Summer 7-21-2014

Numerical Experiments of Dynamical Processes During the 2011-2013 Surge of the Bering-Bagley Glacier System, Using a Full-Stokes Finite Element Model

Thomas Trantow
University of Colorado Boulder, trantow@colorado.edu

University of Colorado

Master's Thesis

Numerical experiments of dynamical processes during the 2011-2013 surge of the Bering-Bagley Glacier System, using a full-Stokes finite element model

Author:
Thomas Trantow

Supervisor:
Professor Dr. Ute C. Herzfeld

A thesis submitted in fulfillment of the requirements
for the degree of Master of Science

in the

Geomathematics Research Group
Department of Applied Mathematics

2014

Signature Page

This thesis entitled:
Numerical experiments of dynamical processes during the 2011-2013 surge of the Bering-Bagley Glacier System, using a full-Stokes finite element model
written by Thomas Trantow
has been approved for the Department of Applied Mathematics

(Professor Dr. Ute Herzfeld, Committee Chair)

(Professor Harvey Segur, Committee Member)

(Professor Juan Restrepo, Committee Member)

Date: _____

The final copy of this thesis has been examined by the signatories, and we find that both the content and the form meet acceptable presentation standards of scholarly work in the above mentioned discipline.

UNIVERSITY OF COLORADO

Abstract

Thesis directed by Ute C. Herzfeld
Department of Applied Mathematics

Master of Science

Numerical experiments of dynamical processes during the 2011-2013 surge of the Bering-Bagley Glacier System, using a full-Stokes finite element model

by Thomas Trantow

The Bering-Bagley Glacial System (BBGS) is the largest glacier system outside of the Greenland and Antarctic ice sheets, and is the Earth's largest surge-type glacier. Surging is one of three types of glacial acceleration and the least understood one. Understanding glacial acceleration is paramount when trying to explain ice discharge to the oceans and the glacial contribution to sea-level rise, yet there are currently no numerical glacial models that account for surging.

The recent 2011-2013 surge of the BBGS provides a rare opportunity to study the surge process through observations and the subsequent data analysis and numerical modeling. Using radar, altimeter, and image data collected from airborne and satellite missions, various descriptions of ice geometry are created at different times throughout the surge. Using geostatistical estimation techniques including variography and ordinary kriging, surface and bedrock Digital Elevation Maps (DEMs) are derived. A time series analysis of elevation change during the current surge is then conducted and validated using a complete error analysis along with airborne observations.

The derived DEMs are then used as inputs to a computer simulated model of glacier dynamics in the BBGS. Using the Finite Element software Elmer/Ice, a full-Stokes simulation, with Glen's flow law for temperate ice, is created for numerical experiments. With consideration of free surface evolution, glacial hydrology and surface mass balance, the model is able to predict a variety of field variables including velocity, stress, strain-rate, pressure and surface elevation change at any point forward in time. These outputs are compared and validated using observational data such as CryoSat-2 altimetry, airborne field data, imagery and previous detailed analysis of the BBGS.

Preliminary results reveal that certain surge phenomena such as surface elevation changes, surge progression and locations at which the surge starts, can be recreated using the current model. Documentation of the effects that altering glaciological parameters and boundary conditions have on ice rheology in a large complex glacial system comes as secondary result. Simulations have yet to reveal any quasi-cyclic behavior or natural surge initiation.

Dedicated to the summer 2012 Bering Glacier expedition team, who endured a cramped 12 day, 5600 mile drive, sleeping wherever there was flat ground, all for a little science and adventure.

Acknowledgements

First and foremost I would like to thank Dr. Ute Herzfeld for giving a young undergraduate who knew nothing about glaciers the opportunity to go on a once in a lifetime adventure up to wild Alaska to observe these magnificent rivers of ice. The knowledge and appreciation I gained on that trip serves as the main inspiration behind this thesis and memories of that experience will be with me for a lifetime. I would also like to thank each of my fellow student co-workers in the Geomathematics group, especially Brian McDonald and Griffin Hale, who have not only helped mightily in coming up with results, but served as willing walls to bounce ideas off of. Thanks goes to Professors Harvey Segur and Juan Restrepo for serving as thesis committee members and to Professor Anne Dougherty for being an extremely supportive and helpful advisor throughout the years. Lastly, I want to thank my friends and family for their continued patience and encouragement over the past six years as I pursued my interests, whatever they happened to be.

Contents

List of Tables

List of Figures

Abbreviations

BBGS	**B**ering-**B**agley **G**lacial **S**ystem
BBJ	**B**ering-**B**agley **J**unction
BDF	**B**ackward **D**ifference **F**ormula
DBL	**D**ynamic **B**alance **L**ine
DEM	**D**igital **E**levation **M**odel/**M**ap
ELA	**E**quilibrium-**L**ine **A**ltitude
EDS	**E**fficient **D**rainage **S**ystem
FEA	**F**inite **E**lement **A**nalysis
FEM	**F**inite **E**lement **M**ethod
IDS	**I**nefficient **D**rainage **S**ystem
IPCC	**I**ntergovernmental **P**annel on **C**limate **C**hange
JPL	**J**et **P**ropulsion **L**aboratory
SIF	**S**olver **I**nput **F**ile
SAR	**S**ynthetic **A**perature **R**adar
SMB	**S**urface **M**ass **B**alance
USGS	**U**nited **S**tates **G**eological **S**urvey
WISE	**W**ide-field **I**nfrared **S**urvey **E**xplorer

Physical Constants

Earth's standard acceleration due to gravity	g	=	9.80665 $\mathrm{m{\cdot}s^{-2}}$
Density of water	ρ_w	=	1000 kg/m^3
Density of ice at $0°C$	ρ_i	=	916.2 kg/m^3
Gas constant	R	=	8.3144621 $\mathrm{J{\cdot}mol^{-1}{\cdot}K^{-1}}$

Symbols

Symbol	Variable Name	Unit
a	variogram range	m
a_s	accumulation/ablation	m
c_0	nugget effect	m^2
$\boldsymbol{g}$	gravity vector	$m \cdot s^{-2}$
h	lag	m
n	glen or creep parameter	
nug	nugget	m^2
s	estimation standard deviation	m
s_0	error estimate of z	m
p	isotropic pressure	Pascals (Pa) ($\mathrm{N} \cdot \mathrm{m}^{-2}$)
$\boldsymbol{u}$	velocity	$\mathrm{m} \cdot \mathrm{s}^{-1}$
u_b	mean sliding velocity	$\mathrm{m} \cdot \mathrm{s}^{-1}$ ($\mathrm{m} \cdot \mathrm{a}^{-1}$)
z	realization (measurement) of a spatial random variable	
z_b	elevation at the base of a glacier	m
z_s	elevation at the surface of a glacier	m
A	flow parameter	$\mathrm{Pa}^{-3} \cdot \mathrm{s}^{-1}$
D	glacier (domain) region	
N	effective pressure	Pa
Q	activation energy	$\mathrm{kJ} \cdot \mathrm{mol}^{-1}$
T	temperature	Kelvin (K)

Y	Young's modulus	
Z	spatial random function	
α_i	kriging weights	
γ	experimental variogram	
γ_{gau}	Gaussian variogram	
$\dot{\boldsymbol{\epsilon}}$	strain rate tensor	s^{-1}
η	effective viscosity	$\mathrm{Pa} \cdot \mathrm{s}$
κ	Poisson ratio	
λ	Lagrange parameter	
ρ	density	$\mathrm{kg} \cdot \mathrm{m}^{-3}$
$\boldsymbol{\sigma}$	Cauchy stress tensor	Pa
σ_{ii}	normal stress	Pa
σ_0	noise levels	m
$\boldsymbol{\tau}$	deviatoric stress tensor	Pa
τ_{ij}	shear stress	Pa
Φ	hydropotential	$kg \cdot m^{-1} \cdot s^{-2}$
Ψ	a scalar quantity	

"Like all good fruit the balance of life is in the ripe and ruin."

– Δ

Chapter 1

Introduction

1.1 Purpose of study

With the accelerated warming of our environment comes a rapid increase in the melting and overall behavior of the glaciers and ice sheets around the world, and its potentially disastrous effect on human society is unavoidable. It is sometimes difficult to prove that some catastrophic environmental event was caused by our changing climate due to the inherent complexity of the chaotic system we call Earth. Yet there is one undeniable measurement that we can directly attribute to our warming planet: sea level rise. The increase in our ocean's water level is caused in part by the melting of ice sheets and glaciers in the polar and mountain regions around the world. In the most recent Intergovernmental Panel on Climate Change (IPCC) Assessment Report (AR5) in 2013, it was shown with high confidence that sea level rise has increased from an average of 1.7 mm/yr at the beginning of the 20th century to 3.2 mm/yr in the past couple of decades with a projected continued increase in the range of 8 to 16 mm/yr by the end of the 21st century (Church et al., 2013). This number has increased from the last IPCC report (AR4) in 2007 due to improved modeling methods of land-ice systems (Church et al., 2013). With most of the world's population living in coastal regions, a change in water level of this magnitude would displace millions of people globally leaving parts of many cities underwater.

If we are to predict the amount of mass that is discharged by ice sheets and glaciers, it is fundamental to understand the dynamics of ice, that is, how it flows and reacts to its environment.

A first way to grasp how ice evolves is to observe its movements by taking measurements of its position, velocity and surface elevation at various times. By making these observations over the past century, scientists have discovered that most of the mass transfer from the ice sheets to the oceans is done through the fast-moving outlet glaciers, which tend to react most rapidly to warming (Krabill et al., 2004; Mayer and Herzfeld, 2008; Pelto et al., 1990). These regions of accelerated ice, or *ice streams*, tend to switch between slow and fast modes of flow and the mechanisms that trigger this switch are largely unknown (Clarke, 1987). This brings about a particular interest in certain glaciers that demonstrate unstable flow patterns called *surge glaciers*. Different from normal valley glaciers that display an overall constant and normal flow, a surging glacier will quasi-periodically experience extreme flow pulsations. There are not many glaciers that exhibit surge behaviors but their very existence suggest that there are internal processes that control fast and slow flow (Clarke, 1987). Therefore the study of surge-type glaciers is of high importance when trying to understand flow instability (Clarke, 1987).

The largest of these surge type glaciers is Bering Glacier, located in the Chugach - St. Elias Mountains in southeast Alaska, whose ice system is of similar size to the ice streams in Greenland and Antarctica. Therefore the study of the surge processes in the Bering-Bagley Glacial System (BBGS) should provide valuable insight into flow instability in a large and complex system. A surge of Bering Glacier can cause a major change in the costal environment, including disruption of shipping lanes, further motivating the need for understanding its flow. Its current surge, initiating in 2011, gives us a rare opportunity to observe and measure the surge phenomenon. This thesis seeks to further our current knowledge of surge-type glaciers and the mechanisms controlling periodic flow, thus contributing to the understanding of ice loss to our rapidly thinning ice sheets.

1.2 Scope of study

The ultimate goal of this study is to create a numerical model of the Bering-Bagley Glacial System that sheds light on the surge mechanisms and behavior. This is done by using a variety of observations to generate a realistic glacier structure on which experiments can be done. Observations are also used to validate any resulting behaviors predicted by the model. Mathematical consideration of the physical processes such as glacier flow, free surface evolution and

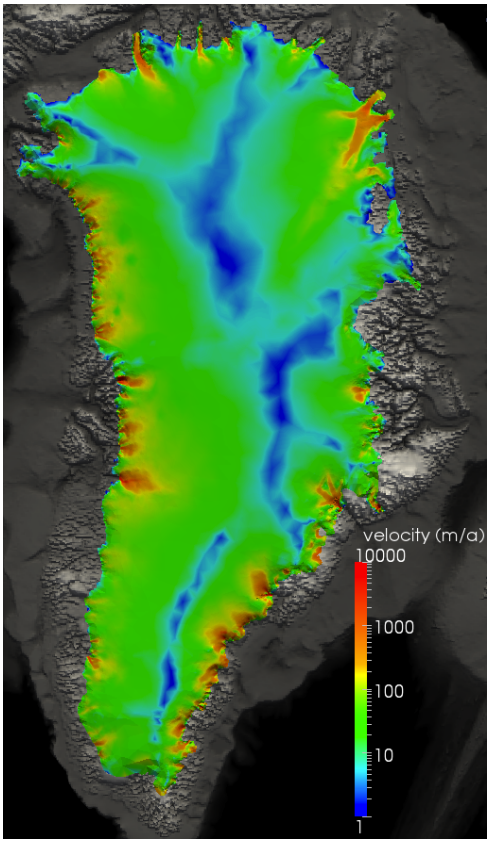

FIGURE 1.1: **Ice velocity on the Greenland Ice Sheet.** Mass transfer from the ice sheet to the ocean is largely through the outlet glaciers of high velocity. This velocity map created using the FEM software Elmer/Ice by Seddik et al. (2012).

glacier hydrology are taken into account, along with some of the ideas and numerics of the Finite Element Method (FEM).

Only the Bering-Bagley Glacial System is considered and some analysis will restrict our view further to only Bering Glacier itself due to data availability at the time of investigation. Other surge glaciers that have received an immense amount of study, especially those in Southeast Alaska such as Variegated Glacier, were considered in depth when reviewing what is known about the surge mechanisms (see Cuffey and Paterson (2010), Jay-Allemand et al. (2011), Kamb et al. (1985), Eisen et al. (2001), Eisen et al. (2005) and Harrison et al. (2008)).

A glacier is a very complex system, especially one as large as the BBGS, and therefore multiple physical processes should be considered to get the most accurate representation possible. Yet, because this is the first implementation of such a model, we must start simple with a few assumptions, and add complexity as we move forward. For example, the scope of this study

does not account for temperature interactions between the surrounding environment and the ice, an important factor when considering meltwater and its effect on basal slipping. Most experiments consider only the process of ice evolution, which is driven by gravity and restricted by the surrounding geology. The effects that hydrology and the atmosphere have on glacier evolution are artificially simulated but not modeled in their own right as separate processes. At the very end of experimentation, a first attempt at simulating the basal hydrologic system, and its coupling to the glacier dynamics, is shown.

This thesis begins with a complete background of the relevant studies in the field of glaciology as well as an overview of the physical and mathematical concepts that are required when studying glaciers and ice sheets. A detailed description of the steps to create the necessary input for a glacier model are then given along with information on the software used for simulation and its methods of calculation. Results and analysis begin with a time series study of the derived Digital Elevation Models (DEMs) along with a complete error analysis, which provides insight into the current surge of Bering Glacier and is used as validation for the model. The results of the nearly 100 experiments are then given in chronological order with comments on any insight that was gained. Although the order in which experiments were done may seem sporadic at times, it follows the natural logical progression of experimentation. Finally, a short conclusion of the results and their implications is given along with future directions this study could take. Appendices containing code samples and tangent projects are found following the concluding remarks.

1.2.1 Data sets and limitations

In order to create a realistic model of the Bering-Bagley Glacial Glacier, observational data are needed to define the surface and bedrock topography of the glacier. Surface elevation of the BBGS is measured using airborne altimetry (Herzfeld et al., 2013a; Muskett et al., 2009) or satellite altimetry such as CryoSat-2 (ESA, 2007). The two main criteria used in deciding which data set(s) to use are (1) the data coverage throughout the glacial system and (2) the frequency of measurements. Based on these two characteristics, surface topography was derived using CryoSat-2 data (see section 3.3.1.1). CryoSat-2 data over the Bering Glacier became

available in 2009 and not until 2011 was the data frequent enough to get sufficient coverage over a six-month period, thus restricting data analysis to 2011 at the earliest.

Bed topography is inherently harder to attain due to the difficulty of ice penetration measurements. Several attempts at ice thickness measurements, from which bed topography can be easily derived, were done by Conway et al. (2009) and Rignot et al. (2013) using low-frequency ice-penetrating radar systems. The thickness data collected by Rignot et al. took time to process and was not made available to our group here in Colorado until later in experimentation. Before acquisition of this data, only Bering Glacier, and not the entire BBGS, could be modeled.

The other surface and bed elevation data that were available were used as validation sets for model results. Other data sets involving surface velocity and mass balance were not available to us, but their published results are still used as validation (see Burgess et al. (2012), Tangborn (2013) and Turrin et al. (2013)). A more in-depth look at the data sets is given in Chapter 3.

Chapter 2

Background

2.1 The Bering-Bagley Glacial System and the surge phenomenon

2.1.1 The Bering-Bagley Glacial System

The Bering-Bagley Glacial System (BBGS), which mainly consists of Bering Glacier and the Bagley Ice Valley, is the largest and longest glacial system in North America and is characterized by its tendency to surge. Located on the southeastern coast of Alaska, the BBGS stretches over 200 km long and has an ice surface area of around 5200 km^2. The BBGS is a *temperate glacier* meaning that its ice, from surface to base, is at or near the melting point throughout the year (Cuffey and Paterson, 2010). Bering Glacier is a prototype of a large surge-type glacier, and is comparable in size to the large fast-moving outlet glaciers of Greenland and Antarctica[1]. The BBGS is the largest glacial system outside of the Greenland and Antarctic ice sheets and therefore provides a rare opportunity for observation and analysis of the surge phenomenon in a large and complex glacier system (Fatland et al., 2003; Herzfeld, 1998; Herzfeld and Mayer, 1997; Molnia and Williams, 2001; Molnia, 2008; Molnia and Post, 2010a,b).

[1]Most of the surge dynamics occur on the Bering Glacier portion of the BBGS, and so often, when referencing surge specific behaviors and characteristics of the BBGS, the name "Bering Glacier" is used when talking about the glacial system.

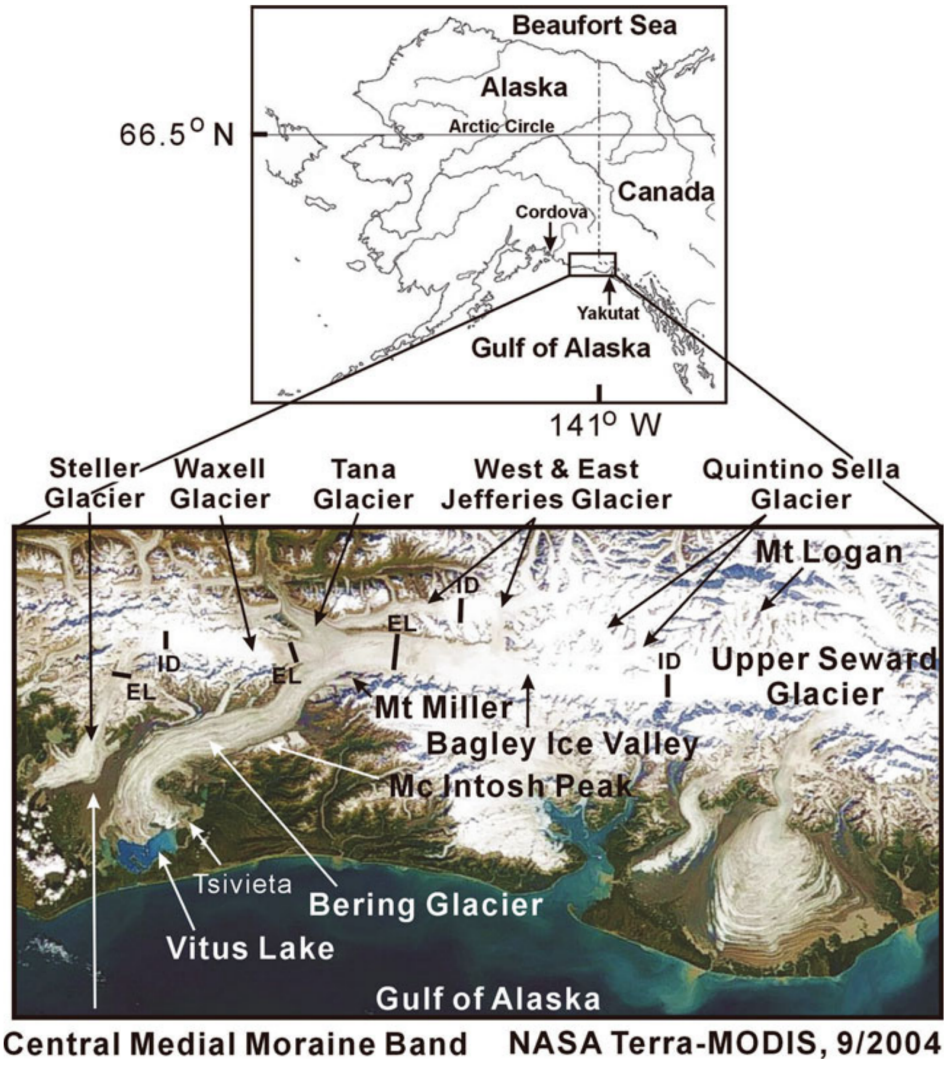

FIGURE 2.1: **The Bering-Baley Glacial System and the surrounding area.** Located in the Chugach and St. Elias Mountains in southeast Alaska, the BBGS is the world's largest glacial system outside of the continental ice sheets. ID corresponds to the dividing lines between features and EL labels historical equilibrium lines dividing accumulation and ablation zones (also known as the ELA). This figure is taken from Muskett et al. (2009).

2.1.2 Description of the surge phenomenon

A surge is a catastrophic dynamic event during which the glacier accelerates 10-100 times its normal velocity and advances rapidly. A surge-type glacier is defined by a quasi-periodic cycle consisting of a long quiescent phase with normal ice flow or slow retreat, and a short surge phase of accelerated flow. During the quiescent phase, overall glacier geometry is steepened due to the changing surface mass balance (SMB) in which the glacier thickens in areas of accumulation

and thins in areas of ablation (Raymond, 1988). The regions of accumulation and ablation are divided by the equilibrium-line altitude (ELA). Some glaciers will have small acceleration events, or "mini-surges", during the quiescent phase that will redistribute the build-up/loss of ice throughout the glacier (Harrison and Post, 2003; Meier and Post, 1969; Raymond, 1987). This leads to the definitions of a *reservoir area*, defined as the area of general thickening during the quiescent phase, and the *receiving area* to which mass is transferred during the surge, located both up-glacier and down-glacier of the reservoir area. In consequence, drastic elevation changes occur during the surge phase, including rapid thinning in the former reservoir area, drawdowns along the margins of the glacier and thickening in the receiving areas (Fowler, 1987, 1989; Harrison and Post, 2003; Meier and Post, 1969; Raymond, 1987). The division between the reservoir and receiving areas is called the dynamic balance line (DBL) and can move over time throughout both phases (Raymond, 1987).

Heavy crevassing indicative of sudden deformation, horizontal and vertical displacement of ice and sudden changes in the glacial hydrologic system are also characteristics of a surge. The state of current knowledge on the surge process has been summarized by Meier and Post (1969), by Raymond (1987) and by Harrison and Post (2003), with the conclusions that the physics of the surge process are still not well understood. In recent studies, the effects of glacier geometry, climate and setting, of basal morphology and composition of the bed, or rather, susceptibility of the bed material to deformation, and of englacial water distribution have been investigated in three regards: as factors that may explain that a given glacier is a surge-type glacier, as causes of glacier surges and as triggers of an actual surge (Björnson et al. (2003); Copland et al. (2003); Fatland et al. (2003); Harrison and Post (2003); Jay-Allemand et al. (2011); Jiskoot et al. (2003); Kamb (1987); Kamb et al. (1985); Lingle and Fatland (2003); Murray et al. (2003); Quincey et al. (2011) and other papers in Annals of Glaciology 36, 2003, see also Bruhn et al. (2010)).

Meier and Post (1969) distinguish 3 types of surging glaciers: (i) large-sized with high surge velocities, large displacement and large lowering of the ice reservoir, (ii) large-sized with low surge velocities, small vertical and horizontal ice displacement, and (iii) steep, small glaciers with small reservoir lowering and ice displacement. Much of the research on the physics of the surge process is based on few case studies of mostly smaller glaciers of type (iii), such as the 1982-1983, but also the 2003 surge of Variegated Glacier, Alaska (see e.g. Eisen et al. (2001, 2005); Harrison et al. (2008); Humphrey et al. (1986); Jay-Allemand et al. (2011); Kamb et al.

(1985); Raymond (1987)) and surges of Trapridge and South glaciers, Yukon (Clarke et al., 1987; Flowers and Clarke, 2000, 2002a,b; Flowers et al., 2011), which are easier to equip with geophysical instrumentation but behave differently than large glaciers. The progression of a surge in a large glacier and the characteristic dynamics of each surge phase has only recently started to be analyzed systematically with the latest surge of Bering Glacier (Burgess et al., 2012; Herzfeld et al., 2013a; Turrin et al., 2013), and this thesis is a contribution to this problem.

The Bering-Bagley Glacial System is a complex glacier system of type (i) that has a surge cycle around 20-25 years and is currently surging (2011, 2012, 2013, ..?). The major surge event started when the reservoir collapsed in spring 2011 and ice was released and transferred into the receiving zones. Elevation loss of 40-70 m in the reservoir area was derived from airborne laser altimeter observations, and mass transfer to a receiving area in lower Tashalich arm resulted in elevation gain of 20-40 m (Herzfeld et al., 2013a). A smaller acceleration event was recorded in 2008 leading some to say that the surge technically started before 2011 (Burgess et al., 2012; Turrin et al., 2013). Because "mini-surges" happen frequently in the BBGS, the definition of when the glacier is in a surge phase can vary, but here we say it started in spring 2011 with this larger mass redistribution event. It is important to note that some of the current studies of the latest BBGS surge only analyze glacier dynamics of the years from 2008 to 2011 (more so in 2008 than 2011) and do not consider glacier movement that occurred in 2012 and 2013 when the BBGS was still displaying signs of surging (see sections 4.1.1 and 4.1.2).

2.1.3 Current knowledge of the surge process

Glaciers evolve by a combination of viscous ice deformation, basal sliding over the bed, and in the case of soft, non-rigid beds, the deformation of the bed itself. Basal activity, especially in temperate glaciers, is the key to understanding how and when glaciers move as it can account for 90% of the total observed surface velocity (Cuffey and Paterson, 2010). Glacier movement due to sliding occurs when the water pressure at the base is sufficiently high to reduce the friction between the glacier and the bed over which the ice flows. The composition of glacier beds is mostly unknown due to the difficulty of observation, but is usually assumed to either be a hard, rigid bed or a soft bed consisting of a sediment layer between the glacier and an eventual solid base. With hard beds, high water pressure will reduce resistance through cavitation at the

ice/bed boundary whereas for soft beds, increasing water pressure will cause dilatation of the sediment layer (Fleurian et al., 2014; Flowers and Clarke, 2002a,b).

During the southeast Alaskan summers, warmer temperatures induce surface melting throughout the glacier. The meltwater is transferred to the base through englacial tunnels, or moulins, thus requiring the formation of drainage system at the ice/bedrock interface to transfer the water downstream. The hydrological system at the base of a glacier is usually classified into two main groups: (i) inefficient drainage systems (IDS), characterized by high water pressure, and a system of linked cavities in the case of hard beds or diffusion in the sediment layer for soft beds (Lliboutry, 1968; Shoemaker, 1986; Weertman, 1972) and (ii) efficient drainage systems (EDS) with low water pressure and channels in the ice and/or bed (Nye, 1970; Rothlisberger, 1972).

In the quiescent phase, the glacier is able to create a tunneled system that efficiently drains the water. An increased supply of water through rain or accelerated melting will increase the water pressure at the base, but these channels can expand to accommodate the increased flux (Rothlisberger, 1972). During a surge, the efficient drainage system is changed into an inefficient one that increases basal water pressure causing increased ice velocities. The change from an EDS to an IDS is thought to occur at the DBL where the up-glacier thickening and the down-glacier thinning steepens the geometry, which in turn increases the local driving stress. This can force the basal water pressure to rise to accommodate an increased flux (Kamb, 1987). With an increased basal water pressure, the shear force of the bedrock on the ice is reduced thus causing the ice to accelerate until it can reach a force equilibrium (Raymond, 1987). This steepening of geometry at the DBL is sometimes called a *surge front*, and resembles a bulge that can propagate both up and down-glacier and is coincident with peak surface velocities. The surge front can increase in height and velocity as it moves down glacier, as seen in the 1982-1983 surge of Variegated Glacier (Kamb et al., 1985). Compressional longitudinal stresses are formed in front of the bulge and extensional stresses behind, which can be identified by looking at fresh crevasse formations (Herzfeld et al., 2013b). The activation mechanism of the surge front is unknown but is said to propagate both down and up-glacier from a nucleation point in the form of a kinematic wave. As this wave passes, it will activate the inefficient drainage system (Fowler, 1987).

It is still unknown exactly how this activation wave and increased driving stress promotes and maintains the shift from an EDS to an IDS or vice versa. One guess is made in the case of soft glacier beds: the sediment layer is thought to deform when the driving stress increases allowing an increased ice velocity without an increase in resistive shear stress, and so the glacier can accelerate until lateral or longitudinal frictions slow it down (Cuffey and Paterson, 2010).

2.1.3.1 Principles of modeling a surge

Ideally, a surge model will produce a glacier with a periodic (or quasi-periodic) oscillating state between a long state of slow flow with gradual build-up, and a short state of accelerated flow and rapid drainage. A surge can be easily produced by lowering basal shear stress for some short amount of time (Campbell and Rasmussen, 1969). Physically this is done by increasing the basal water pressure through the production of meltwater (Lliboutry, 1964). This already requires the coupling of glacier flow dynamics to the hydrological system and the surrounding atmospheric and geothermal environment, each complex systems in their own right.

Budd (1975) lays out a few key principles for a surging glacier model. (1) Using a constant input of bedrock configuration (in the case of a rigid bed), surface mass balance distribution and properties of the ice, a steady state glacier does not result. (2) The same laws and ice properties apply to all temperate glaciers, at least up to the first order. (3) Surging is a large scale phenomenon that can be adequately represented by a numerical model that uses discrete values with spacing comparable to ice thickness. This would imply that small scale bedrock features are not relevant except in their contributions to bulk averages over larger scales. According to Budd, nothing more than this is needed to simulate surging but more recent studies have shown that inclusion of basal hydrology is necessary to recreate a surge (Fowler (1987); Gagliardini et al. (2007); Jay-Allemand et al. (2011); Kamb (1987); Kamb et al. (1985); Raymond (1987) among others).

Several methods have been used to try and simulate the hydrological system at the base of a glacier (Fleurian et al., 2014; Flowers and Clarke, 2000, 2002a,b; Flowers et al., 2011). A recent model given by de Fleurian (Fleurian et al., 2014) uses a double continuum approach that relies on porous layers located at the glacier bed to compute the water heads of the inefficient water systems and an equivalent porous layer (EPL). This implementation eliminates the need to

model the exact tunnel and/or cavity system by using an entire layer at the base that mimics certain properties of the actual system.

The hydrological system is coupled to the flow evolution of the glacier by a friction law at the base of the glacier that relates basal shear stress to ice velocity. Recent studies have been dedicated to finding the best representative friction law, which should consider water (or effective) pressure, bedrock topography and composition, and the existence of subglacial cavities. The latest, and so far most accurate, of these laws is given by Gagliardini et al. (2007), which gives a multivalued relation between shear stress and velocity at the base, thus allowing for the possibility of a periodically surging glacier. An overview of basal friction laws is given in section 2.2.5.2.

2.1.4 Observations of surges in the Bering-Bagley Glacial System

2.1.4.1 Surge history in the BBGS

Before the current surge, six different surge events have been recorded in 1900, 1920, 1938-1940, 1957-1960, 1965-1967 and 1993-1995. Despite these periodic advancements, the BBGS has been slowly retreating at a rate of around 0.04-1.0 km per year (Molnia, 2008; Molnia and Post, 1995). Both of the latest surges in 1965-1967 and 1993-1995 display multiple acceleration events followed by stagnant ice during their respective time ranges (Fatland and Lingle, 2002; Molnia, 2008; Roush et al., 2003).

The best documented case of a BBGS surge was in 1993-1995. It is believed that the onset of the ice acceleration occurred during the winter of 1993 in lower-central Bering above the overflow area, and had a peak velocity between 59 to 100 m/day (21,535 to 36,500 m/a)[2] once it reached the terminus (Fatland and Lingle, 1998; Roush et al., 2003). Surge speeds near the terminus were on average 10-20 m/day (3650-7300 m/a) while speeds up in the Bagley Icefield were around 5 m/day (1825 m/a) (Fatland and Lingle, 2002). As a reference, speeds in the quiescent phase were less than 1 m/day (365 m/year) in both of these regions (Post, 1972). A surge front documented as a leading surface undulation was observed traveling around 100 m/day (36,500 m/a) from the location of surge onset to the terminus. Fluctuating acceleration rates, increased velocities and surface elevation changes were observed downstream of the Jefferies

[2]Conversions to meters per year are shown because results from the model are given in units of MPa-m-a.

confluence to the Bagley Icefield where uniform flow velocities were observed in quiescence (Fatland and Lingle, 2002). The surge was associated with high englacial water pressures due to the observations of clear blue water in crevasses and lakes on the surface (Lingle et al., 1993).

2.1.4.2 Observations of the current BBGS surge

The observations of the current surge are based on laser altimeter data from Herzfeld et al. (2013a), synthetic aperture radar (SAR) offset tracking and LiDAR altimetry analysis by Burgess et al. (2012), and optical feature-tracking methods from Landsat-7 imagery by Turrin et al. (2013).

According to Burgess et al. (2012), during the quiescent phase two small acceleration events occurred, the first sometime between 1995 and 2000 and the second between 2003 and 2007. The first resulted in a small surface lowering of about 10 meters just above the Bering-Bagley junction (BBJ) and about 5 meters of thickening below the junction. The second event resulted in a surface lowering of around 20 meters in the reservoir area in the lower Bagley Icefield that translated into surface elevation gain of about 35 meters near the bend in the upper-central Bering. The DBL was estimated to be at mid-glacier just below the the northern inflowing glacier with a reservoir area extending up to the BBJ. The area between the DBL and 10 km down-glacier is thought to be the trigger area of the surge, due to a $\sim 70\%$ increase in driving stress.

The onset of the major surge event occurred in spring 2011 with a smaller acceleration event in 2008 (Burgess et al., 2012; Herzfeld et al., 2013a). Surface speeds in late 2007 and early 2008 were around 1 m/day (365 m/a) in the Bagley Icefield and upper Bering Glacier (LeBlanc, 2009). Between September 2008 and February 2009 the BBGS accelerated progressively from the BBJ to the lower-mid glacier right above the overflow area (Burgess et al., 2012). The maximum recorded velocity was 7 m/day (2555 m/a) near mid-glacier but peak speeds might have been even higher (Burgess et al., 2012). In early 2010, surface speeds in the lower and central Bering glacier returned to normal quiescent speeds and velocity in the lower Bagley and upper Bering were measured at around 2 m/d (720 m/a). During this event, it is thought that accelerations in the Bagley Icefield happened around the same time if not before accelerations

in the Bering portion of the BBGS (Burgess et al., 2012). A peak thickening of $\sim$ 90 meters occurred above the overflow area.

The prominent part of current surge is believed to have started in late winter/ early spring in 2011. The recently heightened reservoir area in the lower-central Bering, observed by Herzfeld et al. (2013a) and Burgess et al. (2012), transferred its mass down-glacier along the northern branch of the flow regime to the lower Tashalich arm area. The former reservoir area experienced surface lowering of 40-70 meters while the receiving area gained 20-30 meters of surface elevation (Herzfeld et al., 2013a). The DBL of the surge is thought to be just below the bend at the Grindle Hills. There was very few measurements of velocity during 2011, but one 11 day interval in the beginning of July showed a peak velocity of 9 m/day (3285 m/a) in the central and upper-central part of Bering Glacier (Burgess et al., 2012). No velocity measurements were made in the lower part of Bering. The thickening continued to move downstream until it reached the terminus, where it extended 2-4 km (Turrin et al., 2013).

Additional analysis of the 2011 part of the surge, as well as extended consideration to surge dynamics in 2012 and 2013, will be presented in section 4.1.2 using derived difference DEMs using CryoSat-2 altimeter data.

2.2 The physics of glaciers

This overview of stress and strain and of the equations governing ice rheology follows that given in Cuffey and Paterson (2010).

2.2.1 Stress and strain

Stress is defined as force per unit area. It has the same units as pressure, however, stress is a much more complex quantity because it varies both with direction and with the surface it acts on. When we study stress we look at the balance of forces between two parts of a body. In continuum mechanics, we usually define stress as a second-order tensor called the *stress tensor*, or *Cauchy stress tensor*, whose components are given by,

$$\boldsymbol{\sigma} = \begin{pmatrix} \sigma_{xx} & \tau_{xy} & \tau_{xz} \\ \tau_{yx} & \sigma_{yy} & \tau_{yz} \\ \tau_{zx} & \tau_{zy} & \sigma_{zz} \end{pmatrix}. \tag{2.1}$$

If we were to define our rectangular coordinates so that x is the direction normal to the surface element, σ_{xx} would be the *normal stress* component whereas σ_{yy} and σ_{zz} would be the *tangential stresses*. *Tensile* or extensional stress is defined to be positive whereas *compressional* stress is negative. Components $\tau_{ij} = \sigma_{ij}, i \neq j$, are called *shear* stresses, which can be thought of as stresses that change angles in an object. In other words, shear stress would change originally rectangular objects into parallelograms. Shear stress acts parallel to a surface and becomes a key factor, for example, when determining the basal sliding component of glacier movement. In three dimensions, only six components of the stress tensor are independent. In order to avoid any rotational acceleration of an element, shear stresses τ_{ij} and τ_{ji} are equal, resulting in a symmetric tensor. Knowing these six values is sufficient when specifying the state of stress in a body.

Alternatively, we can specify stress by knowing the *principle stresses* and their directions (*principle axes*), defined as the values and directions that maximize normal stress. Along these principle axes, which are mutually orthogonal, shear stress is nonexistent. The principle stresses are in fact the eigenvalues of the stress tensor and their corresponding eigenvectors represent the principle axes. There is a common decomposition of the stress tensor into its isotropic and deviator parts, which is gone over in more detail in section 2.2.2.

Strain is a dimensionless measure defined as the amount of deformation an object experiences compared to its original size and shape. For example, if a block 10 cm on a side is deformed so that it becomes 9 cm long, the strain is (10-9)/10 or 0.1 (sometimes expressed in percent, in this case 10 percent). In glaciological studies we are more interested in strain *rates*, particularly the strain-rate tensor labeled by $\dot{\boldsymbol{\epsilon}}$, as the relation between stress and strain-rate defines our flow law (see section 2.2.3).

2.2.2 Stokes equations

Ice is a highly viscous material that moves very slowly and its flow can be described by the Stokes equations, which is simply a linearization of the Navier-Stokes equations neglecting the inertial and acceleration terms. If we assume a single driving force due to gravity in the z-direction, conservation of linear momentum in three directions gives us,

$$\nabla \cdot \boldsymbol{\sigma} + \rho \boldsymbol{g} = 0, \tag{2.2}$$

and from conservation of mass we get,

$$\nabla \cdot \boldsymbol{u} = 0, \tag{2.3}$$

where $\boldsymbol{\sigma}$ is the Cauchy stress tensor, ρ is the ice density, $\boldsymbol{g} = (0, 0, -9.81)\ m/s^2$ is the gravity vector, and $\boldsymbol{u}$ is the velocity vector (for a comprehensive list of all the variables and their units that are used in this thesis, see the *Symbols* table on pages xvix-xx).

The Cauchy stress tensor can be decomposed into the difference of the *deviatoric stress tensor*, which tends to distort the body, and the *isotropic pressure*, which tends to change the volume. The (negative of) isotropic pressure is calculated by taking the average of the normal stresses, i.e. the diagonal elements of the stress tensor,

$$p = -(\sigma_{11} + \sigma_{22} + \sigma_{33})/3 = -tr(\boldsymbol{\sigma})/3. \tag{2.4}$$

Decomposing the the stress tensor into its isotropic and deviator parts, $\boldsymbol{\sigma} = \boldsymbol{\tau} - p\boldsymbol{I}$, where $\boldsymbol{I}$ the 3×3 identity matrix and $\boldsymbol{\tau}$ is the deviatoric stress tensor, we can write equation 2.2 as,

$$\nabla \cdot (\boldsymbol{\tau} - p\boldsymbol{I}) + \rho \boldsymbol{g} = 0. \tag{2.5}$$

As a consequence of defining the isotropic pressure as the average normal stress, the deviatoric stress tensor describes pure shear whose trace is equal to zero. The *strain rate tensor*, defined

as the rate of change of the deformation of a material and denoted by $\dot{\boldsymbol{\epsilon}}$, is the symmetric component of the gradient of flow velocity. That is,

$$\dot{\boldsymbol{\epsilon}} = \frac{1}{2}(\nabla \boldsymbol{u} + \nabla \boldsymbol{u}^T). \tag{2.6}$$

It follows that the divergence of the velocity is equivalent to the trace of the strain rate tensor. Thus equation 2.3 can be written as,

$$tr(\dot{\boldsymbol{\epsilon}}) = 0. \tag{2.7}$$

2.2.3 Glen's flow law

The relationship between stress and strain of ice that is commonly used in glaciology is *Glen's flow law*, which assumes that ice is an isotropic material, i.e. the effective viscosity does not depend on the direction of deformation, and is given as,

$$\boldsymbol{\tau} = 2\eta\dot{\boldsymbol{\epsilon}}, \tag{2.8}$$

where η is the effective viscosity defined as,

$$\eta = \frac{1}{2}(EA)^{-1/n}\dot{\epsilon}_e^{(1-n)/n}. \tag{2.9}$$

$A = A(T')$ is a rheological parameter that depends on the ice temperature via an Arrhenius law. That is,

$$A(T') = A_0 exp(\frac{-Q}{RT}), \tag{2.10}$$

where Q is the activation energy, R is the universal gas constant, A_0 is a pre-exponential constant, and T' is the temperature relative to the pressure melting point. The enhancement factor, $E > 1$, in equation 2.9 is a parameter that is suppose to correct for anisotropic effects

based on the type of glacial flow, the age of the ice, etc (Cuffey and Paterson, 2010). The last parameter in equation 2.9 is the exponent n, referred to as the *Glen exponent*. Usually ranging in between 1.5 and 3, the Glen exponent is a heuristic value used to account for the nonlinear relationship between the stress and strain rate of ice (Greve and Blatter, 2009). Note that anisotropic flow laws exist for applications that involve polar ice, where ice is usually more anisotropic, but since Bering Glacier consists of temperate ice, Glen's flow law and its relative simplicity is a fairly accurate approximation of the ice flow (Cuffey and Paterson, 2010).

Under the isotropic assumption, the effective viscosity is independent of the coordinate choice and thus must depend on invariants of the tensor quantities. Second rank tensors like $\boldsymbol{\tau}$ and $\dot{\boldsymbol{\epsilon}}$ have three invariants, i.e. scalar quantities that do not vary under any rotations of coordinate axes (Cuffey and Paterson, 2010). The first invariant for the strain rate tensor (as well as the deviatoric stress tensor) is the trace and the second, termed the *effective strain rate*, is denoted as $\dot{\epsilon}_e$, and its square is defined as,

$$\dot{\epsilon}_e^2 = \frac{1}{2}(\dot{\epsilon}_{11}^2 + \dot{\epsilon}_{22}^2 + \dot{\epsilon}_{33}^2) + \dot{\epsilon}_{13}^2 + \dot{\epsilon}_{12}^2 + \dot{\epsilon}_{23}^2 = tr(\dot{\boldsymbol{\epsilon}}^2)/2. \tag{2.11}$$

2.2.4 Free surface evolution

In glaciological studies, it is common to let the upper surface of the glacier evolve in time due to surface mass balance considerations as well as flow dynamics. Some studies also let the bottom surface of the glacier evolve due to the creation of cavities or tunnel systems at the glacier bed (see Gagliardini et al. (2011)). Surface evolution is described by an advection equation, where the upper surface z_s evolution is given by,

$$\frac{\partial z_s}{\partial t} + u_s\frac{\partial z_s}{\partial x} + v_s\frac{\partial z_s}{\partial y} - w_s = a_s, \tag{2.12}$$

where $\boldsymbol{u_s} = (u_s, v_s, w_s)$ is the surface velocity vector found from the Stokes equation and a_s is the accumulation and/or ablation component that is only prescribed in the normal direction (Gagliardini et al., 2013). There should also be a condition that forces the upper surface to be above the bottom surface or bedrock. If the bottom surface is also evolving, it too should be restricted to be between the upper surface and the bedrock, that is

$$z_s(x, y, t) \geq z_b(x, y, t) \geq b(x, y, t) \ \ \forall t \tag{2.13}$$

where $b(x, y, t)$ represents the fixed bedrock (Gagliardini et al., 2013). The weak form of equation 2.12 together with the restriction given above, form a variational inequality.

2.2.5 Boundary conditions

A variety of different boundary conditions can be applied to each of the glacial boundaries. A *Dirichlet* boundary condition specifies the value that the solution needs to have, while a *Neumann* boundary condition specifies the value that the derivative of the solution must take. A *Robin* type boundary condition specifies some linear combination that the solution and its derivative must take at the boundary. In the case of a symmetric body in which the same physical process occurs on two opposite sides, a *symmetric* boundary condition could be applied. Lastly, *periodic* boundary conditions could also be used if we wish to model only a chunk of a glacier or ice sheet away from the actual physical boundary of the ice body.

2.2.5.1 Ice/atmosphere boundary

The upper surface of the glacier can be treated as a stress-free surface since the atmospheric pressure is considered negligible. Atmospheric pressure is about 101.3 kPa yet the required pressure to deform ice must be on the order of Mega-Pascals (Cuffey and Paterson, 2010). This is given mathematically by,

$$\boldsymbol{\sigma} \boldsymbol{n_s} = -p_{atm} \boldsymbol{\sigma} \approx 0 \tag{2.14}$$

where $\boldsymbol{n_s}$ is the outward pointing normal vector to the surface (Gagliardini et al., 2013).

2.2.5.2 Ice/bedrock boundary

Treatment of the basal boundary condition is one of the most important parts in defining glacier movement since basal slip, due in part to the friction between the bed and the ice, can account

for most of the glacier movement, especially in a surge (Cuffey and Paterson, 2010; Greve and Blatter, 2009; Van der Veen, 2013). Note that basal hydrology also plays a large role in basal slip and is presented in the following section. Without a freely evolving bottom surface, conditions for the ice/bedrock boundary are given by,

$$\boldsymbol{u} \cdot \boldsymbol{n_b} = 0 \tag{2.15}$$

and

$$\sigma_{nt_i} = f_f(\boldsymbol{u}, N) u_{t_i}, \quad i = 1, 2 \tag{2.16}$$

where $\sigma_{nt_i} = \boldsymbol{t_i} \cdot \boldsymbol{\sigma t_i}$ are the basal shear stresses and $u_{t_i} = \boldsymbol{u} \cdot \boldsymbol{t_i}$ are the basal velocities, which are given in terms of the unit tangent vectors $\boldsymbol{t_i}$ $(i = 1, 2)$ and the unit surface normal vector $\boldsymbol{n_b}$ pointing outward to the bedrock surface (Gagliardini et al., 2013). The *effective pressure* is simply the ice normal stress minus the water pressure, that is, $N = -\sigma_{nn} - p_w$. The parameter f_f is known as the *friction parameter* and variations of its calculation define the different friction laws. If $f_f = 0$, equation 2.16 says that no matter the basal velocity, there is no induced shear stress at the base. Physically this represents the ice sliding perfectly over the bedrock. The larger f_f is, the more the bedrock resists ice movement at the base.

Three different friction laws are considered, the first of which is a simple linear relation between the basal shear stress and the basal velocity given by,

$$\sigma_{nt_i} = \beta u_{t_i}, \quad for\ i = 1, 2, \tag{2.17}$$

where $\beta \geq 0$ is the linear friction coefficient.

The second friction law, called the Weertman sliding law, gives a non-linear relation between basal shear and basal velocity:

$$\sigma_{nt_i} = \beta u_b^{(1/n)-1} u_{t_i}, \quad for\ i = 1, 2, \tag{2.18}$$

where u_b is the norm of the basal sliding velocity and n is the exponent from Glen's flow law (Lliboutry, 1968; Weertman, 1972). Notice that if $n = 1$ we arrive at our linear friction law (equation 2.17).

A third friction law was given theoretically by Schoof (2005) and extended by Gagliardini et al. (2007), which describes basal sliding when cavitation is likely to occur,

$$\frac{\sigma_{nt_i}}{CN} + \left(\frac{\chi u_b^{1-n}}{(1 + \alpha_q (\chi u_b)^q)} \right)^{(1/n)} u_{t_i} = 0, \quad for\ i = 1, 2, \tag{2.19}$$

where $\chi = 1/(C^n N^n A_s)$, $\alpha_q = (q-1)^{q-1}/q^q$, A_s is a sliding parameter, and n is the Glen exponent. C is the maximum value of σ_{nt_i} and the exponent $q \geq 1$ controls the post peak decrease (Gagliardini et al., 2013). C should be chosen to be smaller than the maximum local positive slope of the bedrock so that $\sigma_{nt_i}/N \leq C$. This friction law allows us to couple the basal hydrology with ice dynamics, but requires a detailed description of the bedrock topography. Another benefit of this representation is the multivaluedness the law can have for the same velocity. This allows for the possibility of periodic behavior of fast and slow glacial flow. A model successfully implementing this law is presented by Fleurian et al. (2014).

2.2.6 Hydropotential

An interesting quantity pertaining to glacial hydrology is the hydraulic potential or, *hydropotential*. Water will flow from areas of high to low hydropotential and so one can infer the path water might take at the base by looking at a hydropotential map at the ice/bedrock interface. Given a certain glacier geometry, a simplified hydropotential calculation is done just by knowing the ice thickness and pressure at some point.

The expression for hydropotential Φ at the bed is given by,

$$\Phi = \rho_w g z_b + p_w \tag{2.20}$$

where ρ_w is the density of water, z_b is the elevation of the bedrock and $p_w = \rho_i g h - N$ is the water pressure with ρ_i being ice density and N the effective pressure. If there is water at

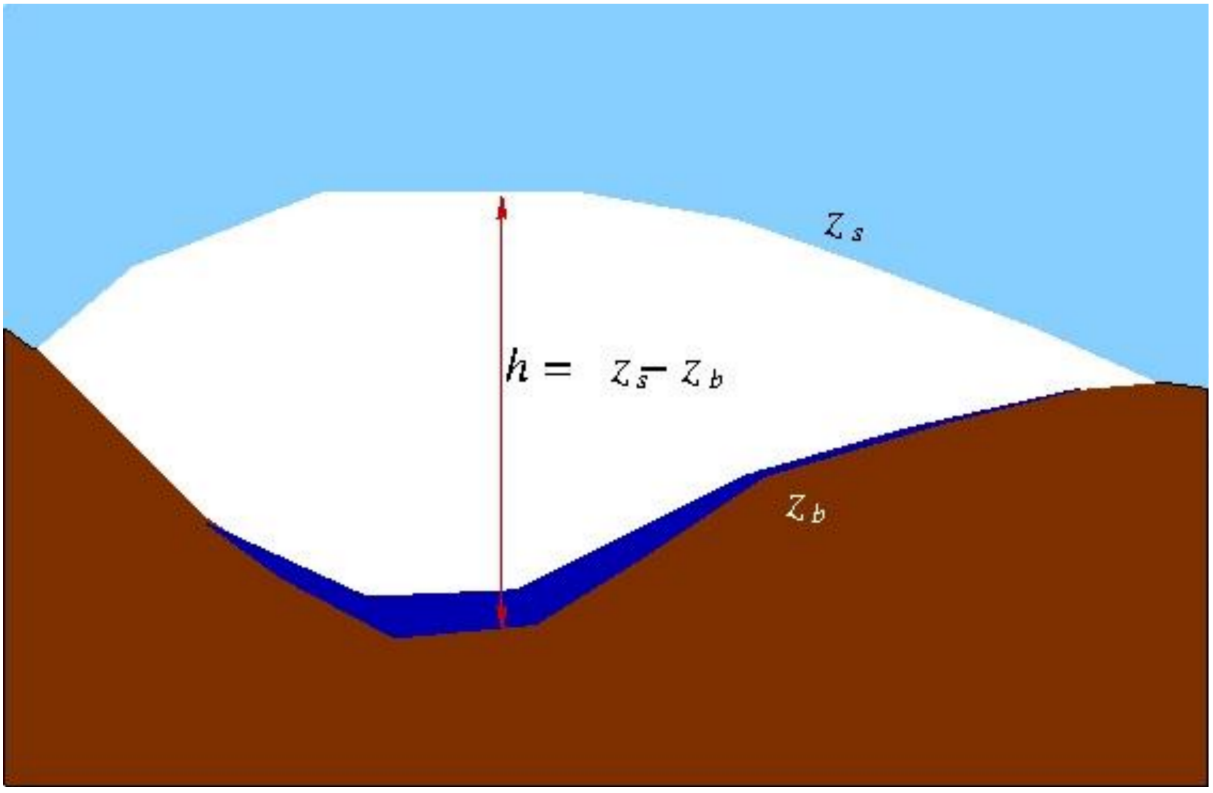

FIGURE 2.2: **Illustration of surface (z_s) and bed (z_b) elevation, important variables in calculation of hydropotential.** Figure courtesy of CSC - IT Center for Science in Finland through the Elmer/Ice website (Zwinger, 2011).

the base of the glacier then the effective pressure is approximately zero and thus $p_w \approx \rho_i g h$. Therefore we can calculate hydropotential by,

$$\Phi = [\rho_i z_s + (\rho_w - \rho_i) z_b] g = [\rho_i h + \rho_w z_b] g, \tag{2.21}$$

where $h = z_s - z_b$ is the height of the glacier.

2.3 Finite Element Method formulation

2.3.1 Mesh generation and deformation

Since most glaciers and ice sheets have lengths and widths much larger than their depths, special treatment is needed when generating a finite element mesh of the glacial body (Gagliardini et al.,

2013). This is especially true for the BBGS where the ratio of centerline depth to glacier width is 1/7 at its largest (see Appendix C). The strategy for creating a glacier mesh for Finite Element Analysis (FEA) requires meshing a 2-D footprint of the glacier and then extruding it up and down in vertical layers. The mesh is structured so that there is the same amount of vertical layers over the entire domain, and the horizontal dimensions are partitioned using an unstructured mesh (Gagliardini et al., 2013). The footprint is created using a contour outline of the ice body, and the top and bottom layers are made to match surface and bedrock topography respectively if desired. The Finite Element Method (FEM) has its advantage here over finite difference and finite volume methods that require a constant grid size over the entire domain.

Transient simulations will require the mesh to deform and update after every time step. With an unstructured mesh, the common approach to rearrange nodes is to solve a pseudo-linear elasticity problem:

$$-\nabla\cdot\left(\frac{2Y\kappa}{(1-\kappa)(1-2\kappa)}\epsilon+\lambda\frac{Y}{2(1+\kappa)}\nabla\cdot\Delta\boldsymbol{x}\boldsymbol{I}\right)=0 \tag{2.22}$$

where Y and κ are Young's modulus and the Poisson ratio respectively, which describe resistance against deformation, and ϵ is the symmetric part of the strain tensor (Gagliardini et al., 2013). Solving for $\Delta\boldsymbol{x}$ we can calculate the location of our updated node based on its initial location $\boldsymbol{x}_0$ via,

$$\boldsymbol{x}(t)=\boldsymbol{x}_0+\Delta\boldsymbol{x}. \tag{2.23}$$

Mesh velocity over one discrete time step can then be calculated by,

$$\boldsymbol{u}_m=\frac{\Delta\boldsymbol{x}(t+\Delta t)-\Delta\boldsymbol{x}(t)}{\Delta t}. \tag{2.24}$$

For a fixed reference frame, the change of a scalar property Ψ is given by,

$$\frac{d\Psi}{dt}=\frac{\partial\Psi}{\partial t}+\boldsymbol{u}\cdot grad(\Psi) \tag{2.25}$$

where $\boldsymbol{u}$ is the fluid velocity. Equation 2.25 consists of local change and a convective part. When considering glaciers and ice sheets, because geometry is not fixed, we usually deal with moving reference frames as opposed to fixed ones (Greve and Blatter, 2009).

In a general reference frame with a moving mesh, conservation dictates that equation 2.25 to turn into,

$$\frac{d\Psi}{dt} = \frac{\partial \Psi}{\partial t} + (\boldsymbol{u} - \boldsymbol{u}_m) \cdot grad(\Psi). \tag{2.26}$$

The only deviation from this rule arises with the free surface, kinematic boundary condition, given in equation 2.12, where we only have a convective term in the horizontal directions (Gagliardini et al., 2013). That is,

$$\frac{\partial z_s}{\partial t} + (u_s - u_m)\frac{\partial z_s}{\partial x} + (v_s - v_m)\frac{\partial z_s}{\partial y} - w_s = a_s. \tag{2.27}$$

2.3.2 Variational form of the Stokes equations

The remaining derivation of the FEM applied to the Stokes equations are based on the process outlined by Mitchell (2012) and more generally by Zwinger (2011) of the Center for Science in Finland and his endlessly helpful presentations on glacier modeling and Elmer/Ice found on the Elmer/Ice website. The *strong* formulation of the Stokes equations for ice flow is given as,

$$\nabla \cdot \boldsymbol{u} = 0, \tag{2.28}$$

$$\nabla \cdot \boldsymbol{\tau} - \nabla p + \rho \boldsymbol{g} = 0. \tag{2.29}$$

In the Finite Element Method we seek to approximate the *weak* form of the partial differential equation(s). The weak form is a variational statement that satisfies the strong form on average over the domain rather than giving the exact solution everywhere. To get the weak form of the Stokes equation, we integrate the strong form over the domain against a test function. This

test function, which we'll call $\boldsymbol{v}$, can be any vector field whose components are all differentiable. First we write equation 2.29 in variational form,

$$-\int_\Omega (\nabla \cdot \boldsymbol{\tau}) \cdot \boldsymbol{v} + \int_\Omega (\nabla p) \cdot \boldsymbol{v} = \rho \int_\Omega \boldsymbol{g} \cdot \boldsymbol{v}. \tag{2.30}$$

We now rewrite the first term by exploiting the inherent symmetry of the deviatoric stress tensor,

$$\begin{aligned} -\int_\Omega (\nabla \cdot \boldsymbol{\tau}) \cdot \boldsymbol{v} &= -\int_\Omega \frac{\partial \tau_{ij}}{\partial x_j} v_i \\ &= \int_\Omega \tau_{ij} \frac{\partial v_i}{\partial x_j} - \frac{\partial}{\partial x_j}(\tau_{ij} v_i) \\ &= \int_\Omega \tau_{ji} \frac{\partial v_i}{\partial x_j} - \nabla \cdot (\boldsymbol{\tau} \cdot \boldsymbol{v}) \\ &= \int_\Omega \boldsymbol{\tau} : \nabla \boldsymbol{v} - \nabla \cdot (\boldsymbol{\tau} \cdot \boldsymbol{v}). \end{aligned} \tag{2.31}$$

We can also rewrite the second term as,

$$\begin{aligned} \int_\Omega (\nabla p) \cdot \boldsymbol{v} &= \int_\Omega \frac{\partial p}{\partial x_i} v_i \\ &= \int_\Omega \frac{\partial}{\partial x_i}(p v_i) - p \frac{\partial v_i}{\partial x_i} \\ &= \int_\Omega \nabla \cdot (p \boldsymbol{v}) - p \nabla \cdot \boldsymbol{v}. \end{aligned} \tag{2.32}$$

Combining equations 2.31 and 2.32, and using the divergence theorem we arrive at,

$$
\begin{aligned}
-\int_\Omega (\nabla \cdot \boldsymbol{\tau}) \cdot \boldsymbol{v} + \int_\Omega (\nabla p) \cdot \boldsymbol{v} &= -\int_\Omega \boldsymbol{\tau} \cdot \nabla \boldsymbol{v} - \nabla \cdot (\boldsymbol{\tau} : \boldsymbol{v}) + \int_\Omega \nabla \cdot (p\boldsymbol{v}) - p\nabla \cdot \boldsymbol{v} \\
&= \int_\Omega (\boldsymbol{\tau} : \nabla \boldsymbol{v}) - \int_\Omega (p\nabla \cdot \boldsymbol{v}) - \int_\Omega \nabla \cdot (\boldsymbol{\tau} \cdot \boldsymbol{v} - p\boldsymbol{v}) \\
&= \int_\Omega (\boldsymbol{\tau} : \nabla \boldsymbol{v}) - \int_\Omega (p\nabla \cdot \boldsymbol{v}) - \int_\Gamma \boldsymbol{n} \cdot (\boldsymbol{\tau} \cdot \boldsymbol{v} - p\boldsymbol{v}) \\
&= \int_\Omega (\boldsymbol{\tau} : \nabla \boldsymbol{v}) - \int_\Omega (p\nabla \cdot \boldsymbol{v}) - \int_\Gamma \underbrace{\boldsymbol{n} \cdot (\boldsymbol{\tau} - p\boldsymbol{I})}_{\boldsymbol{t}} \cdot \boldsymbol{v}.
\end{aligned}
\tag{2.33}
$$

We look to replace the deviatoric stress with the strain rate and eventually velocity via Glen's flow law. Recall that the strain rate is the symmetric part of the Jacobian of velocity, that is $\dot{\boldsymbol{\epsilon}} = \frac{1}{2}(\nabla u + \nabla u^T)$. We can now state our variational problem in terms of the velocity and pressure,

$$
\begin{aligned}
\int_\Omega (2\eta\dot{\boldsymbol{\epsilon}} : \nabla \boldsymbol{v}) - \int_\Omega (p\nabla \cdot \boldsymbol{v}) - \int_\Gamma \boldsymbol{t} \cdot \boldsymbol{v} &= \int_\Omega (2\eta \cdot \frac{1}{2}(\nabla \boldsymbol{u} + \nabla \boldsymbol{u}^T) : \nabla \boldsymbol{v}) - \int_\Omega (p\nabla \cdot \boldsymbol{v}) - \int_\Gamma \boldsymbol{t} \cdot \boldsymbol{v} \\
&= \int_\Omega (\eta(\nabla \boldsymbol{u} + \nabla \boldsymbol{u}^T) : \nabla \boldsymbol{v}) - \int_\Omega (p\nabla \cdot \boldsymbol{v}) - \int_\Gamma \boldsymbol{t} \cdot \boldsymbol{v}
\end{aligned}
\tag{2.34}
$$

Using a similar test function q for pressure p we can state our variational problem and say that the pair $(\boldsymbol{u}, p)$ is a weak solution that solves the variational problem if for all $(\boldsymbol{v}, q)$ we have

$$
\int_\Omega (\eta(\nabla \boldsymbol{u} + \nabla \boldsymbol{u}^T) : \nabla \boldsymbol{v}) - \int_\Omega (p\nabla \cdot \boldsymbol{v}) - \int_\Gamma \boldsymbol{t} \cdot \boldsymbol{v} = \rho \int_\Omega \boldsymbol{g} \cdot \boldsymbol{v}, \tag{2.35}
$$

and

$$
\int_\Omega q\nabla \cdot \boldsymbol{u} = 0. \tag{2.36}
$$

2.3.3 Conversion from a continuous to a discrete problem

The variational problem above is stated as a continuous problem that may not have an exact solution available, but we can discretize the problem and state it in terms of a finite-dimensional

vector space. For simplicity the operator $\boldsymbol{D}$ is introduced in that,

$$\boldsymbol{D}(\nabla \boldsymbol{u}) = \nabla \boldsymbol{u} + \nabla \boldsymbol{u}^T. \tag{2.37}$$

We now introduce the following weighting functions to discretize our problem,

$$\boldsymbol{u} = \sum_{\beta} \boldsymbol{u}_\beta \Psi_\beta \tag{2.38}$$

and

$$p = \sum_{\beta} p_\beta \chi_\beta. \tag{2.39}$$

Following the standard Galerkin Method, the first term in equation 2.35 can be written as

$$\sum_{\beta} \boldsymbol{u}_\beta \left(\int_\Omega (\eta \boldsymbol{D}(\nabla \Psi_\beta) : \nabla \Psi_\alpha) = \sum_{\beta} A_{\alpha\beta} \boldsymbol{u}_\beta \right. \tag{2.40}$$

by choosing our test function to be the basis function in equation 2.38, i.e. $\boldsymbol{v} = \Psi_\alpha$. Keeping with this definition of $\boldsymbol{v}$ our second term in equation 2.35 becomes,

$$\sum_{\beta} p_\beta \left(- \int_\Omega \chi_\beta \nabla \cdot \Psi_\alpha \right) = \sum_{\beta} B_{\alpha\beta} p_\beta. \tag{2.41}$$

Choosing our other test function q to be the basis function for pressure, χ_α in equation 2.39, and substituting into equation 2.36 we obtain

$$\sum_{\beta} \boldsymbol{u}_\beta \int_\Omega \chi_\alpha \nabla \cdot \Psi_\beta = \sum_{\beta} B_{\beta\alpha} \boldsymbol{u}_\beta \tag{2.42}$$

Letting $f = \int_\Gamma \boldsymbol{t} \cdot \Psi_\alpha + \rho \int_\Omega \boldsymbol{g} \cdot \Psi_\alpha$, we can write our system in block matrix form

$$\begin{pmatrix} A & B \\ B^T & 0 \end{pmatrix} \begin{pmatrix} \boldsymbol{u} \\ p \end{pmatrix} = \begin{pmatrix} f \\ 0 \end{pmatrix}. \tag{2.43}$$

Since $\boldsymbol{S} = \begin{pmatrix} A & B \\ B^T & 0 \end{pmatrix}$ is not positive definite, we must check if $\boldsymbol{S}^{-1}$ is well behaved. Solving the first row in 2.43 we see that

$$A\boldsymbol{u} + Bp = f \implies \boldsymbol{u} = A^{-1}(f - Bp) \tag{2.44}$$

and that the second row is

$$B^T\boldsymbol{u} = 0. \tag{2.45}$$

Combining the two previous equations we obtain

$$B^T A^{-1} B \cdot p = B^T A^{-1} f \tag{2.46}$$

and we are interested to see if $B^T A^{-1} B$ is well-behaved. To check if our problem is well-posed we use the *inf-sup* condition,

$$\inf_p \sup_{\boldsymbol{u}} \frac{p^T B\boldsymbol{u}}{(\boldsymbol{u}^T A\boldsymbol{u})(p^T p)} \geq A^{-1}. \tag{2.47}$$

The stability depends on our test functions, but when using the Standard Galerkin Method, applied to the Stokes equations, we do not satisfy the stability criteria above (Howell and Walkington, 2011). Therefore we must use some stabilization method in order to compute a solution for the system. Two types of stabilization methods are commonly used (1) the residual free methods or (2) the residual free bubbles method. In this thesis (specified in simulation runs given in section 3.5), the residual free bubbles method is employed, which simply adds additional degrees of freedom to our system. Note that the residual free bubbles method is actually applied during the free surface calculations, while during the Stokes calculations, an external library uses its own stabilization method.

2.4 Geostatistics

The geostatistical methods of spatial structure analysis using variography and grid estimation using ordinary kriging are applied to derive Digital Elevation Models (DEMs) of the ice surface and bedrock of the Bering-Bagley Glacial System (Herzfeld, 1992, 2004; Journel and Huijbregts, 1989; Matheron, 1963). The underlying concept of geostatistics is that of the regionalized variable. A regionalized variable $z(x)$ is a spatial variable (a variable defined over $\mathcal{R}^2$ or $\mathcal{R}^3$, the two- or three-dimensional space of real numbers) with a transitional behavior between deterministic and random states. For example, CryoSat-2 altimeter data $z_i(x)$, where $i = 1, \ldots, n$, on $z(x)$ may be considered a realization of a spatial random function $Z(x)$ for $x \in D$ with the property that

$$(Z(x) - Z(x+h)) \tag{2.48}$$

is a second order stationary random function for fixed $h \in \mathcal{R}^2$ such that $x, x+h \in D$,

where the glacier region D is a subset of $\mathcal{R}^2$. The property given in 2.48 is called the *intrinsic hypothesis*.

2.4.1 Spatial structure analysis

Variogram analysis is applied to examine the spatial structure of elevation either at the surface or bed of a glacier. Under the intrinsic hypothesis, the *(semi-) variogram*

$$\gamma(h) = \frac{1}{2} E[Z(x) - Z(x+h)]^2 \tag{2.49}$$

exists and is finite, γ measures the spatial continuity (E denotes the mathematical expectation). In practice, an experimental variogram is calculated from the data set, according to the formula

$$\gamma(h) = \frac{1}{2n} \sum_{i=1}^{n} [z(x_i) - z(x_i + h)]^2 \tag{2.50}$$

where $z(x_i)$, $z(x_i + h)$ are samples taken at locations x_i, $x_i + h \in D$ respectively, where n is the number of pairs separated by $h \in \mathcal{R}^2$. Coordinates are in an orthogonal coordinate system. For this analysis, the Universal Transverse Mercator (UTM) System is used.

Variogram models are then fitted to the experimental variograms. Variogram models are characterized by their function type (which ensures that the positive definiteness condition of kriging is satisfied and hence that the inversion step in the kriging problem has a unique solution, see Herzfeld (2004)). The Gaussian model is best suited for kriging of glacier surfaces at a scale that does not resolve crevasse fields (Herzfeld et al., 1993). The Gaussian variogram model is given by the equation

$$\gamma_{gau}(h) = c_0 + c_1(1 - e^{\frac{-h^2}{a^2}}), \tag{2.51}$$

where c_0 is the *nugget effect*, a is the *range*, and $c_0 + c_1$ is the *sill*.

2.4.2 Kriging

Estimation of surface elevation at a given location $x_0 \in D$ is performed by kriging. Kriging, named after the pioneering geostatistician Danie Krige, is a family name for least-squares-based estimators, the general linear estimator is

$$Z_0^* = \alpha_0 + \sum_{i=1}^{n} \alpha_i \, Z(x_i) \quad \text{with} \quad \alpha_i \in \mathcal{R} \tag{2.52}$$

where weights are determined by a minimum variance criterion

$$min(E[Z_0^* - Z_0]^2) \tag{2.53}$$

and with respect to unbiasedness conditions $E[Z_0^* - Z_0] = 0$.

The estimation variance is

$$\begin{aligned} \text{var}[\varepsilon_0] &= \text{var}[Z_0 - Z_0^*] \\ &= \text{var}[Z_0] \\ &\quad -2\sum_{i=1}^{n} \alpha_i \, \text{cov}[Z_0, Z_i] \\ &\quad + \sum_{i,j=1}^{n} \alpha_i \, \alpha_j \, \text{cov}[Z_i, Z_j]. \end{aligned} \tag{2.54}$$

The covariances in equation 2.54, however, are not known. The salient concept in kriging is to replace the unknown covariances by "known" variogram values. The variogram values are taken from the model. Mathematically, this is justified by the intrinsic hypothesis. Using the notation

$$\begin{aligned} \gamma_{0i} &= \gamma(x_0 - x_i) \\ \gamma_{ij} &= \gamma(x_i - x_j) \\ &\text{for } i, j = 1, \ldots, n \end{aligned} \tag{2.55}$$

minimization of the estimation variance yields a matrix equation (or n conditions). The unbiasedness conditions depend on the information available on the expectation of $Z(x)$.

Unknown but constant expectation $0 \neq E = E[Z(x)]$ for all $x \in D$ leads to the unbiasedness condition

$$\begin{aligned} \sum_{i=1}^{n} \alpha_i &= 1 \\ \\ \alpha_0 &= 0. \end{aligned} \tag{2.56}$$

A solution satisfying the n conditions from equations 2.52, 2.53 and 2.54 and the unbiasedness condition 2.56 is obtained from a system of $(n+1)$ linear equations (kriging system), using a Lagrange parameter λ:

$$\begin{pmatrix} \gamma_{11} & \ldots & \gamma_{1n} & 1 \\ \vdots & \ddots & \vdots & \vdots \\ \gamma_{n1} & \ldots & \gamma_{nn} & 1 \\ 1 & \ldots & 1 & 0 \end{pmatrix} \begin{pmatrix} \alpha_1 \\ \vdots \\ \alpha_n \\ \lambda \end{pmatrix} = \begin{pmatrix} \gamma_{01} \\ \vdots \\ \gamma_{0n} \\ 1 \end{pmatrix}. \tag{2.57}$$

This is the most commonly applied form of kriging, known as *ordinary kriging*, the matrix in 2.57 is the *(ordinary) kriging matrix*.

The kriging equation 2.57 has a unique solution if positive-definite variogram models are used to build up the kriging matrix. Such models include the Gaussian model (equation 2.51), which is employed in subsequent analysis.

Chapter 3

Experimental Design

3.1 Experimental overview

The ultimate goal of this study is to create an accurate model of the Bering-Bagley Glacial System that provides insight into the surge process. In particular, we want to know when, where, how and why the glacier surges. To accomplish this task, a variety of input parameters and physical descriptions of ice behavior will be implemented and verified against the collection of observations and analysis done previously on the BBGS surges (specifically, Burgess et al. (2012); Herzfeld et al. (2013a); Molnia and Post (2010a,b); Muskett et al. (2009); Turrin et al. (2013)).

Before any simulations can be performed, an accurate description of the glacier's shape must be created. That is, we need to specify the boundaries of the system, or more specifically, attain a contour outline of the glacier as well as bedrock and initial surface topography. A large portion of this thesis is dedicated to the creation of these surface and bed topographies, or Digital Elevation Maps (DEMs), using satellite and airborne altimeter data. Production and analysis of multiple surface DEMs from different times of the surge (2011-2013) and subsequent derived elevation difference maps will also be used as verification of the model. These DEMs can provide a variety of initial inputs for the model. The course of data acquisition, data processing and geo-mathematical methods that need to be done to create the Digital Elevation Maps are explained

first followed by a detailed description of how the modeling experiments will be conducted and computed.

3.2 Field work: Airborne observations

Field data, including altimeter data and imagery, were collected during four expeditions to Bering Glacier by Dr. Herzfeld and her students. I was able to participate in the third such campaign. In late June of 2012, a group from our lab consisting of Dr. Herzfeld, her daughter Almut, myself and two fellow students Brian McDonald and Griffin Hale, drove to Alaska to conduct a field campaign over the BBGS. After taking a ferry to the small town of Cordova, we flew a small aircraft, which was equipped with a laser altimeter operating at 400 Hz aimed out of circular hole in the bottom of the plane, over the BBGS. Armed with a photographic camera, my job was to take as many pictures of close up crevasse patters as I could while Dr. Herzfeld took pictures of the surge features and other large scale characteristics of the glacier. These images are used throughout this thesis to validate derived glacier behavior.

FIGURE 3.1: **Pictures from the summer 2012 Bering Glacier campaign.** (Left) Me getting ready for take off. (Right) The small aircraft flown over Bering Glacier by pilot Terry Kennedy.

Similar campaigns in fall 2011 and fall 2012 used a different laser altimeter (also operating at 400 Hz) and captured similar photos as described above. The laser used in the summer campaign had a lower pulse rate whose optics were too small to yield sufficient elevation measurements for proper analysis and hence any altimeter data used in this thesis came from fall 2011 and fall 2012 (Herzfeld et al., 2013a).

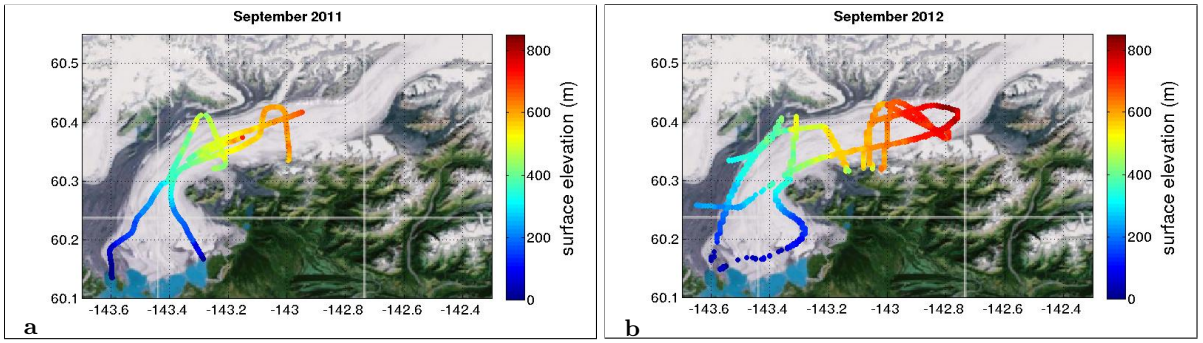

FIGURE 3.2: **Airborne laser altimeter elevation data from fall campaigns.** (a) Fall 2011, (b) fall 2012.

3.3 Derivation of Digital Elevation Maps and other model inputs

3.3.1 Data sources

3.3.1.1 Surface data: CryoSat-2 SIRAL data

While the glacier bedrock does not change on the timescale we are interested in, the glacier surface is constantly changing throughout the seasons not to mention during the surge process itself. Therefore multiple surface DEMs can be derived that correspond to different time periods. A total of four surface DEMs are created to represent the glacier surface during the summer and winter seasons between May 2011 and April 2013 and are derived from CryoSat-2 measurements. Until this study, CryoSat-2 data have only been used to study sea-ice over the arctic and antarctic regions. This is the first analysis that uses data measured over land-ice and mountain regions. Therefore a complete error analysis will be necessary to determine the accuracy and reliability of these measurements, which is done in section 4.2.

The European Space Agency's (ESA's) CryoSat-2 mission is an Earth Explorer Mission launched on April 8th, 2010. The main payload of CryoSat-2 is the synthetic-aperture, interferometric altimeter (SIRAL), a new type of sensor designed to collect altimeter data in three modes: LRM (low resolution mode), SAR mode (SARM) and synthetic aperture interferometric mode

(SARInM). In LRM, the SIRAL operates like a conventional pulse-limited radar altimeter. In the other two modes, SAR-type formation and processing of the signal is employed to increase resolution in the along-track direction to 250 m (300 m in the Bering Glacier area). Over critical areas of the margins of the ice sheets, SIRAL data are collected in SARIn mode, which is the most interesting capability of the SIRAL instrument. Designed to better capture surface elevation in sloping areas, SIRAL receives data using two antennas, which facilitates identification of ground returns off nadir (which is impossible with conventional altimetry) (Drinkwater et al., 2004; ESA, 2007; Wingham et al., 2004, 2006). The 250 m spacing is a great improvement over ERS-1/2 radar altimeter data spacing, which is about 5 km, whereas GLAS (Geoscience Laser Altimeter System) data have an along-track spacing of 173 m. In across-track direction, the area from which the energy is returned is as large as the footprint, which is up to 15 km, depending on surface roughness.

The SIRAL instrument is a 13.6 GHz normal-incidence radar altimeter with a single transmit unit and two receive chains, including two slightly elliptical antennas elongated in along-track direction and offset by 1 m in the across-track direction. In LRM, it operates with a pulse-repetition frequency (PRF) of 1.971 kHz and sends out 350 MHz chirps. In LRM and SARM, the measurement and tracking spectrum spans a range window of 60 m with 0.469 m range resolution. Hence the best accuracy that can be expected is about 0.5 m.

In SARIn mode, bursts of 64 pulses of the same 18.182 PRF are transmitted, but at a slower burst repetition rate than for the SAR mode, and both receiving chains are employed. The processing is described in detail in Wingham et al. (2006). In essence, since the two antennas are spaced 1 m in the across-track direction, the angle of arrival can be measured in addition to the slant range, which allows determination of the ground location of the point of first return in the across-track direction, in addition to elevation at that point. As a result, there is one point per along-track location, but the ground location is not necessarily at nadir. This effect can be seen in the data of Bering Glacier (figure 3.7 and figure 3.8). This information is provided in the level-2 data, which are used in this study (ESA, 2007).

CryoSat-2 was launched into a 717.2 km altitude orbit with 92° inclination. CryoSat-2's geographic coverage extends to 88° N/S, which facilitates study of polar regions. The repeat period is 369 days, with a 30-day subcycle; inter-track spacing at the equator is 7.5 km.

Data acquisition is conducted using geographic masks, which have been determined by the ESA in communication with the CryoSat-2 PIs. Alaska is entirely within the SARInM mask, which is ideal for studies of elevation changes of the BBGS during the surge cycle.

In SARIn mode, the across-track offset of the echoing point can be determined directly using phase information. In the L2 SARIn data, the 20 Hz latitude and longitude values (fields 32 and 33 in the L2 data product) provide the estimated position of the return (as computed from the phase difference) and not the nadir. The nadir location is only present in the L2 data at 1 Hz (fields 3 and 4). As a result of this effect, ground locations may appear up-hill and across-track from the nadir locations on the track. It is important to note that phase-wrapping will occur when the across-track offset is large enough and this will have the effect of the echo appearing to come from the other side of the ground track. For Greenland and Antarctica, the effect of phase-wrapping is flagged by use of an ambiguity DEM that shows where this effect is likely to occur, however such DEMs are not available for Alaska and hence phase-wrapping may affect the CryoSat-2 data over Bering Glacier. If one observes a sequence of records with increasing across-track offset and then an abrupt switch to the other side of the track, it is likely that phase-wrapping has occurred. Data on the glacier clustering to one side of the track hint that they are good returns without phase-wrap (pers. comm. Enrica Cocco, ESA).

The elevation data received from the CryoSat-2 mission is shown in section 3.3.2.

3.3.1.2 Bedrock data

Three different ice thickness measurement data sets are used in this study. Based on derived surface DEMs from their respective airborne campaigns, bedrock elevation can be derived from the ice thickness measurements.

The first such campaign was conducted in March 2006 by Dr. Howard Conway of the University of Washington and used a monopulse radar system attached to a small plane in order to gather ice thickness measurements along the centerline of Bering Glacier, as well as a few transverse cross sections (Conway et al., 2009). These thickness measurements, and the derived surface and bed elevation data, were generously made available for use in this study thanks to Dr. Conway. Figure 3.3 shows the bedrock elevation measurements from the 2006 flight.

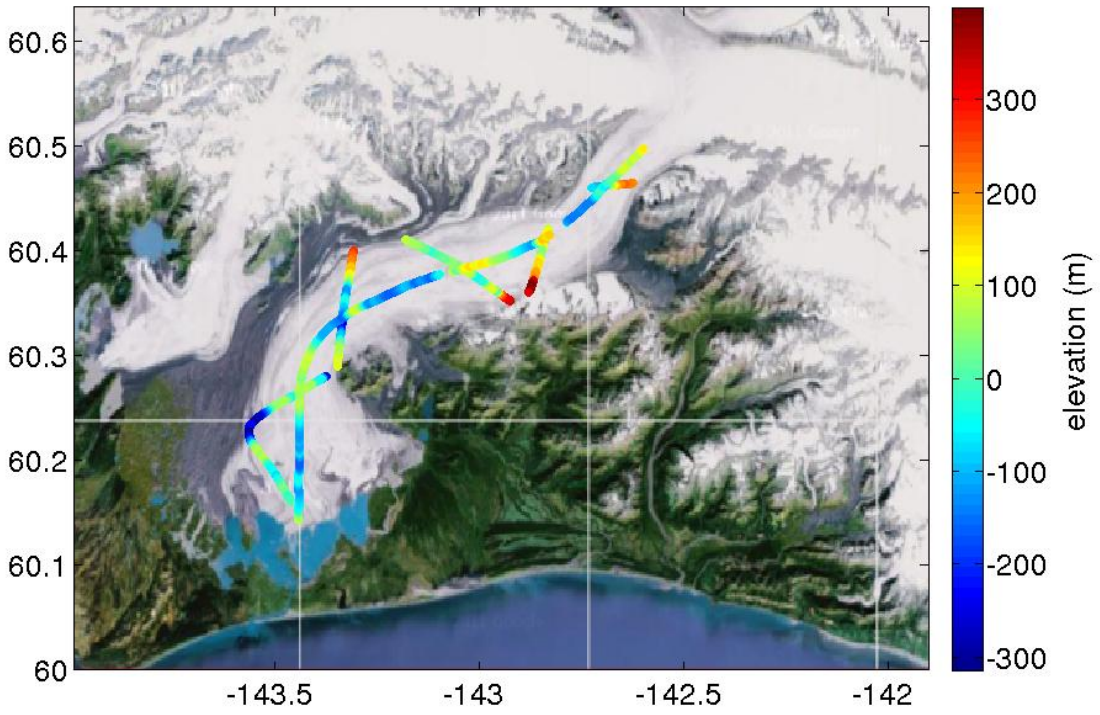

FIGURE 3.3: **Bedrock elevation measurements from the March 2006 campaign over Bering Glacier from Dr. Howard Conway of the University of Washington.**

Another measurement of the bed elevation of Bering Glacier was given by Dr. Bruce Molnia (United States Geological Survey) (Molnia and Post, 1995). Only 37 measurements were obtained, but some were done at places not flown over by the other two campaigns and therefore their addition will provide a better DEM from kriging. These data are shown in figure 3.4.

The campaign that yielded the most coverage and the only coverage in the Bagley Icefield, is the JPL WISE campaign. NASA's Jet Propulsion Laboratory (JPL) deployed the ice penetrating radar system called the Wide-field Infrared Survey Explorer (WISE) in 2008 and 2012 to investigate ice thickness in temperate glaciers in southeast Alaska. The radar operates at 2.5 MHz and consists of a single transmitter and receiver that operates on a dipole antenna that dangles from the back of an airplane (Rignot et al., 2013). Thanks are due to Eric Rignot and Jeremie Mouginot as part of the NASA Operation IceBridge (OIB) mission for making this valuable data available for this study in the fall of 2013. Because this data was not attained until late in the study, an ideal bedrock DEM could not be created that included treatment of sub-glacial

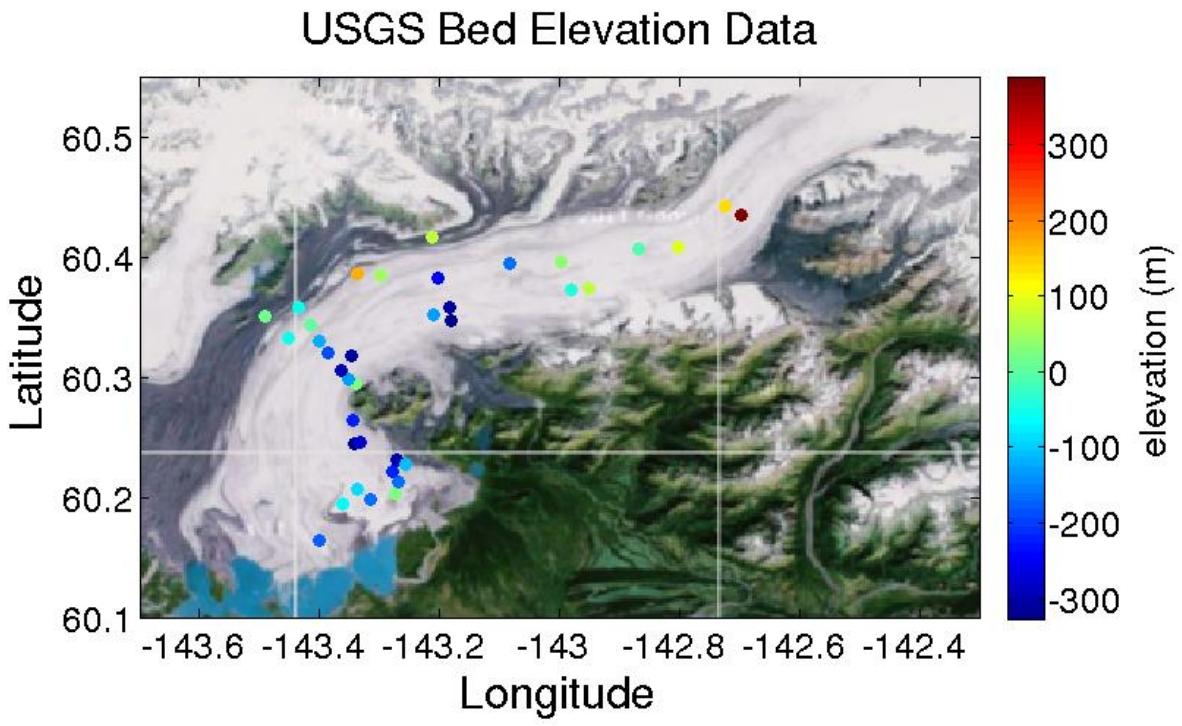

FIGURE 3.4: **Bedrock elevation measurements from the the USGS.**

troughs using the cutting edge algorithm developed by our lab group. The creation of better bedrock topography using the trough-altgorithm could serve as a first extension to this study.

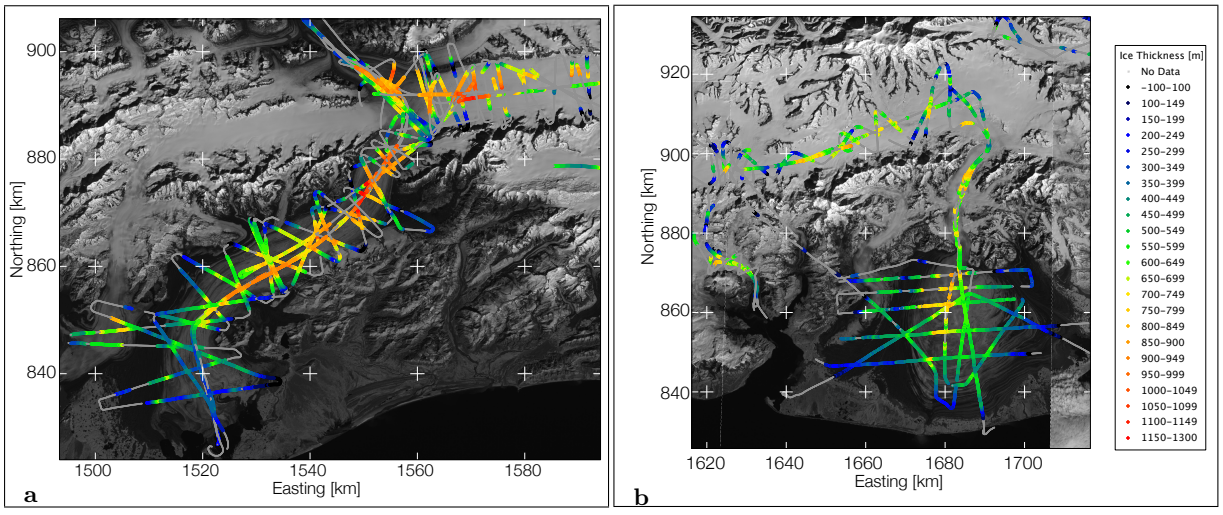

FIGURE 3.5: **Airborne radar ice thickness data from JPL.** (a) Radar measurements over Bering Glacier, (b) Radar measurements over the Bagley Icefield (top) and Malaspina Glacier (bottom).

It is fair to assume that the bedrock elevation would not be changing in any significant way over the span of these three separate measurements. Therefore, the data from all three sources are combined and are used to derive a bedrock DEM for the glacier model (see section 4.1.3). However, the different data sets may have different error characteristics, which would require a more in-depth analysis of the bedrock topography. Since the JPL 2008/2012 data only became available in fall 2013, this is left for a later study.

3.3.1.3 Glacier contour outline

A contour outline of the glacier is needed in order to define the lateral boundaries of the BBGS. This was done using paper, a pencil, a straight edge and a 1:250,000 scale contour map created by the USGS of the BBGS in 1983 (Survey, 1983). A total of 109 points were measured and linearly interpolated by the modeling software in order to define the boundary (see figure 3.6). The outline of the glacial system remains constant on scales we are interested in everywhere except at the terminus where calving occurs. This project does not consider calving and the changing terminus but the thesis could be extended to allow for calving by allowing mass flux through the boundary there or by allowing an evolving terminus by making that boundary a free surface.

3.3.2 Data processing

3.3.2.1 CryoSat-2 processing

Because rapid and large elevation changes are characteristic of a surge, frequent observation and mapping of surface elevation are desirable to document elevation changes during the surge process. However, CryoSat-2 data, while being acquired continuously, do not yield sufficient spatial coverage to allow monthly elevation mapping.

Figure 3.7 shows the coverage of the CryoSat-2 data for different time intervals. The data for one-month and three-month intervals do not provide adequate coverage to create a surface map

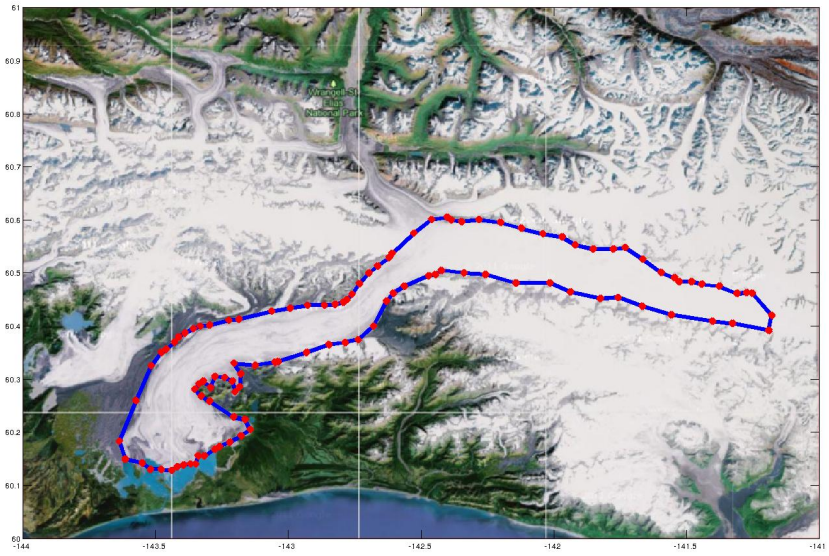

FIGURE 3.6: **BBGS contour outline.** The red diamonds indicate the measured points along the edges of the glacier used in the creation of the lateral boundary (blue) for the model.

using kriging (see section 2.4.2). If data from six-month time intervals are used, coverage of the area is sufficient for derivation of a DEM, which is justified in section 4.2 on error analysis.

CryoSat-2 altimeter data, useful for geophysical research, start in February 2011. Two years of data are used from May 2011 to April 2013, divided into four six-month intervals: May 2011 - October 2011 (summer 2011), November 2011 - April 2012 (winter 2011/12), May 2012 - October 2012 (summer 2012), and November 2012 - April 2013 (winter 2012/13). The reason for these divisions arises from the local weather patterns near Bering Glacier, Alaska. In the months of May-October, the region around Bering Glacier receives precipitation as rain, and in November-April as snow (accumulation).

3.3.2.2 Spatial scattering of ground-track locations

The left column of figure 3.8 shows the raw, unfiltered data over Bering Glacier for the four six-month intervals. Closer scrutiny of the data distribution in figure 3.8 shows that data points may follow straight lines, as seen in the summer 2011 data set (figure 3.8 (a)), or may appear to be scattered around lines, as is the case for summer 2012 data (figure 3.8 (e)). The data

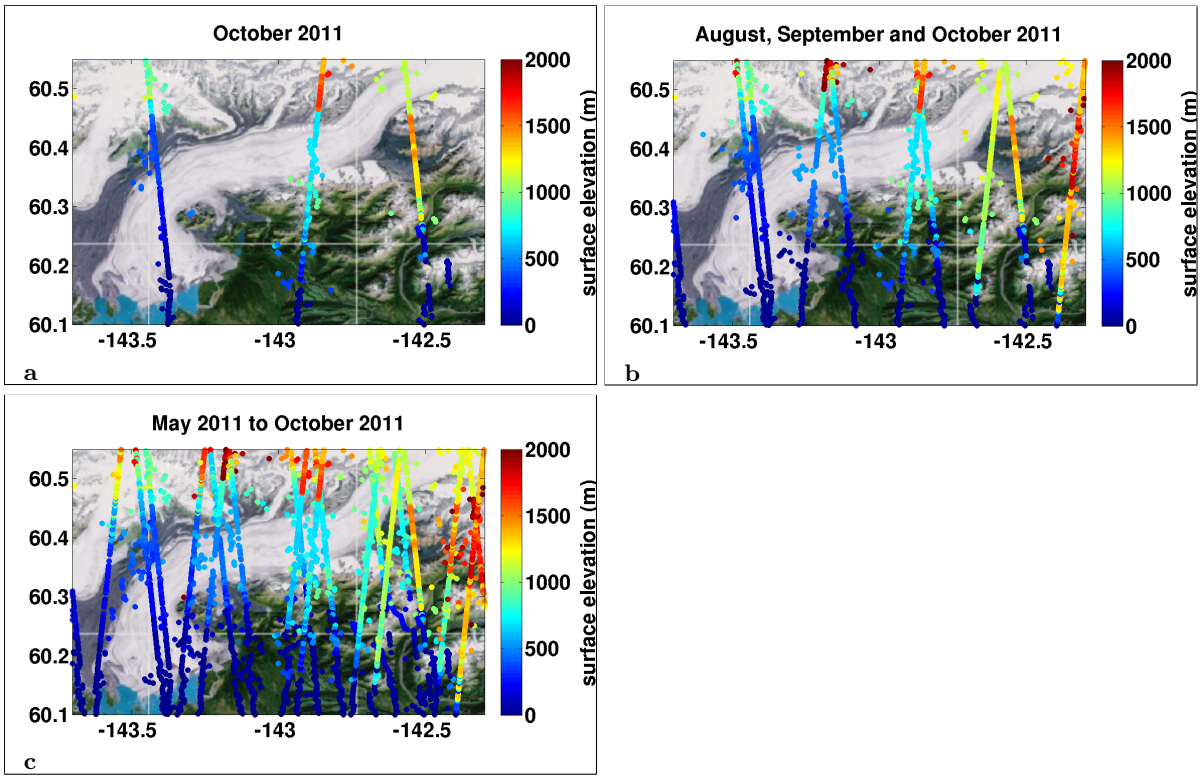

FIGURE 3.7: **CryoSat-2 ground tracks over Bering Glacier, Alaska for various time intervals.** (a) CryoSat-2 ground tracks for a one-month period. There can be anywhere from 2 to 5 tracks over Bering Glacier per month but an average month has 3 or 4. (b) CryoSat-2 ground tracks for a three-month period. (c) CryoSat-2 ground tracks for a six-month period.

on Bering Glacier and Bagley Icefield appear not to be affected by phase wrapping, as for each track, the ground locations of received plots tend to scatter off to one side of a track without abrupt switching. A scattering of the ground locations around the cantorial track line is likely attributable to surface roughness. As location of crevasse fields change during the surge, surface roughness changes. This leads to different scattering patterns of the received signal's ground locations around the nadir track line, a consequence of the SAR-type processing. A comparison of figure 3.8 (a) (summer 2011, early surge phase) with figures 3.8 (e) and 3.8 (g) (summer 2012 and winter 2012/2013, mature surge phase) shows this scattering.

3.3.2.3 Filtering

On first inspection, there are some tracks and isolated points that arise suspicion due to their large (>200 m) elevation differences between nearby data. Based on contour maps produced by

the USGS (Survey, 1983), as well as laser altimeter data collected during 2011 and 2012 field campaigns (Herzfeld et al., 2013a), surface elevation over the glacier does not exceed 1200 m. Therefore any tracks dominated by elevation values higher than 1200 m are taken out of the data set, as well as any single data point exceeding that threshold. After application of this first filter, the resultant data sets that were used for creating elevation maps are shown on the right column of figure 3.8. Notice that the coverage is better in the latter two data sets than in the first two data sets, possibly CryoSat-2 performance or processing improved.

3.3.3 Variography

The variogram model is determined from the experimental variogram by application of a variogram fitting algorithm. To determine variogram models for the CryoSat-2 data, there are two possibilities: (a) to use six-month data sets and derive a variogram model for each one (red lines in figure 3.9), and use that in the analysis, or (b) to use the entire two-year data set to derive a single variogram model (green line in figure 3.9), which will be used to derive all four half-year DEMs. After following both paths, it was decided to use option (b), because it allows for a consistent error analysis (see section 4.2). Figure 3.9 shows that the difference in variogram models between options (a) and (b) is small.

First, global experimental variograms (i.e. variograms that consider all directions for pairs of points) are calculated from the entire two-year data set and then from each of the six-month data sets individually, using a lag (spacing) of 300 m, which matches the approximate average spacing of CryoSat-2 data in the study region. Bering Glacier, excluding the Bagley Icefield, is approximately 90 km long. 150 steps to a maximal lag of $300m \times 150 = 45,000m$ (equal to half the length of the domain of Bering Glacier) was used, because variograms for more than half the domain diameter may be affected by edge effects due to decreasing number of pairs for larger lags.

The Gaussian variogram applied in the data analysis, option (b), has parameters nugget = 125.69 m^2, sill = 601960.59 m^2 and range = 65992.11 m.

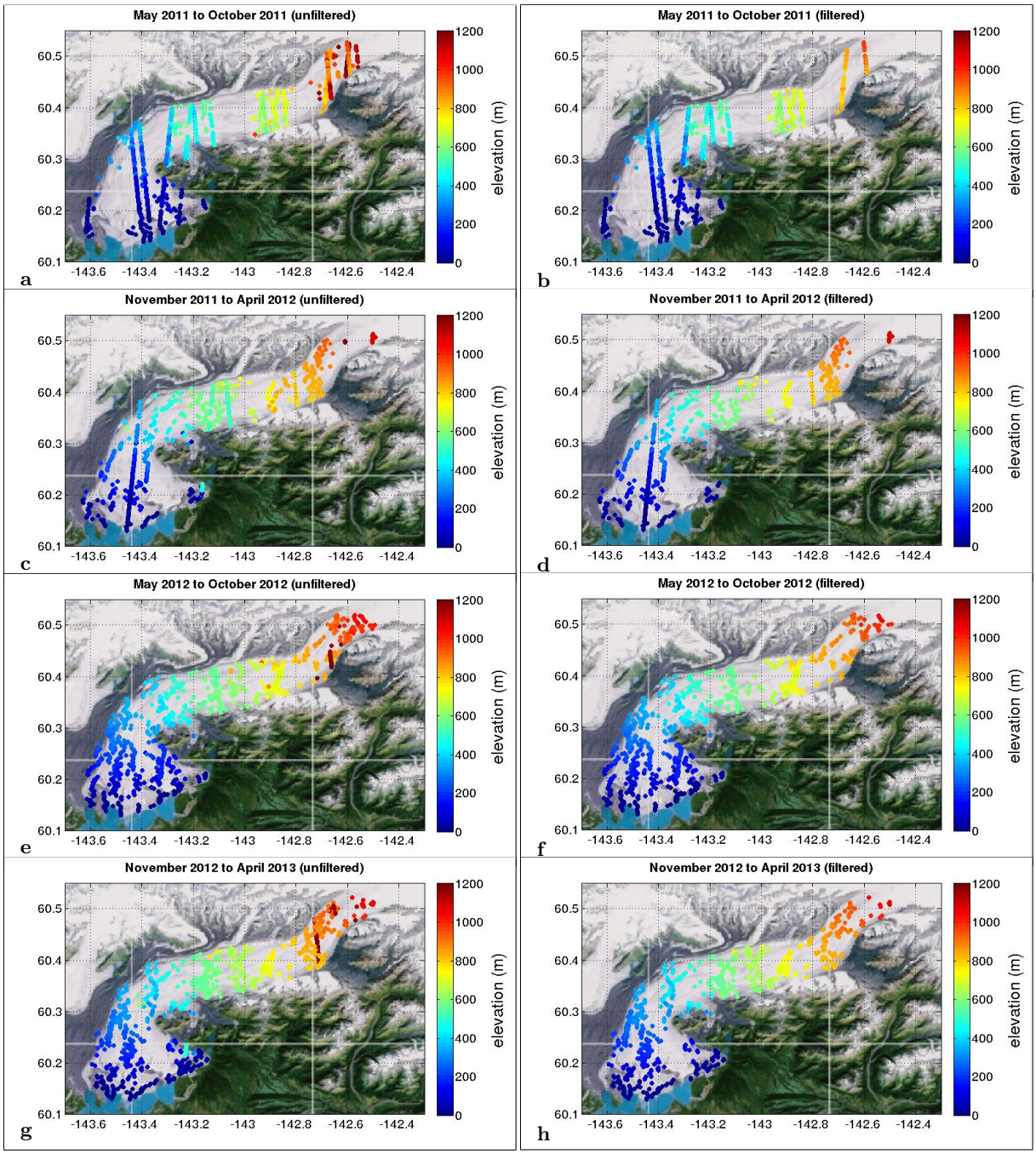

FIGURE 3.8: **Unfiltered (left) and filtered data (right) from the CryoSat-2 satellite over Bering Glacier, Alaska for four different six-month intervals.** (a) and (b) Summer 2011, (c) and (d) winter 2011/2012, (e) and (f) summer 2012, (g) and (h) winter 2012/2013.

Using these variogram parameters, a kriging algorithm is run using the elevation data from each data set. The resulting Digital Elevation Maps, shown in section 4.1.1, can now be used to derive

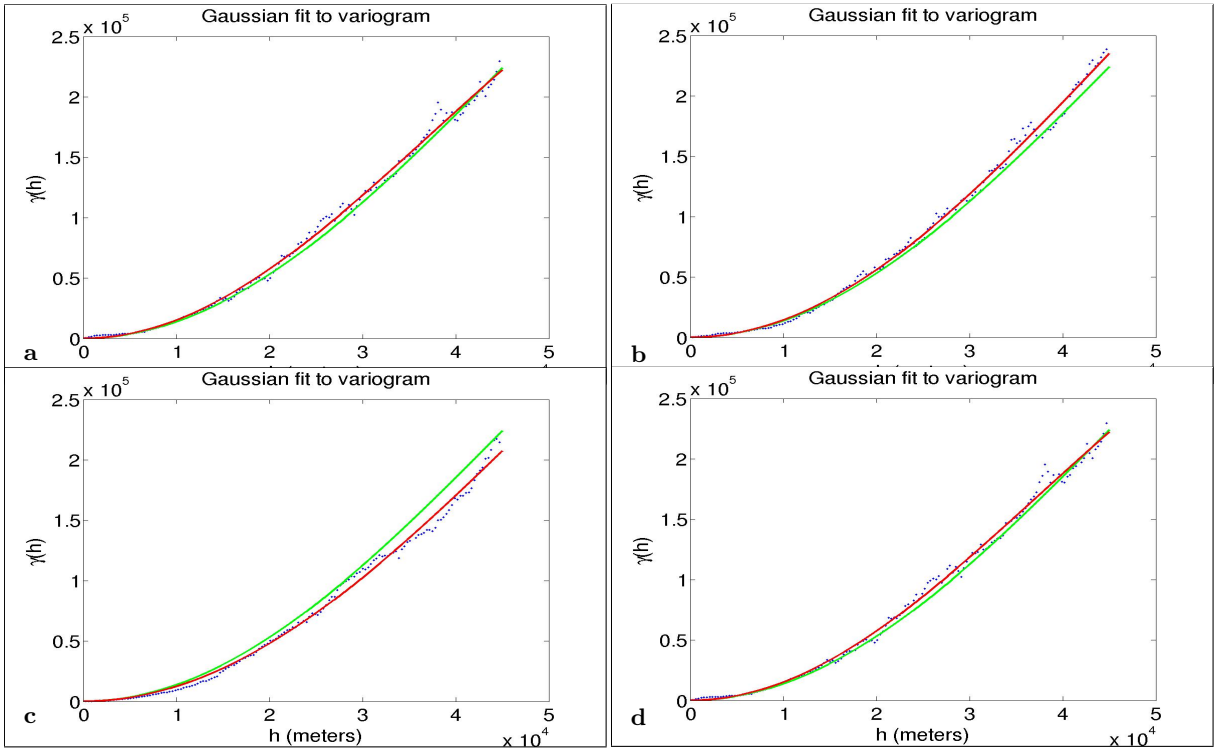

FIGURE 3.9: **Individual variogram models (red) of each of the data sets plotted with a single variogram model (green) based on spatial analysis done with all the data from May 2011 to April 2013.** For each subfigure the variogram values are: (a-d) Nugget = 125.69, Sill = 601960.59, and Range = 65992.11, (a) summer 2011: Nugget = 103.18, Sill = 434836.52, and Range = 53222.99 , (b) winter 2011/2012: Nugget = 56.83, Sill = 614706.60, and Range = 64840.26, (c) summer 2012: Nugget = 148.83, Sill = 630174.70, and Range = 71259.98, (d) winter 2012/2013: Nugget = 16.80, Sill = 616228.85, and Range = 65691.89.

initial glacier geometry for the model. Similarly, a Gaussian fit was made to the combined bed data, explained in section 3.3.1.2, whose variogram values were used as parameters for kriging a DEM for the bedrock. The Gaussian fit to the bed data is seen in figure 3.10, along with the derived variogram values, and the resulting bed DEM from kriging can be found in section 4.1.3.

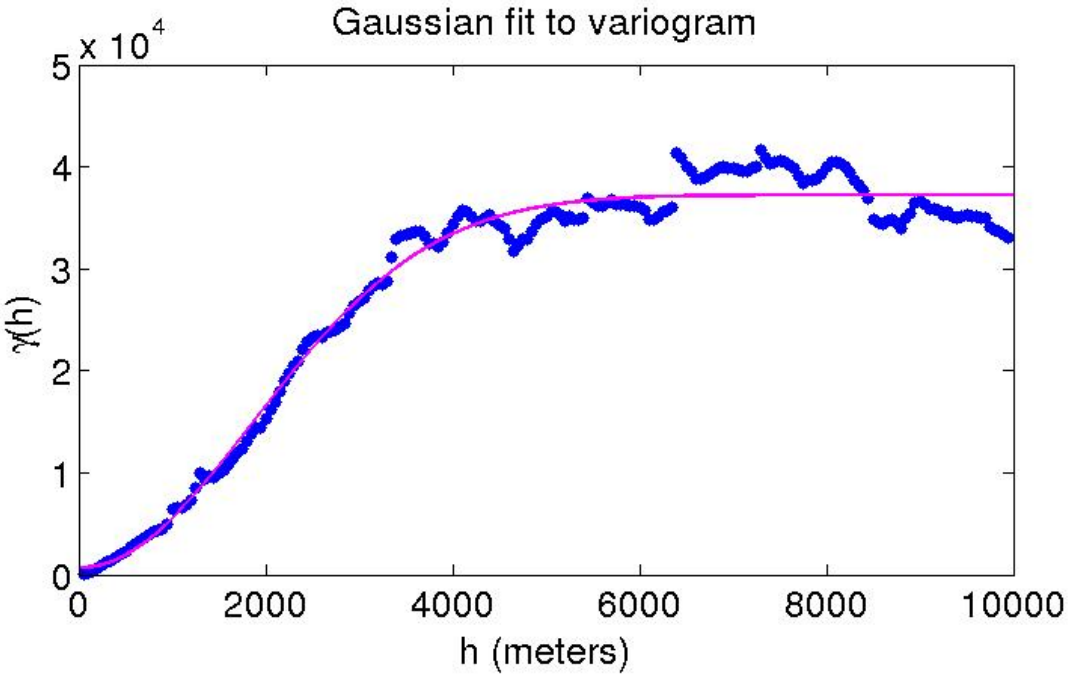

FIGURE 3.10: **Gaussian variogram fit to the combined bed elevation data.** Nugget = 679.35, Sill = 37226.32 and Range = 4601.00.

3.4 Software

An overview of the finite element software used for modeling is now given followed by a detailed description of how one uses the software for their specific modeling goals. This includes showing how to set up a simulation by defining the glaciological parameters, initial and boundary conditions, solvers, and so on. A brief description on the numerics of some solvers is also given.

3.4.1 Elmer

Elmer is open source, finite element software for multi-physical problems developed mainly by the Center for Science (CSC) in Espoo, Finland. Elmer was originally produced in 1995 with a collaboration of Finnish universities, research institutes and industry, and later became used internationally after its open source publication in 2005. Elmer uses the Finite Element Method (FEM) to solve many physical problems that involve Partial Differential Equations (PDEs) such as structural mechanics, fluid dynamics, heat transfer or electrodynamics. Elmer, being multi-physics software, provides solvers that can couple these physical phenomena and has also been made highly parallelizable, thus making it ideal for solving large and complex problems (Ruokolainen et al., 2013). Most of the code for Elmer is written in C and FORTRAN and uses a Solver Input File (SIF) as a way for the user to specify their model specifics and simulation needs.

3.4.2 Elmer/Ice

Elmer/Ice is the largest and most active community within Elmer that develops code specific to glaciological problems. It is a full-Stokes, finite element, ice sheet/ ice flow model mainly developed by the CSC as well as the Laboratoire de Glaciologie et Géophysique de l'Environnement (LGGE) in France and the Institute of Low Temperature Science (ILTS) at Hokkaido University in Japan (see Ruokolainen et al. (2013), Zwinger (2011), Gagliardini et al. (2013), Seddik et al. (2012), Gagliardini and Zwinger (2008), Ruokolainena et al. (2013)).

3.4.3 GMSH

There are several programs external to Elmer that are commonly used for pre and post-processing of Elmer solutions, the first of which is the three-dimensional finite element mesh generator called GMSH. It is used in the modeling process as a way to generate a fast, light and user-friendly mesh that can be easily used by Elmer during computation.

3.4.4 Paraview

Elmer has the ability to do its own post-processing and visualization using the built-in ElmerPost command, yet some users prefer to do post-processing using the program Paraview. Elmer can easily produce results with the appropriate format for Paraview by adding a simple solver to the input file (see section 3.5.4). Paraview is also open sourced and multi-platformed and was built in order to quickly build, visualize and analyze data qualitatively and quantitatively. Most figures in Chapter 4 that deal with results and analysis were generated using Paraview.

3.5 Specifics of the Solver Input File

This section aims to outline the solver input file (SIF), by going over an example of a SIF used in a particular model run on the BBGS, in order to show what needs to be specified to run a simulation (to see this specific SIF go to Appendix A). An overview of the various solvers that are used in simulation is given, as well a description of the various glaciological parameters, which can be seen as knobs to adjust ice flow behavior. A description of the material (ice), body force (gravity), initial conditions and boundary conditions is also given.

3.5.1 Simulation details

Since we expect our flow to be changing in time, we seek a transient solution set up on a three-dimensional Cartesian coordinate system. We have a choice of two different time stepping schemes: Backwards Difference Formulas (BDF) or the Crank-Nicholson method. Most experiments in this thesis use a BDF scheme of order one, also known as the Backwards Euler's

method, due to its speed and simplicity. The accuracy and speed of the results of the two methods are compared later in the thesis in section 4.3.1.5. So that one time step is temporally meaningful, the time step size was chosen to be one day (or 1/365 years). Simulations were carried out anywhere from 10 time step intervals, corresponding to ten days, to 9125 intervals, or 25 years, which compares to a full surge cycle for Bering Glacier.

3.5.2 Bodies, forces and initial conditions

We initially consider two distinct bodies: the main glacial body and the upper free surface of the glacier[1]. Both are made of ice but are treated separately since the physics and mathematics acting on the two parts of the glacier are different. The single force acting on the main body of ice is gravity, while the external force acting on the free surface is accumulation. Initial conditions can be manually set or specified by previous flow solutions using the result file that is created after every ElmerSolver run. If a initial condition is not given, it is assumed to be zero, and in most cases the pressure and initial velocity in each direction will be zero. The initial position of the free upper surface is given by the surface Digital Elevation Map derived in section 3.3.2 and shown in section 4.1.1, and is read into the SIF file using a user defined function.

3.5.3 Material

Both bodies use the same material description of temperate ice. Temperate ice implies that ice temperatures are near the freezing point of water due to their location outside of the polar ice caps where ice can be much colder (referred to as polar ice). The temperature distribution is assumed to be constant in this model and is set to $-1°C$. A natural extension to the model could solve for a non-uniform temperature distribution throughout a glacier as Elmer/Ice provides such solvers. It is in this section that we define Glen's flow law; the viscosity model that describes ice deformation (see section 2.2.3). A final condition is set here that defines the minimum thickness of ice allowed (one meter in this case). This prevents any unrealistic inputs or calculations by redefining any surface node position that was calculated to be lower than the glacier bed, to

[1] One experiment will introduce a third body that corresponds to a bottom free surface when cavities at the glacier bed are considered.

be one meter higher than the bed. Initial parameter values used in Glen's flow law, as well as other descriptions of ice, such as density, the Poisson ratio, and Young's modulus, are given in table 3.1. Values used in most simulations are based on studies done on other temperate glaciers (Cuffey and Paterson, 2010; Gagliardini et al., 2011) and units are in MPa - a - m (mega-Pascals - years - meters) to keep with the established custom in Elmer/Ice.

Parameter	Value	Units
Ice density	916.2	kg/m^3
Water density	1000	kg/m^3
A (pre-factor)	9.1254e+12	$MPa^{-3}a^{-1}$
Earth's acceleration from gravity	-9.81	m/s^2
Glen exponent	3	
Activation Energy	60	kJ/mol
Glen Enhancement Factor	1	
Critical Shear Rate	1.0e-10	$MPa \cdot a^{-1}$
Constant Temperature	-1	degrees Celsius
Young's Modulus	1.0	
Poisson Ratio	0.3	

TABLE 3.1: **Parameter values used initially in the Elmer/Ice simulation of Bering Glacier.**

3.5.4 Solvers and their numerics

3.5.4.1 Navier-Stokes

The most important solver in glaciological models is the Navier-Stokes solver used to describe the flow of ice driven by gravity. Because ice is a highly viscous material, advective and inertial forces can be neglected so that the mass and momentum conservation formulas of Navier-Stokes can be linearized and renamed the Stokes equations (see section 2.2.2). The convective accelerations can easily be turned off and on by the addition or neglection of the keyword "Stokes" in the SIF file (see Appendix A). This solver assumes that ice flow is isotropic and isothermal and these assumptions are held throughout the thesis. It is important to note that anisotropic flow laws and temperature solvers exist in Elmer/Ice but are not used in this model as these assumptions are often held in studies involving temperate ice (Cuffey and Paterson, 2010).

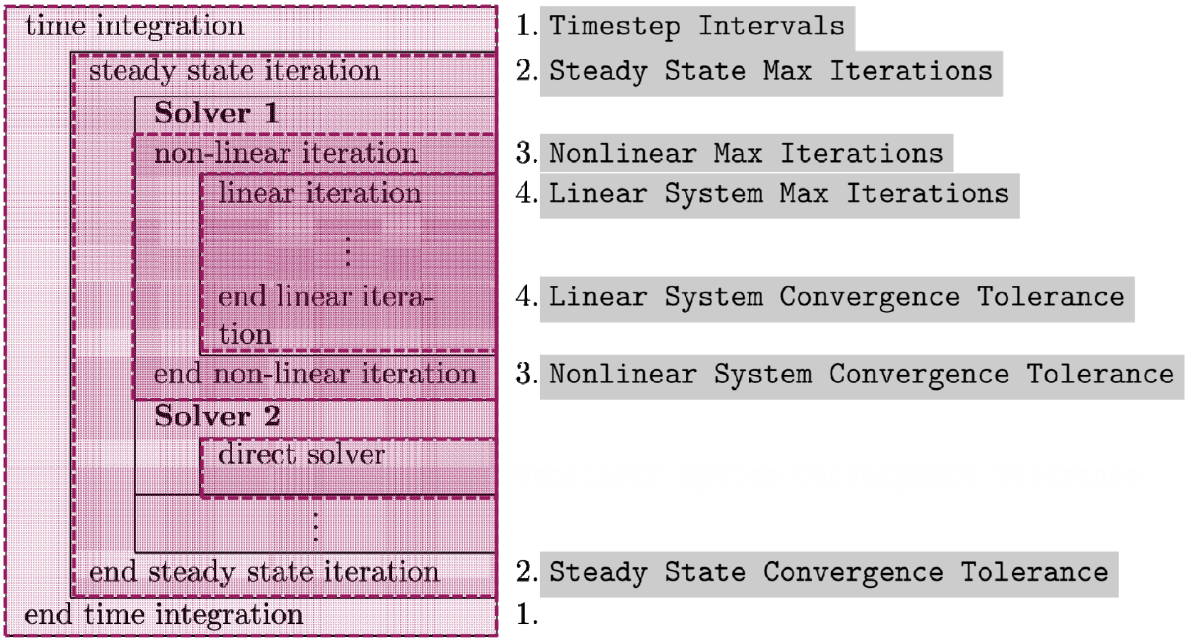

FIGURE 3.11: **Overview of the numerics and the different layers of iteration.** For a transient simulation, we iterate in time over a specified number of intervals, letting each solver calculate its specified output for each time step. If the simulation, for example, included the heat transfer problem with a coupling to the Stokes equations via velocity, a steady state solution would need to be found for each time step. In the case of this thesis, where the general advection-diffusion problem is not solved, we need not solve a steady state problem and therefore the Steady State Max Iterations is set to 1. When solving the Stokes equations (Solver 1 in the figure) a nonlinear system must be solved iteratively by solving the linearized problem described in section 2.3. This linear system may be solved using a variety of different direct or iterative methods.

The formulation of the linear system used to solve the Stokes equations is given in section 2.3. A direct method to solve the linear system is used that calls the external library UMFPACK (unsymmetric multifrontal sparse LU factorization package) to solve and uses stabilization methods to ensure numeric stability. Other methods for solving this system can be found in Appendix B in table B.2. Nonlinearities arise through the material parameters for the nonlinear system when $n > 1$ in Glen's flow law (equation 2.8 and 2.35). For each iteration in a nonlinear loop, we find the effective viscosity η using the previously calculated velocity field ($\boldsymbol{u}$) via a Picard iteration,

$$\boldsymbol{u} \cdot \nabla \boldsymbol{u} \approx \boldsymbol{u}^{(i-1)} \cdot \nabla \boldsymbol{u}^{(i-1)} \tag{3.1}$$

or a Newton iteration,

$$\boldsymbol{u} \cdot \nabla \boldsymbol{u} \approx \boldsymbol{u}^{(i)} \cdot \nabla \boldsymbol{u}^{(i-1)} + \boldsymbol{u}^{(i-1)} \cdot \nabla \boldsymbol{u}^{(i)} - \boldsymbol{u}^{(i-1)} \cdot \nabla \boldsymbol{u}^{(i-1)}. \tag{3.2}$$

With quadratic convergence, we will arrive at a solution faster using Newton linearization but on the downside, it is known to diverge if we start to far away from the solution (Gagliardini et al., 2013). Therefore we will always start with Picard iterations (five in this case), and then switch to Newton iterations to speed up convergence. The related tolerances and maximum iterations for each method is given in the SIF file in Appendix A.

3.5.4.2 Cauchy/Deviatoric stress

This module will solve for the deviatoric stress based on the calculation of the strain rate tensor (equation 2.8), which itself is found through the velocity field (equation 2.6). The strain rate itself can easily be made to be an output of the simulation by adding the *strain rate solver* whose implementation is similar to this one. If one prefers to have the full Cauchy stress tensor, as opposed to just its deviatoric part, the keyword Cauchy is set to be logically true (see Appendix A). The elements of the Cauchy stress (σ_{ij}) are found by subtracting the isotropic pressure p from the deviatoric part ($2\eta\dot{\epsilon}_{ij}$ see section 2.2.2), that is,

$$\sigma_{ij} = 2\eta\dot{\epsilon}_{ij} - p\delta_{ij} \tag{3.3}$$

where δ_{ij} is the Kronecker delta.

3.5.4.3 Eigenvalues of stress tensor

This solver allows us to compute the eigenvalues, and associated eigenvectors, of any previously calculated tensor variable. In this case, we are interested in the eigenvalues of the stress tensor because they are invariants that represent principle stresses. The associated eigenvectors represent the direction of the principle stresses. The eigenvalues are stored in a vector labeled *eigenstress* and are ordered so that the third component gives the maximal tensile strength.

3.5.4.4 Free surface solver

Like the Stokes solver, the upper free surface solver requires both linear and nonlinear iterations to solve equation 2.12. To show the different methods for solving the linear system, an iterative method was employed, specifically the Biconjugate Gradient Stabilized (BiCGStab) method. The specifications of this method are given in the example SIF file under Solver 4 in Appendix A. For stabilization, the residual free bubbles method is used (see section 2.3).

The nonlinear system can be treated the same way as described in the Stokes Solver section (3.5.4.1) and its specifications are given in the example SIF file. A choice to include accumulation (snowfall) in the simulation is specified in this section by setting the keyword "Use Accumulation" to be logically true. Accumulation is taken as a normal flux to the surface.

3.5.4.5 Mesh update

The mesh update solver is used to shift the nodes in our glacier surface in order to comply with the altered geometry imposed by the change in the free surface. The deformation reaction of the mesh is given by the Poisson ratio and Young's modulus specified in the materials section 3.5.3.

3.5.4.6 Paraview converter

This last module serves the purpose of converting the results of each time step into a format that can be read by Paraview for post-processing.

3.5.5 Equations

The Equations section of the SIF file specifies which solvers are to be active during the simulation run and specifies those that are connected by the same equation. In our case, all the solvers except the Free Surface Solver are connected to the Stokes Equations, leaving us with two separate equations specified in this section.

3.5.6 Boundary conditions

3.5.6.1 Bedrock

It is in this section that we define the basal sliding law we wish to use. Often, simulations are done with no sliding by setting the velocity at this boundary to be zero in each direction. Most experiments will fix our linear sliding law coefficient to be 0.1 in the tangential directions. The normal velocity is set to zero since there is no ice flux through this boundary. Because we assume the bedrock boundary is fixed, we set the mesh update in each direction to be zero so that our basal boundary does not change. Many variations to this condition are tested throughout experimentation.

3.5.6.2 Upper surface

For the upper free surface we must tell Elmer that this boundary belongs to Body # 2, by setting the keyword "Body ID" to 2. We do not wish to fix the velocity on the surface and therefore no velocity conditions are specified for the upper surface. In order to properly analyze elevation change, we want to fix the mesh points in the x and y-directions and only allow these nodes to move vertically in the z-direction. To do this we set the Mesh Update variable to be zero in the x and y-directions and only restrict the z-direction so that the upper surface does not go below the bedrock boundary. This last part is done by using a user defined function in the Materials section of the SIF. Once again, several variations on this condition will be tested, but this is the most common specification.

3.5.6.3 Lateral boundaries

For the sides of the glaciers, we initially set the velocity in each direction to be zero, that is, we assume no sliding on the boundaries. Because the lateral sides are so small compared to the other boundaries, this assumption does not effect our results in a significant way. We also will assume that the glacier sides are rigid and do not change, so the Mesh Update variable is set to zero in each direction.

3.5.6.4 Other boundaries

In some simulations, a subset of the lateral boundary points is divided into additional, separately defined boundaries of the glacier. For example, in simulations dealing with basal hydrology, the bottom layer of the lateral boundary is split into a lower basal frame (boundary 4 in figure 3.12) and the terminus (boundary 5 in figure 3.12). In most cases, boundaries 3, 4 and 5 in figure 3.12 are all part of the lateral boundary defined in 3.5.6.3.

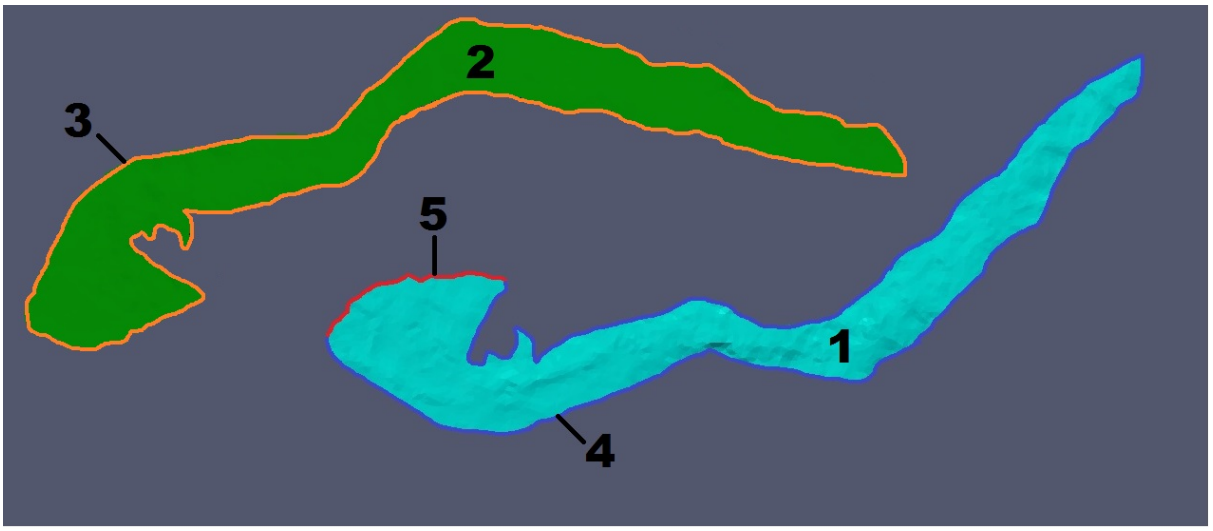

FIGURE 3.12: **Five distinct boundaries used in glacier simulations.** The top of the glacier is shown in green where the bottom of the glacier is shown in light blue. Boundary 1 - bed topography, Boundary 2 - upper free surface, Boundary 3 - lateral boundary (defined for the upper and middle layers), Boundary 4 - basal frame, Boundary 5 - glacier snout at the base. Boundaries 3, 4, and 5 are combined into a single boundary in most experiments that do not include basal hydrology.

3.5.7 Experiments with basal hydrology

Additional solvers are needed when considering basal hydrology. In the case of calculating the hydropotential, a solver that calculates the height of the glacier at each point is needed. In the case of the double continuum approach, recently created (2014) modules calculating IDS and EDS specific values are included. An overview of these solvers is not given here but can be found on the Elmer Ice Wiki page at http://www.elmerfem.org/elmerwiki/.

3.5.8 Variable visualization examples

Figures 3.13 and 3.14 provide 33 examples of the types of variable visualization that can be done in Paraview once Elmer, or more specifically the ElmerSolver, is done with calculation. Each of these variables are solved for using the solvers described above. Figure 3.13 (i) - (iii) gives the *normal vectors* for each element on the bottom surface. The color in the vectors represent the component of the normal vector in the (i) x, (ii) y and (iii) z-directions. Vector (or glyph) visualization is one of the many ways to view the results. Figure 3.13 (iv)-(vi) gives the *eigenstress* components, or rather in eigenvalues of the Cauchy stress tensor. They are ordered so that the first eigenvalue, (iv) *eigenstress* x, is the smallest eigenvalue, followed by (v) *eigenstress* y, with the largest eigenvalue being (vi) *eigenstress* z. These values, like most variables in this thesis, are represented through a color scheme and are labeled by a scale at the bottom. Figure 3.13 (vii)-(ix) gives the magnitude of the eigenvectors associated with aforementioned eigenvalues at the base of the glacier. Figure 3.13 (x)-(xii) gives the *normal stress* in the x-direction, returned from Elmer as *stress*1 i.e. $\boldsymbol{\sigma}_{xx}$, at time steps (x) 1, (xi) 100, and (xii) 1000 at the ice/bedrock boundary. Note that any of the field variables in figure 3.13 can be plotted at any of the time steps that were solved for using ElmerSolver. Figure 3.13 (xiii)-(xv) gives the *shear stress* in the y-z plane, $\boldsymbol{\tau}_{yz}$, at the base of the glacier after (xiii) 1 time step, (xiv) 100 time steps and (xv) 1000 time steps. Figure 3.14 (xvi)-(xviii) gives the fifth component of the *strain rate* tensor, that is the strain rate in the y-z plane, after (xvi) 1 time step, (xvii) 100 time steps and (xviii) 1000 time steps at the ice/bedrock interface. Any of the six independent entries of the stress and strain rate tensors can be visualized at any time step. Figure 3.14 (xix)-(xxi) gives the *velocity* on the surface of the glacier after (xix) 1 time step, (xx) 100 time steps and (xxi) 1000 time steps. Figure 3.14 (xxii)-(xxiv) gives the *mesh update* variable in the z-direction after (xxii) 1 time step, (xxiii) 100 time steps and (xxiv) 1000 time steps on the glacier surface. This variable is interpreted as cumulative elevation change. Figure 3.14 (xxv)-(xxvii) gives the magnitude of the *mesh velocity* after (xxv) 1 time step, (xxvi) 100 time steps and (xxvii) 1000 time steps at the top of the glacier. Figure 3.14 (xxviii)-(xxx) gives the scalar quantities (xxviii) *pressure*, (xxix) *Zs top* or elevation, and (xxx) the *height* of the glacier measured from base to surface. The last row in figure 3.14 gives the variables that one can solve for that are associated with hydrology. Specifically, (xxxi) gives the *hydropotential* at the base of the glacier, which is visualized using contour lines of equipotential giving a third

way to visualize our data. (xxxii) Gives the *eplhead* (equivalent porous layer water head) at the base and (xxxiii) gives the *idshead* (inefficient drainage system water head) at the base. It should be noted that although all the data that is visualized in figure 3.14 is shown for the base or the surface of the glacier, it is possible to visualize each of these variables at points in any of the internal layers of the glacier mesh. Cross-sectional view can also be easily made.

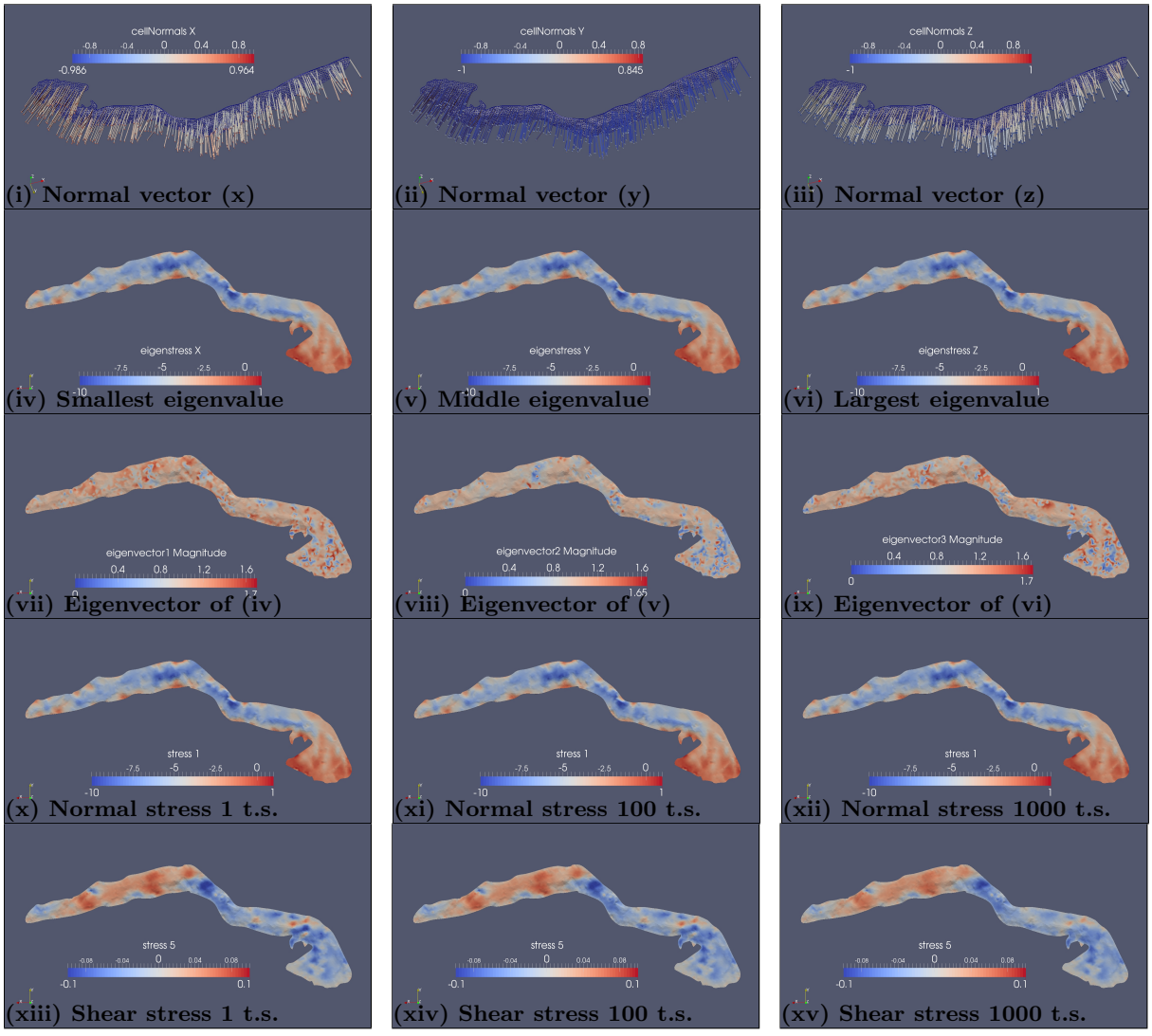

FIGURE 3.13: **Examples of possible variables that Elmer can solve for and their visualizations using Paraview (I).** (i)-(iii) Cell-normal vectors with x, y and z-components respectively. (iv)-(vi) Eigenstress or eigenvalues of the Cauchy stress tensor in ascending order. (vii)-(ix) Associated eigenvectors of the Cauchy stress tensor. (x)-(xii) Normal stress in the x-direction after 1, 100 and 1000 time steps. (xiii)-(xv) Shear stress in the y-z plane after 1, 100 and 1000 time steps.

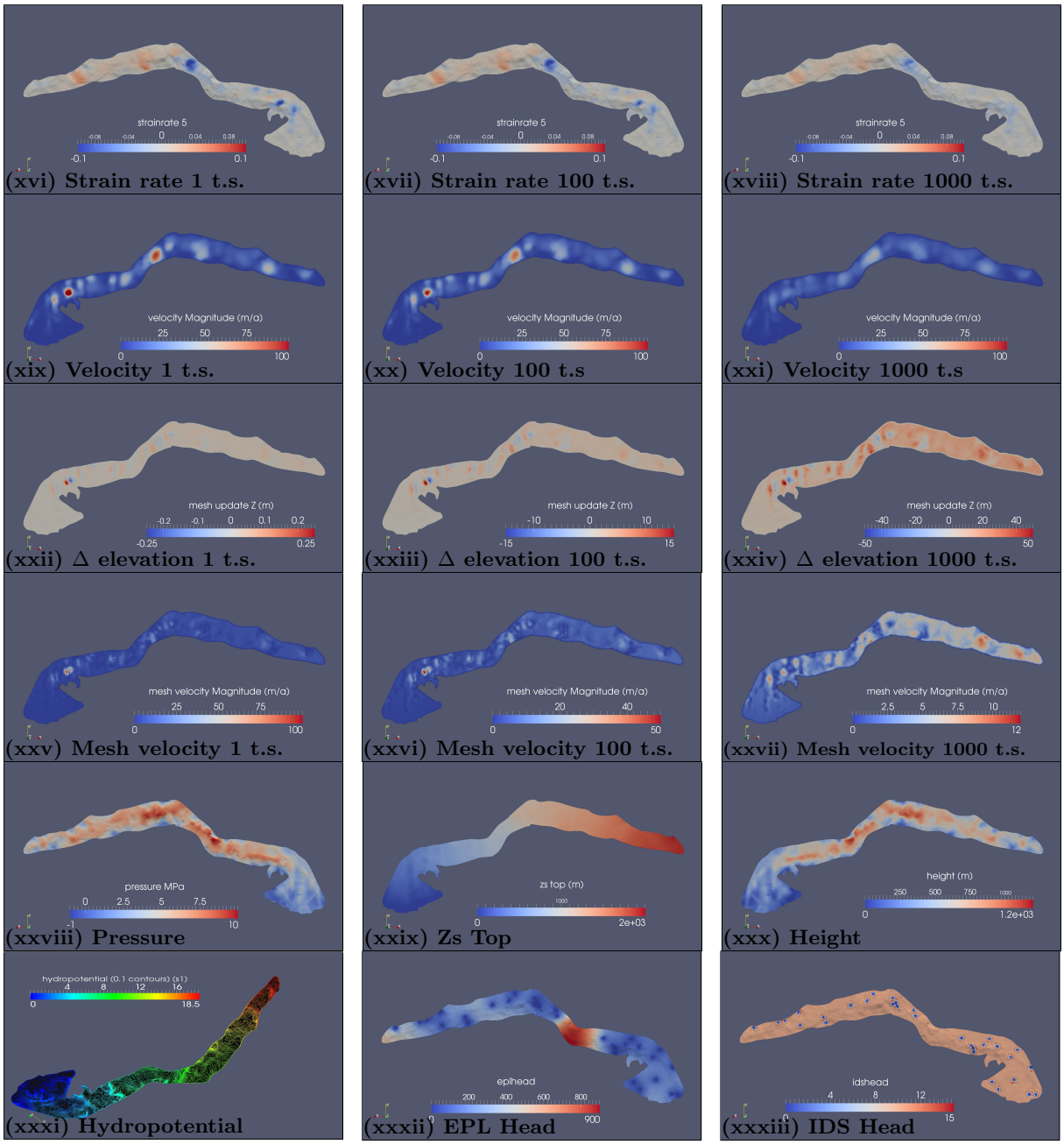

FIGURE 3.14: **Examples of possible variables that Elmer can solve for and their visualizations using Paraview (II).** (xvi)-(xviii) Strain rate in the y-z plane after 1, 100 and 1000 time steps. (xix)-(xxi) Velocity magnitude after 1, 100 and 1000 time steps. (xxii)-(xxiv) Mesh update in the z-direction, or cumulative elevation change, after 1, 100 and 1000 time steps. (xxv)-(xxvii) Mesh velocity magnitude after 1, 100 and 1000 time steps. The scalar quantities of (xxviii) pressure, (xxix) Zs Top or elevation, and (xxx) glacier height. Finally, the last row displays (xxxi) hydropotential, (xxxii) equivalent porous layer water head (eplhead) and (xxxiii) inefficient drainage system water head (ids head).

Chapter 4

Results and Analysis

4.1 Derived maps and time series analysis

4.1.1 Surface DEMs

Aside from being a useful input for modeling, the derived Digital Elevation Maps and their Difference Maps can help shed light on the current surge process via a time series analysis. Results derived from these maps, and hence the CryoSat-2 data, are presented on several levels, the first of which considers the usefulness of CryoSat-2 data in creating elevation maps for large mountain glaciers like Bering Glacier. The satellite is operated in synthetic aperture interferometric (SARIn) mode while over Bering Glacier. Figure 3.7 shows that six months worth of measurements provides sufficient coverage of the glacier surface to create a DEM of the surface. The area of Bering Glacier considered for the Digital Elevation Model is $\sim 865\ km^2$ and with an average of 625 data points per data set, a 200 m resolution DEM can be calculated with a maximum error of 21.75 meters and mean error of 3.67 meters based on the error analysis in section 4.2. DEMs for each of the four data sets are derived and are presented in figure 4.1.

A first result of the analysis is that CryoSat-2 data *can* be used for the study of elevation changes in Bering Glacier, Alaska. For six-month data sets, DEMs with error levels of 21.75 m maximally and noise levels of 45 m maximally can be derived. This allows to map elevation changes with a highest error level of $2 \times 21.75 = 43.5\ m$. Notably the largest error values occur

only in the first season and locally for later seasons so the error values are lower for most of the data (see section 4.2).

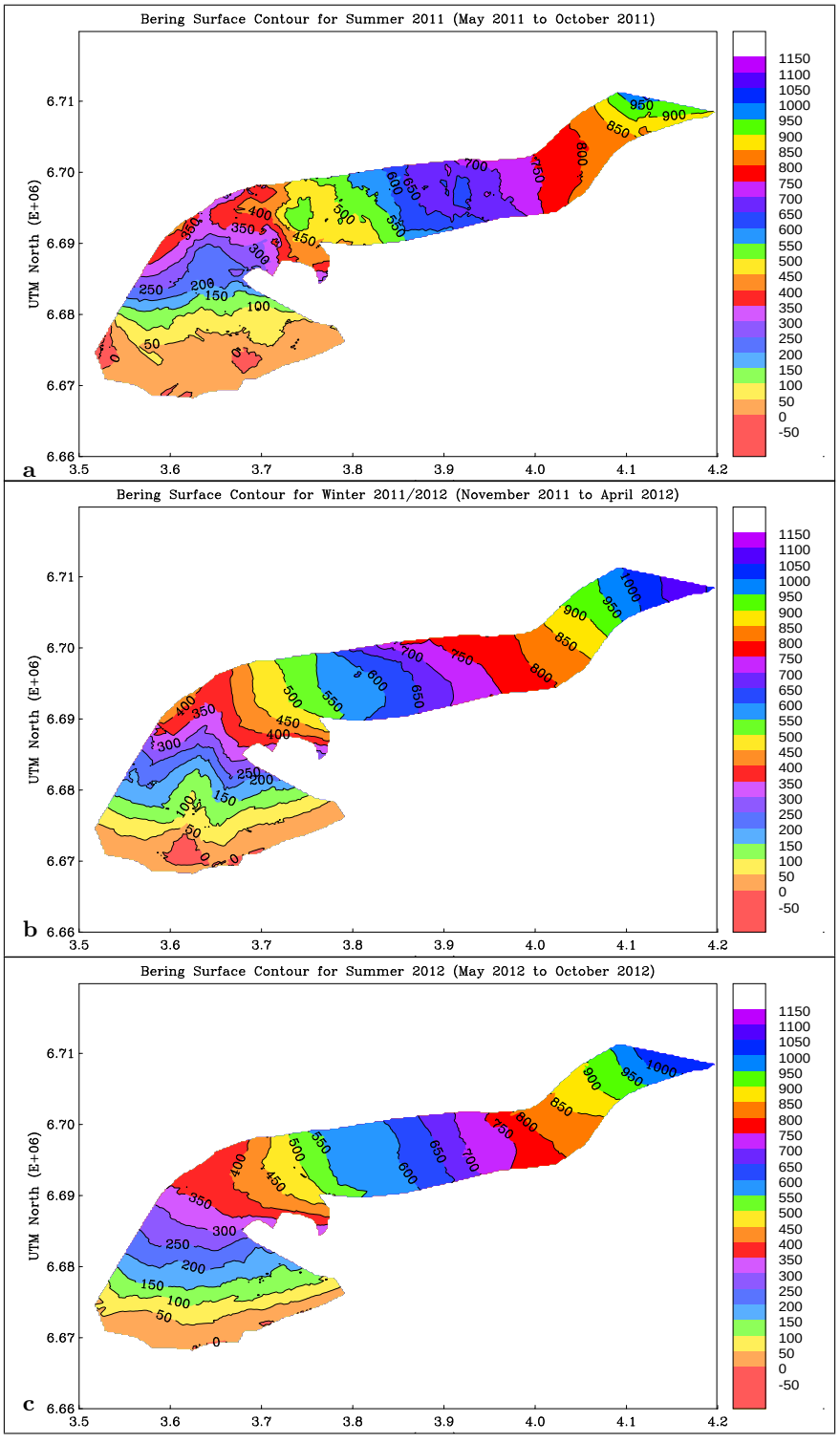

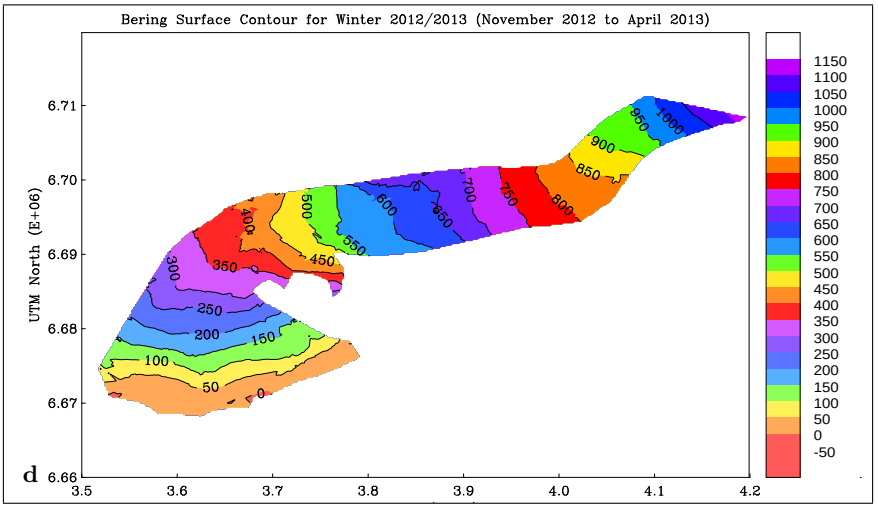

FIGURE 4.1: **Bering Glacier surface elevation from CryoSat-2 data.** Each color represents a 50 meter contour. (a) Summer 2011, (b) winter 2011/2012, (c) summer 2012, (d) winter 2012/2013.

The elevation maps constitute the second result of the analysis. These maps can be used as a basis for modeling or to study elevation changes. A visual comparison of the four maps already indicates that elevation changes over space and time. Airborne altimeter data, described in section 3.2, was used to measure surface elevation in September 2011 and 2012. The times that these measurements were made are near the boundary between the summer and winter seasons, and are therefore overlaid onto the two DEMs that are closest to them in time to see if any additional enlightenment can be found (see figure 4.2).

The tracks from fall 2011 in figure 4.2 (a) show good correlation with the summer 2011 DEM in the upper part of the glacier but not as much in the lower part. The opposite is true in figure 4.2 (b) that overlays the DEM from winter 2011/2012. This would suggest that mass transfer to the lower-glacier happened sometime before September 2011, but after CryoSat-2 measurements were made at that part of the glacier. It also suggests that elevation gain in the central-Bering during the winter happened after September 2011. The tracks from 2012 that overlay the DEM from summer 2012 match very well in figure 4.2 (c). This points to accuracy of the summer 2012 DEM to represent its time period since September is in its range. Figure 4.2 (d) shows a discrepancy in the upper part of the tracks perhaps suggesting that elevation changes occurred in the winter of 2012/2013 in that location.

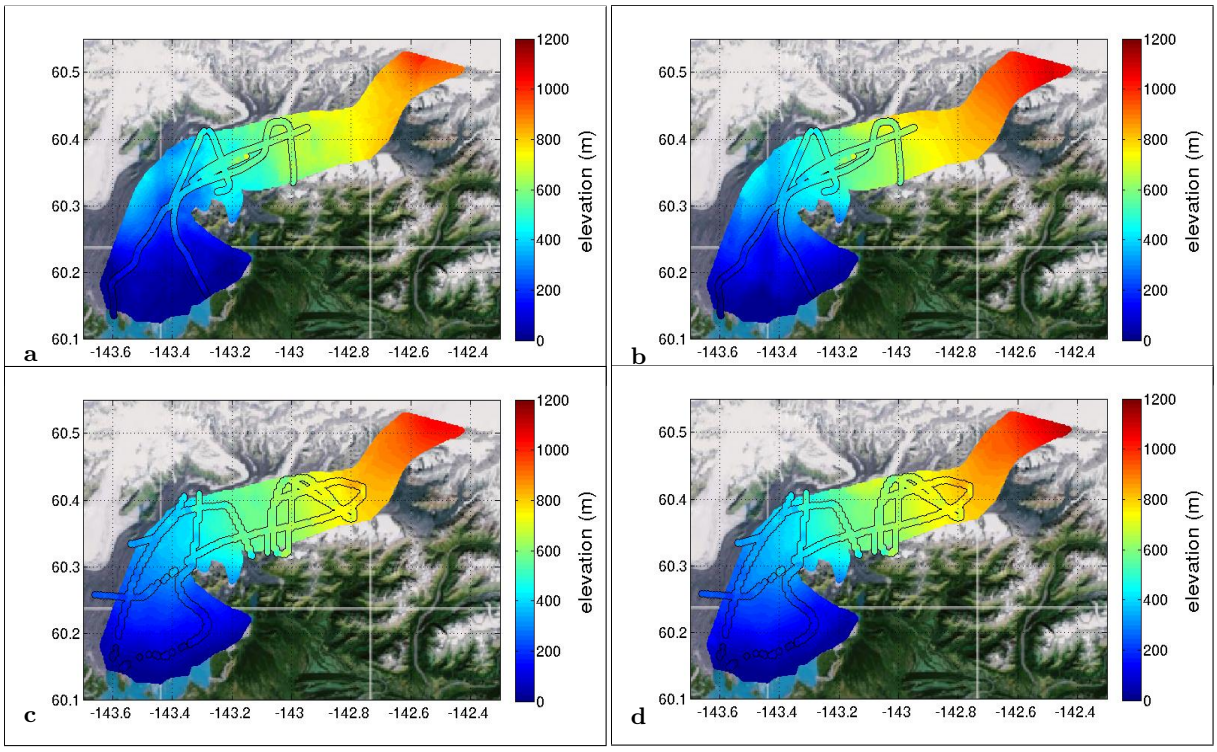

FIGURE 4.2: **Bering DEMs overlaid with airborne altimeter data from summer 2011 and 2012 campaigns.** (a) Altimeter data from September 2011 over DEM of summer 2011. (b) Altimeter data from September 2011 over DEM of winter 2011/2012. (c) Altimeter data from September 2012 over DEM of summer 2012. (d) Altimeter data from September 2012 over DEM from winter 2012/2013.

Elevation change is analyzed in detail in the next section, using difference DEMs. In summary, large-scale and large-sized changes in surface elevation can be derived from analysis of six-month DEMs based on CryoSat-2 data. Since elevation change during a surge is large, the maps derived here can be used for investigation of elevation changes during the surge.

4.1.2 Difference maps

From the four DEMs of the six-month seasons, six difference maps are derived (see figure 4.3). Elevation difference maps show values up to 150 meters in elevation gain and 100 meters in elevation loss, which are much larger than twice the maximum error of 21.75 meters and the average error level of 3.67 meters. Elevation change on the order of 150 meters is typical for a surge of Bering Glacier, as observed during the 1993-1995 surge by USGS lidar measurements (Herzfeld, 1998; Molnia and Post, 2010a).

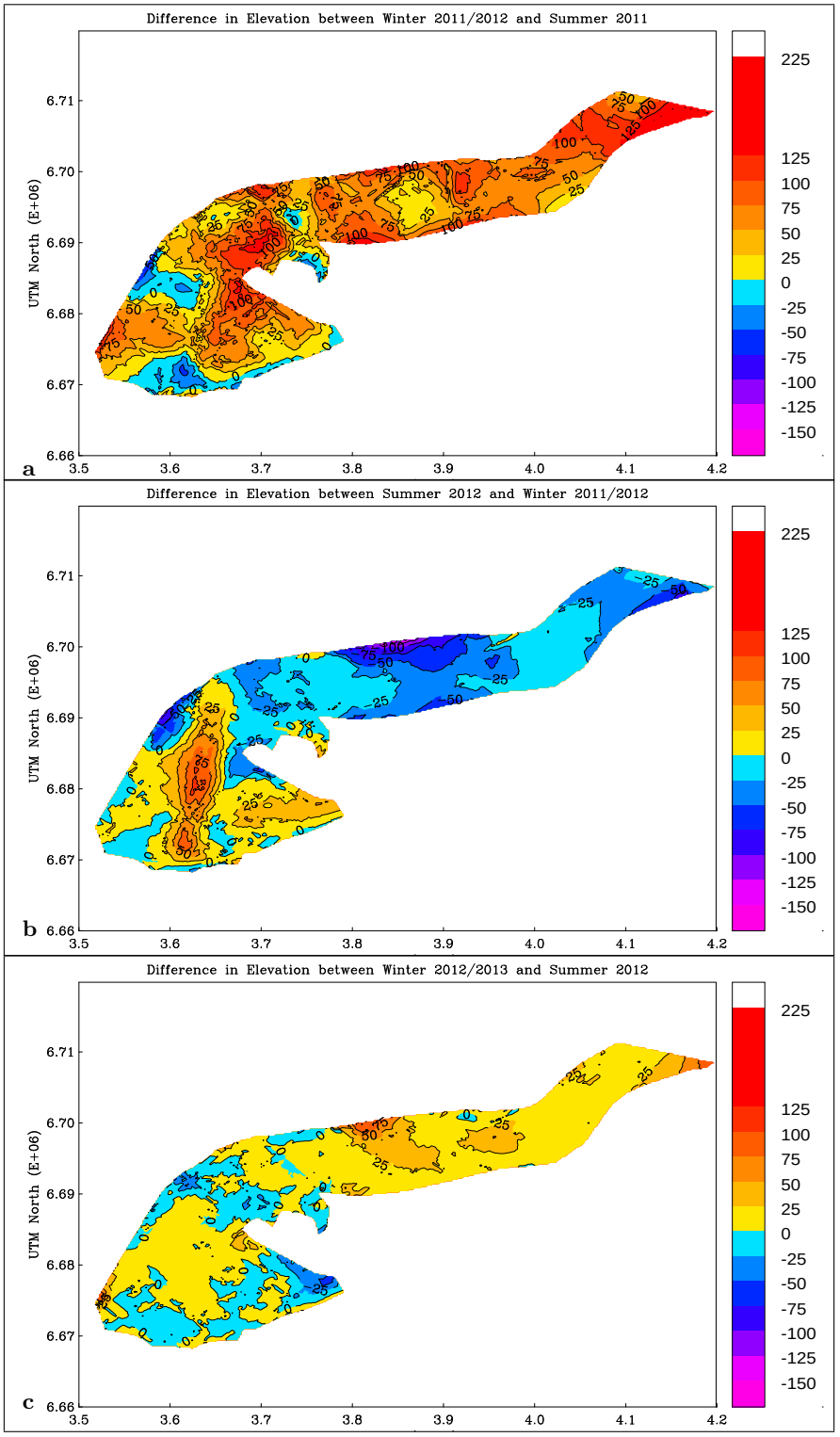
Difference in Elevation between Winter 2011/2012 and Summer 2011
Difference in Elevation between Summer 2012 and Winter 2011/2012
Difference in Elevation between Winter 2012/2013 and Summer 2012
UTM North (E+06)
6.66
6.67
6.68
6.69
6.70
6.71
3.5
3.6
3.7
3.8
3.9
4.0
4.1
4.2
225
125
100
75
50
25
0
-25
-50
-75
-100
-125
-150
a
b
c

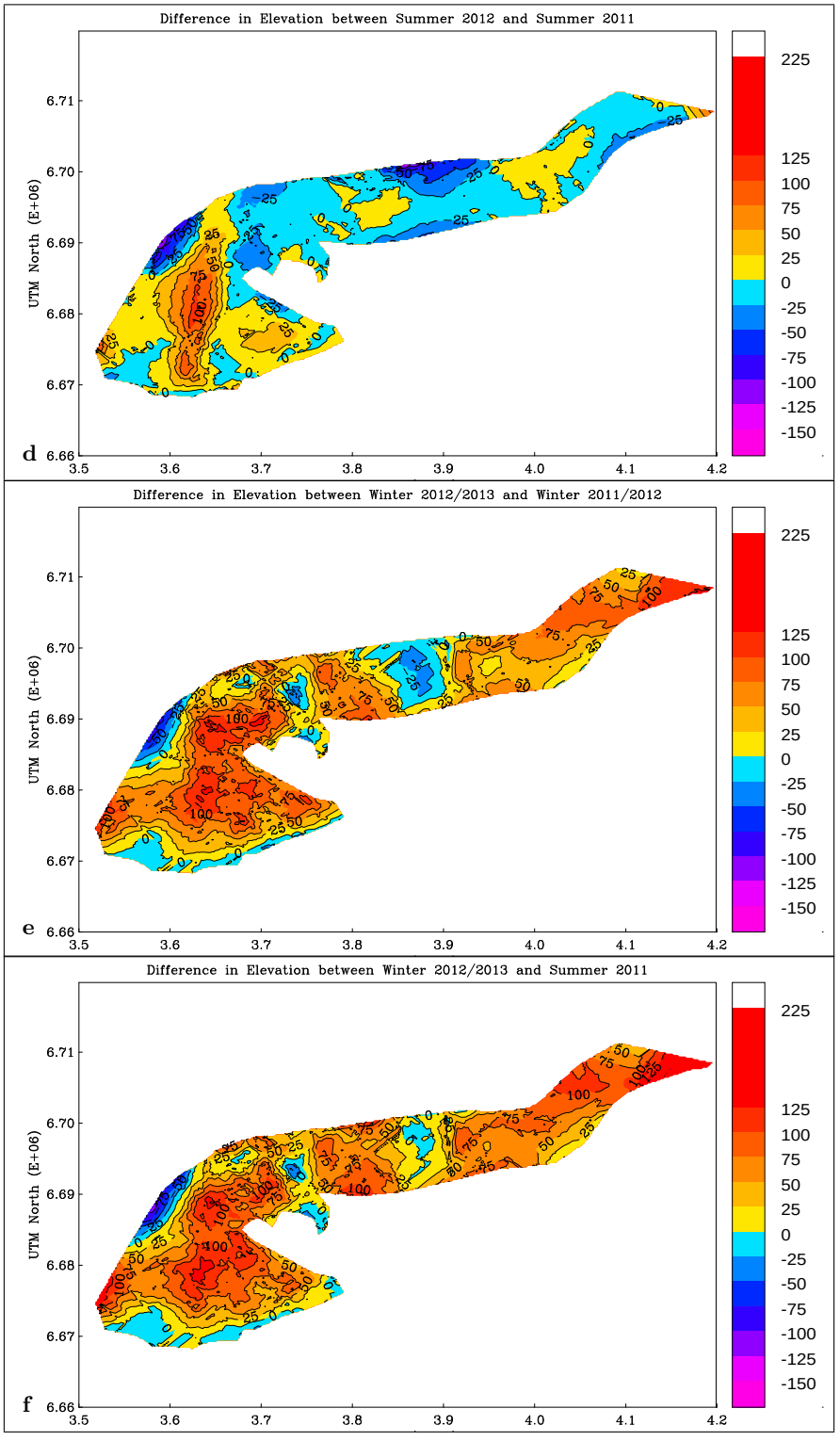

FIGURE 4.3: **Bering Glacier surface elevation change.** (a) Winter 2011/2012 elevation minus summer 2011 elevation, (b) summer 2012 elevation minus winter 2011/2012 elevation, (c) winter 2012/2013 elevation minus summer 2012 elevation, (d) summer 2012 elevation minus summer 2011 elevation, (e) winter 2012/2013 elevation minus winter 2011/2012 elevation, (f) winter 2012/2013 elevation minus summer 2011 elevation.

Measurement of surface elevation using radar and laser altimetry is effected by firn penetration and apparent range delay over snow surfaces. Yang et al. (2010) calculate apparent range delay for 532 nm laser altimeter data. Snow cover causes range delay corresponding to apparent surface lowering. However this effect accounts for an elevation error of 30 cm whereas surface roughness may cause a much larger apparent elevation error (on the order of 40 m for 532 nm laser altimeter data Herzfeld et al. (2012 in prep.)). Similar errors may affect CryoSat-2 data with other values.

Figure 4.4 provides a reference to keys areas on Bering that were effected during the surge.

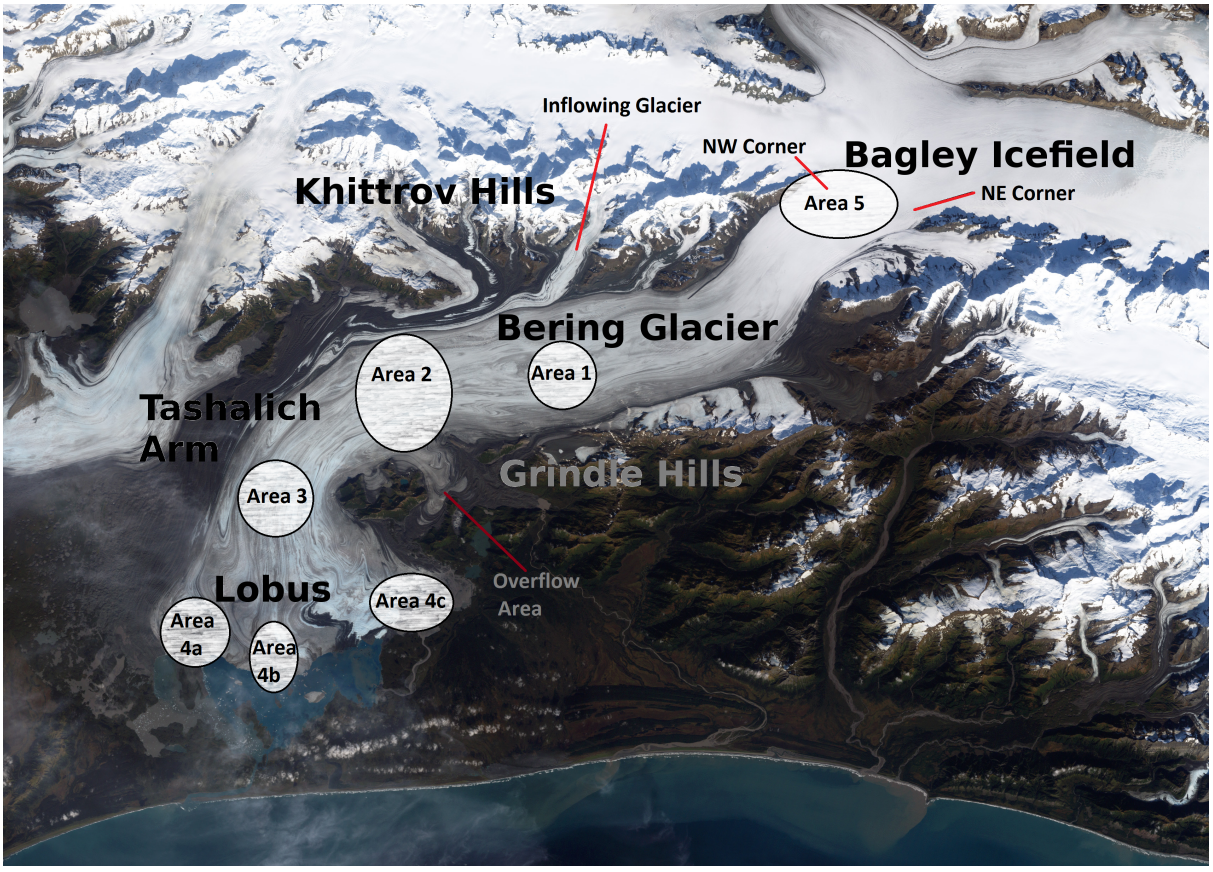

FIGURE 4.4: **Bering Glacier features.** Shown are labeled features of Bering Glacier and the surrounding area. Areas 1-5 are areas of interest during the surge and are referenced throughout the following analysis. Background image from nasa.gov.

Area 1: Central Bering. A small negative anomaly compared to surrounding areas is observed in area (1). Considering winter's snowfall and elevation gain observed elsewhere, ice surface lowering must have occurred in this area. Surface lowering in this area continues in summer 2012 (map (e), 25-50 m) and in winter 2012/2013 (map (f) 0-25 m). In this area, new crevassing

and apparent surface lowering were observed from aircraft in July 2012 and in October 2012, at the southern margin of Bering Glacier (figure 4.5 (a)) and at the northern margin (figure 4.5 (b)), while no *new* crevassing occurred in the longitudinally central region of area (1) despite being heavily crevassed. Area (1) is located south of an inflowing glacier form the North (see figure 4.4).

A small gain (0-25 m) occurred in summer 2012 to winter 2012/2013 in area (1) (see map (c)), so the change in map (f) results from change shown in map figure 4.3 (a) and map figure 4.3 (e), i.e. between summer 2011 and summer 2012. A large increase in surface elevation (>75 m) occurs in the northernmost part of area (1) from summer 2012 to winter 2012/2013, which is at the influx of a northern side glacier. A prominent rift formed in the northern part of the area (figure 4.5 (c)).

Area 2: Reservoir Area. Area 2, which includes the reservoir area, shows surface lowering (25-50 m) between summer 2011 and winter 2011/12 (map (a)). Coordinates for the reservoir area are 3.73-3.76 $\times 10^5$ UTM East, 6.692-6.695 $\times 10^6$ UTM North, as determined from laser altimeter measurements by (Herzfeld et al., 2013a). Surface lowering continues in this area as seen in maps figure 4.3 (b) (0-25 m), figure 4.3 (d) (> 25 m), figure 4.3 (e) (25-50 m) and figure 4.3 (f) (25-50 m). All maps, especially figures 4.3 (a), 4.3 (e) and 4.3 (b), show the mass transfer between the reservoir area and the Tashalich arm area (area 2 to area 3 and on to area 4). This transfer appears to weaken towards the end of the observation period.

Area 3: Upper Lobus. Area 3 receives prominent surface elevation gain (25-75 m) from winter to summer 2012 (map (b)). This, along with the rest of Tashalich arm, are the likely receiving zones. The mass transferred here continues to move down glacier into the lower lobus toward the glacier terminus as seen in map (e).

Area 4: Lower Lobus. Surface lowering is observed along the front of the entire lobus. From summer 2011 to summer 2012, the front in Tashalich Arm experienced the largest surface lowering (approximately 25 m), also area 4b (the front of another branch of Bering's several branches). Another area of anomalous behavior is 4c, the eastern margin of the lobus below the Grindle Hills is an ice fall, where acceleration occurs at time of surges (1993-1995, 2011-2013).

Area 5: Bering-Bagley Junction, the NW corner of the study area and a location below the junction of Bering Glacier and Bagley Icefield, shows a large increase (100-125 m) from summer 2011 to winter 2011/2012 (map (a)). This area is a region of heavy crevassing (figure 4.5 (d)). Note that highest values always occur in the NE corner, which are a result of extrapolation.

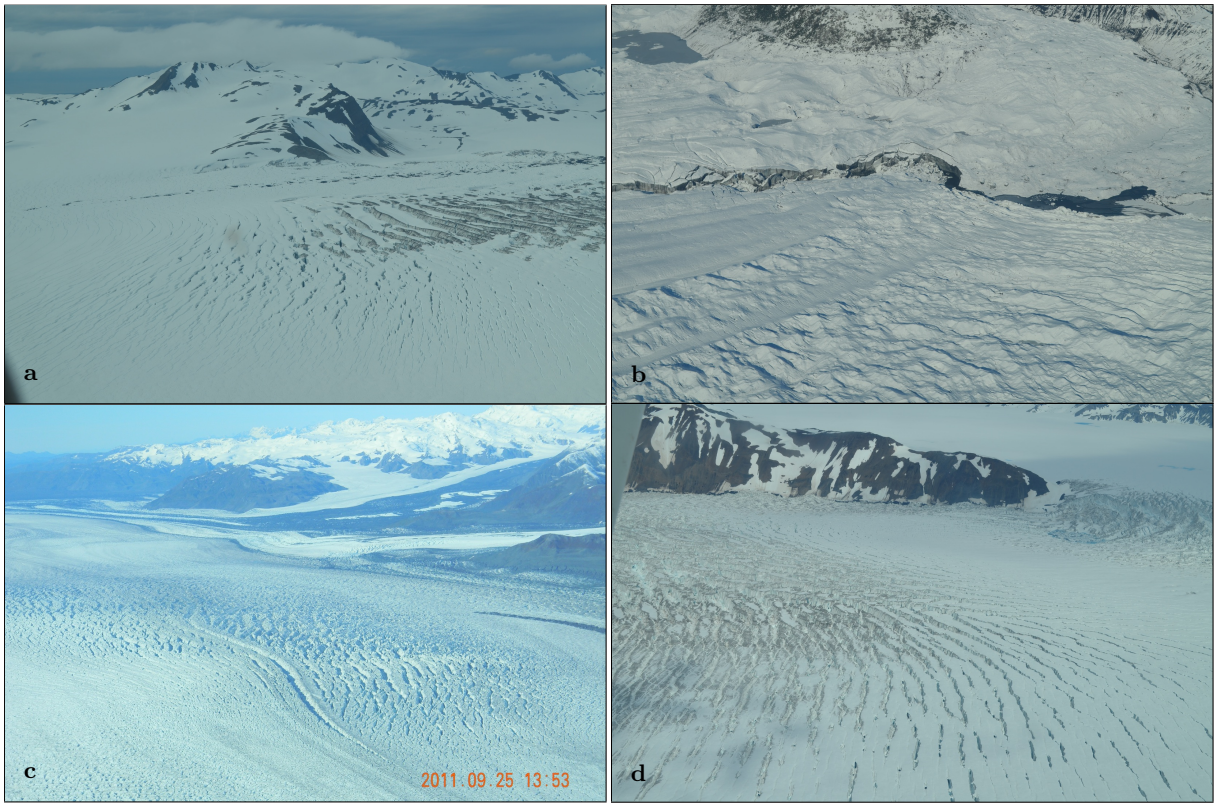

FIGURE 4.5: **Photos of the areas of interest from field campaigns in 2011 and 2012.** (a) and (b) New crevassing and surface lowering in the southern and northern part of Area 1 respectively. (c) A prominent rift in the northern part of Area 1. (d) Field of heavy crevassing near the Bering-Bagley junction in Area 5.

In summary: The difference map (a), summer 2011 to winter 2011/2012, shows mostly mass gain. Elevation increase from summer seasons to winter seasons needs to take into account snowfall, yet snowfall recorded in the surrounding area is on average 8.28 meters per year (Muskett et al., 2009; Osborn, 2013) and winter 2011/2012 was a record snow year in the Prince William Sound area. However spatially varying elevation changes of up to 125 meters interspersed with areas of elevation loss reaching over 50 meters cannot be explained by snowfall and hence must be attributed to the surge. In conclusion we can attribute connected areas of

surface lowering and surface heightening to geophysical processes related to the surge, taking into account that 0-25 meter elevation increase from summer to winter may actually reflect a lowering in ice surface elevation due to the error.

From winter 2011/2012 to summer 2012 (map figure 4.3(b)) we observe elevation loss everywhere except in the front. From summer 2012 to winter 2012/2013 (map (c)) there was not much change, except for a thickening near the inflow of the northern side glacier in area (1) (north of the rift area). Changes from summer 2011 to summer 2012 (map (d)) showed mostly elevation loss except in the lobus area. Changes from winter 2011/2012 to winter 2012/2013 (map (e)) show a mass transfer pattern that best matches the surge (compared to all other elevation change maps), with elevation loss in area (1) (the general rift area and region where surface lowering was observed in the field in 2012), in area (2) (the reservoir area), area (3) (NW side of central Tashalich arm, near the moraine) and along the front of the lobus (area (4)) and elevation gain of 100 m in an area below the junction with Bagley ice field (area 5), up to 100 m elevation gain in central Bering Glacier between areas (1) and (2), with the maximum on the southern side of the glacier, as well as a large region of elevation gain in lower central Bering Glacier and throughout the lobus, exceeding 125 m in the central lobus. Comparing map (e) to map (a) shows that some of this change initiated in 2011, while larger elevation losses in area (1) occurred in 2012. The mass transfer downward to Tashalich arm continues to 2012/2013. All these observations from CryoSat-2 data match field observations. Comparison of summer 2011 and 2012 suggests a prominent area of thickening along what may be a central trough branch underlying the lobus area. For this last observation, we do not have a matching field observation.

In conclusion, large (over 25 m) elevation changes, which are anomalous to the general elevation change trend between the six-month seasons, can be detected using CryoSat-2 data. These changes match field observations of surface lowering and fresh crevassing indicative of the surge process.

Hence if large elevation changes are occurring in large mountain glaciers, CryoSat-2 data can be used to map and analyze those. Relatively high error levels in CryoSat-2 data may otherwise preclude analysis of elevation change in mountain glaciers, or may require longer time series to aggregate data for better coverage and to average out errors.

4.1.3 Bed DEM

The resulting Digital Elevation Map from kriging the combined bed data and the derived variogram parameters is given in figure 4.6. A separate map of Bering (a) and Bagley (b) are given with their respective scales in order to show optimal contrast in elevation for each map. No error analysis was done for the bedrock DEM since the data was not attained until fall 2013.

A two dimensional plot along the central flow line of the Bering Glacier for the four surface maps and the bed map is shown in figure 4.7 for an alternative view.

4.2 Error analysis

Two methods are applied to derive error maps for DEMs: (1) the standard deviation of the kriging method (see equation 4.1) and (2) error maps using a formula resultant from numerical error propagation through the kriging equations. Method (1) is the standard method found in the kriging literature (Journel and Huijbregts, 1989; Matheron, 1963), method (2) is derived in Herzfeld (1992).

4.2.1 Standard deviation

The estimation variance of ordinary kriging (OK) is given by

$$s^2 = \sum_{i=1}^{n} \alpha_i \, \gamma^*(x_i, x_0) + \lambda \tag{4.1}$$

where λ is a Lagrange multiplier used in solving the kriging system. An advantage of the formula is that the estimation variance and estimation standard deviation $s = \sqrt{s^2}$ can be calculated without significant additional computational effort, because the coefficients α_i are derived by inverting the ordinary kriging system. The estimation variance depends only on the data distribution in space. Consequently the kriging variance simply reflects the survey pattern (it is a combination of the distance to the nearest track, the variogram values and the weights). The kriging variance is not an error measure in the sense of numerical error analysis. For an error analysis applied to kriging, see section 4.2.2.

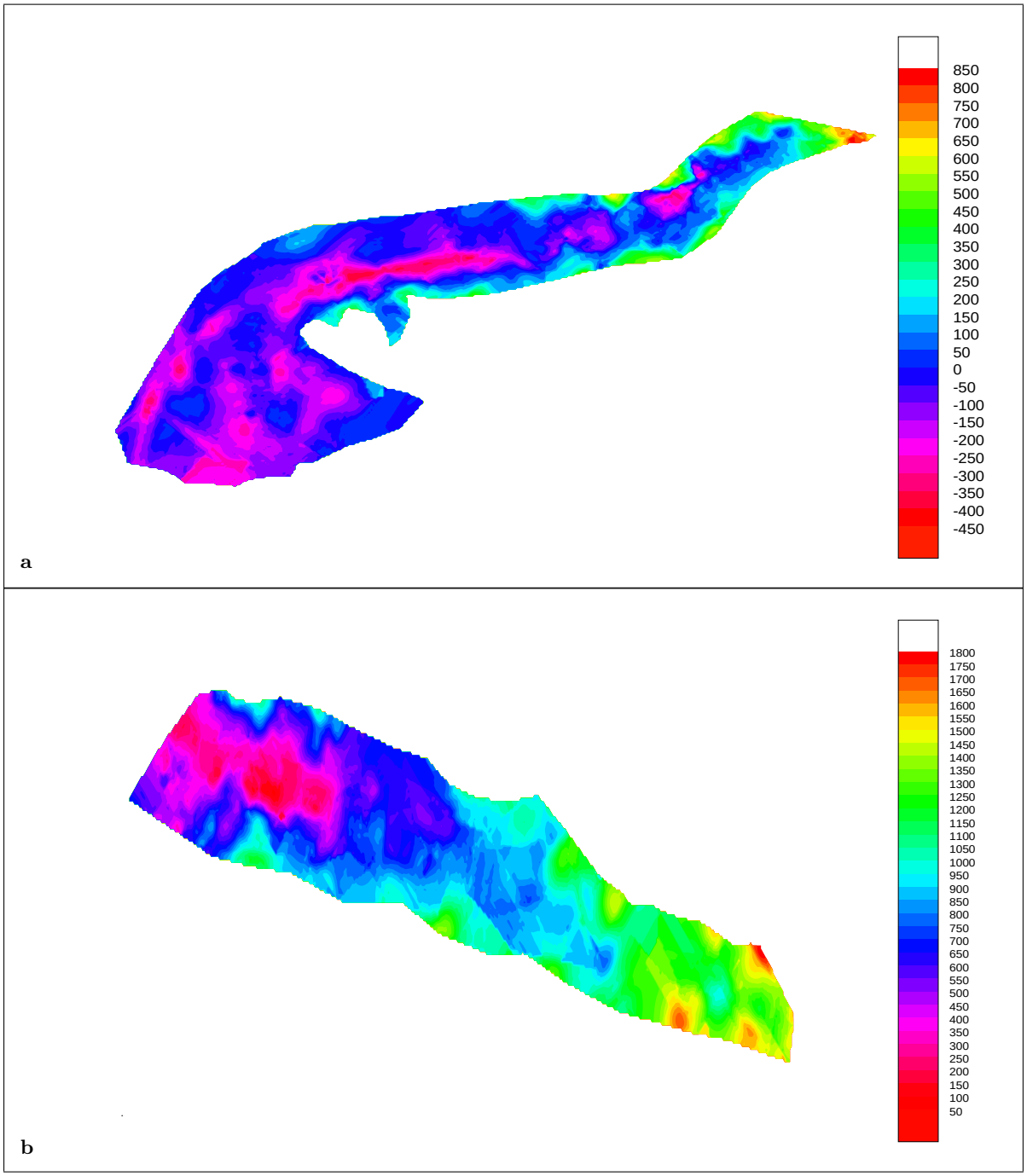

FIGURE 4.6: **(a) Bering Glacier and (b) Bagley Icefield bedrock DEMs.**

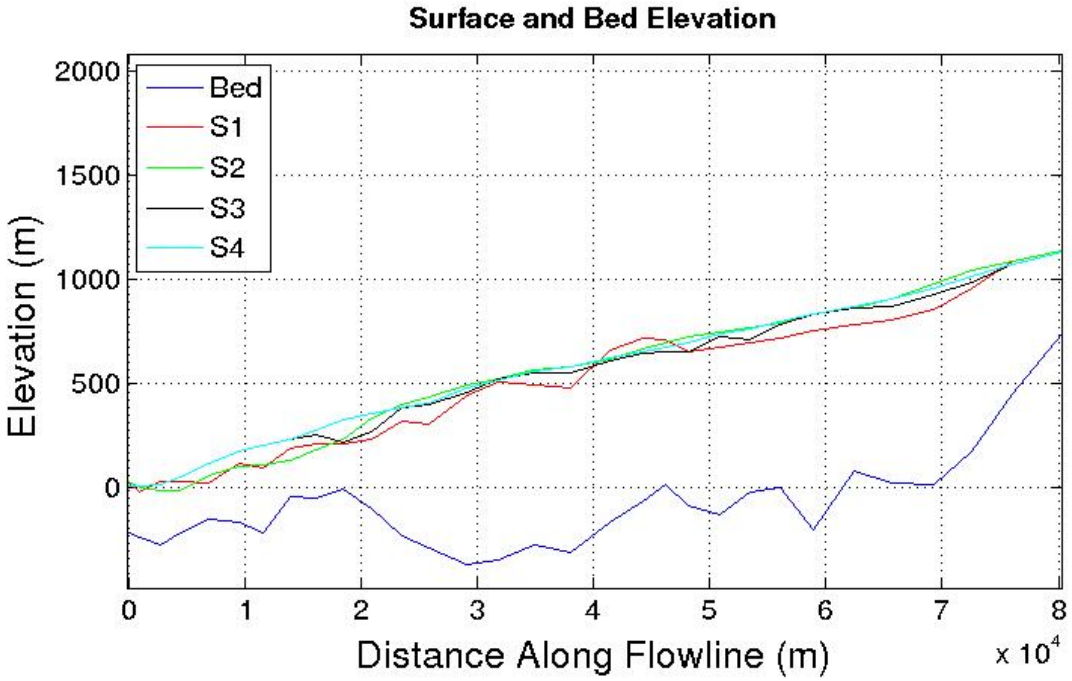

FIGURE 4.7: **Elevation along the central flow line of Bering Glacier.**

The northeastern corners of the summer 2011 and winter 2011/2012 standard deviation maps yield very high values. This is due to the lack of data points in the vicinity of the corner as can be seen in figure 3.8. We also have noticeably higher values in Tashalich Arm for reasons explained in the next section. The average standard deviation for each data set is 12-13 m.

4.2.2 Error propagation

The second method applies numerical random error propagation to the kriging equations (Herzfeld et al., 1993).

Theorem: Propagation of standard error through a function. If U is a quantity derived as a function $U(x_1, ..., x_n)$ of measured quantities $x_1, ..., x_n$ for a natural number n, then the standard deviation σ_U can be expressed in terms of the standard deviations σ_i of x_i for $i = 1, ..., n$ as follows:

$$\sigma_U = \sum_{i=1}^{n} \left(\frac{\partial U}{\partial x_i} \right)^2 {\sigma_i}^2. \tag{4.2}$$

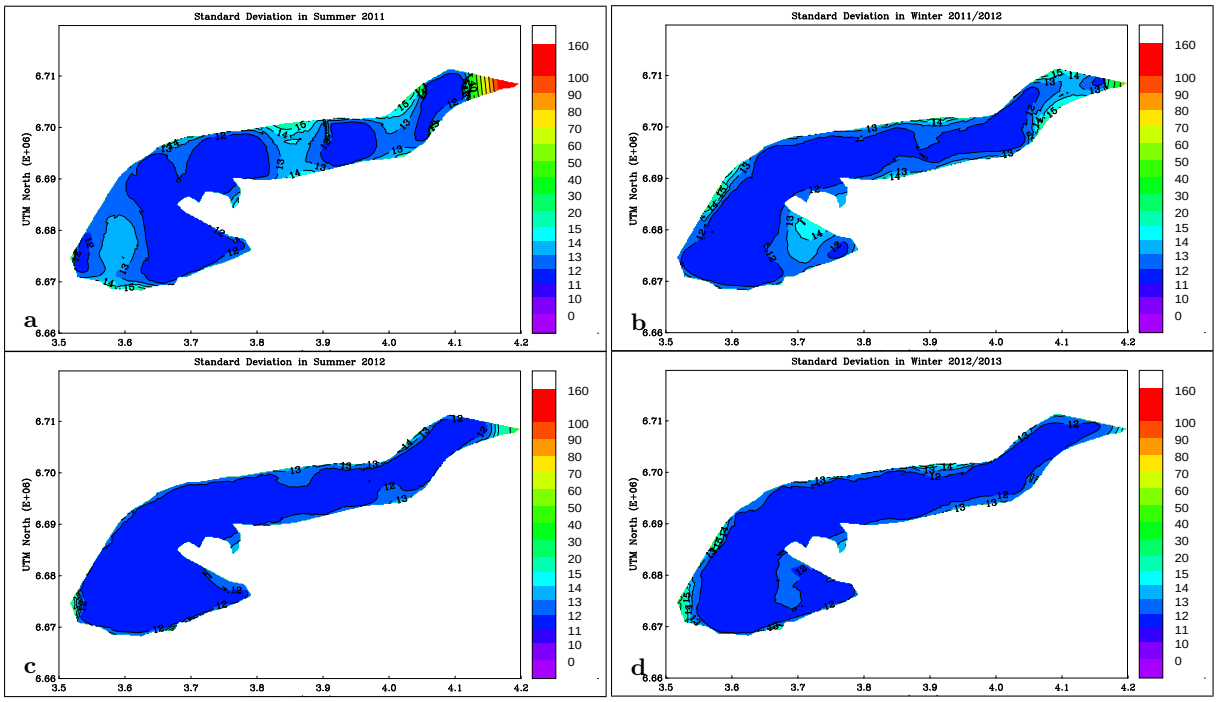

FIGURE 4.8: **Standard deviation of kriging for each of the four six-month periods.** Note that the color scale gives one meter steps from 10-15 m, a 5 m step from 15-20 m, and 10 m steps everywhere else in order to highlight variability. (a) Summer 2011, (b) winter 2011/2012, (c) summer 2012, (d) winter 2012/2013.

The theorem is quoted after Moffitt and Bouchard (1975), eqn. 4-16, p. 168.

It should be noted that an analytical approach to error approximation, based on absolute errors, would yield a different result. The form of the error equation is the same (based on derivatives) in the analytical case.

The theorem is applied to the kriging equation 2.57, noting unbiasedness conditions 2.56 for ordinary kriging.

(Step 1) Calculation of nugget values (nug).

As a first step in creating error maps, nugget values are derived for variograms calculated in along-track bins of CryoSat-2 data. The value in the first bin of the variogram is taken as the nugget value (see figure 4.9 and table 4.1). The average nugget value when considering all data points is 28.5502 m^2.

(Step 2) Calculation of noise levels (σ_0).

Noise levels are derived from nugget values for along-tack bins. The nugget value is the value of the (semi)variogram at zero distance (or, the value of the smallest distance bin). Since the (semi)variogram corresponds to half the variance for a certain distance class, the nugget is half the variance of observation in the same location, and hence the noise level, σ_0, is

$$\sigma_0 = \sqrt{2 \cdot nug}. \tag{4.3}$$

The average noise value when considering all data points is 12.0962 m (see table 4.1).

(Step 3) Calculation of numerical error (s_0).

From the gridded noise levels, an estimate of the kriging standard deviation is derived by propagating the noise levels through the kriging calculations, using methods applicable to random error propagation, that is, simply by application of the Theorem (with equation 4.2).

Application of the error propagation method to the kriging estimator equation 2.52 (with $\alpha_0 = 0$)

$$Z_0^* = \sum_{i=1}^{n} \alpha_i \, Z(x_i) \quad \text{with} \quad \alpha_i \in \mathcal{R}, \tag{4.4}$$

gives

$${s_0}^2 = {\sigma_0}^2 \sum_{i=1}^{n} {\alpha_i}^2 \tag{4.5}$$

where s_0 is the error estimate associated with elevation $z(x_0)$ in location x_0, Z_0^* denotes the kriging estimator, σ_0 the average noise level in the neighborhood of x_0 (as determined in step 2), and $\alpha_i, i = 1, ..., n$ are the kriging weights (from ordinary kriging), because

$$\frac{\partial Z_0^*}{\partial Z_i} = \alpha_i. \tag{4.6}$$

For simplicity, the deviation of the numerical error assumes that the standard deviation of measurement is the same throughout the neighborhood used for estimation of a point. We use σ_0 as derived in step 2. Results are shown in the right column in figure 4.9. The average error value when considering all data points is 3.6674 m (see table 4.1).

	Error Analysis Values		
Season	Error(m)	Noise(m)	Nugget(m^2)
Summer 2011			
Max	16.0792	38.3147	734.0076
Min	1.4692	4.9019	12.0143
Mean	7.1392	23.7749	289.1878
Winter 2011/2012			
Max	9.0619	16.0761	999
Min	0.1122	0.3771	20.9785
Mean	3.4084	10.8710	20.9785
Summer 2012			
Max	4.3620	6.9999	24.4991
Min	0.0378	0.1398	0.0098
Mean	1.6068	5.5738	16.5265
Winter 2012/2013			
Max	21.7536	44.6990	999
Min	0.0378	7.3831	27.2552
Mean	3.2890	10.6150	60.8085
All Data			
Max	21.7536	44.6990	999
Min	0.0378	0.1398	0.0098
Mean	3.6674	12.0962	28.5502

TABLE 4.1: **Error Analysis Values**

4.2.3 Interpretation of results from error analysis

A large noise level within a six-month data set may have two sources: (a) high noise in the CryoSat-2 data (remote sensing data collection noise) or (b) high variability in the surface elevation during the six-month time interval, due to mass transfer as part of the surge (geophysical causes). Noise levels of type (a) may be caused by increased crevassing that may lead to changes in apparent surface elevation (range delay, see (Herzfeld et al., 2012 in prep.)), changes in snow cover that may lead to forward scattering or range delay causing elevation errors, which are typically smaller than those related to surface roughness (Yang et al., 2010). An example for noise levels due to mass transfer is seen in Tashalich arm.

Highest error values (s_0) occur for the summer 2011 data, when high noise levels occur throughout the glacier. Hence this is likely an attribute of the CryoSat-2 data collected in this time frame. In winter 2012/13 high error values are observed in the Tashalich Arm area. Since Tashalich Arm behaves differently than other parts of Bering Glacier with respect to elevation change and crevassing during the surge, the high noise levels may be surge-related. Transfer of mass during the surge will lead to higher variability in the data, but is actually a geophysical signal and not a noise component. The noise value is up to 45 m, and our elevation increase of 20-40 meters was observed in airborne altimeter data over Tashalich arm (but in 2011). Thinning may have occurred in winter 2012/2013 in this region. The error levels for summer 2011 are high, depending on location. Therefore this may be a surge effect.

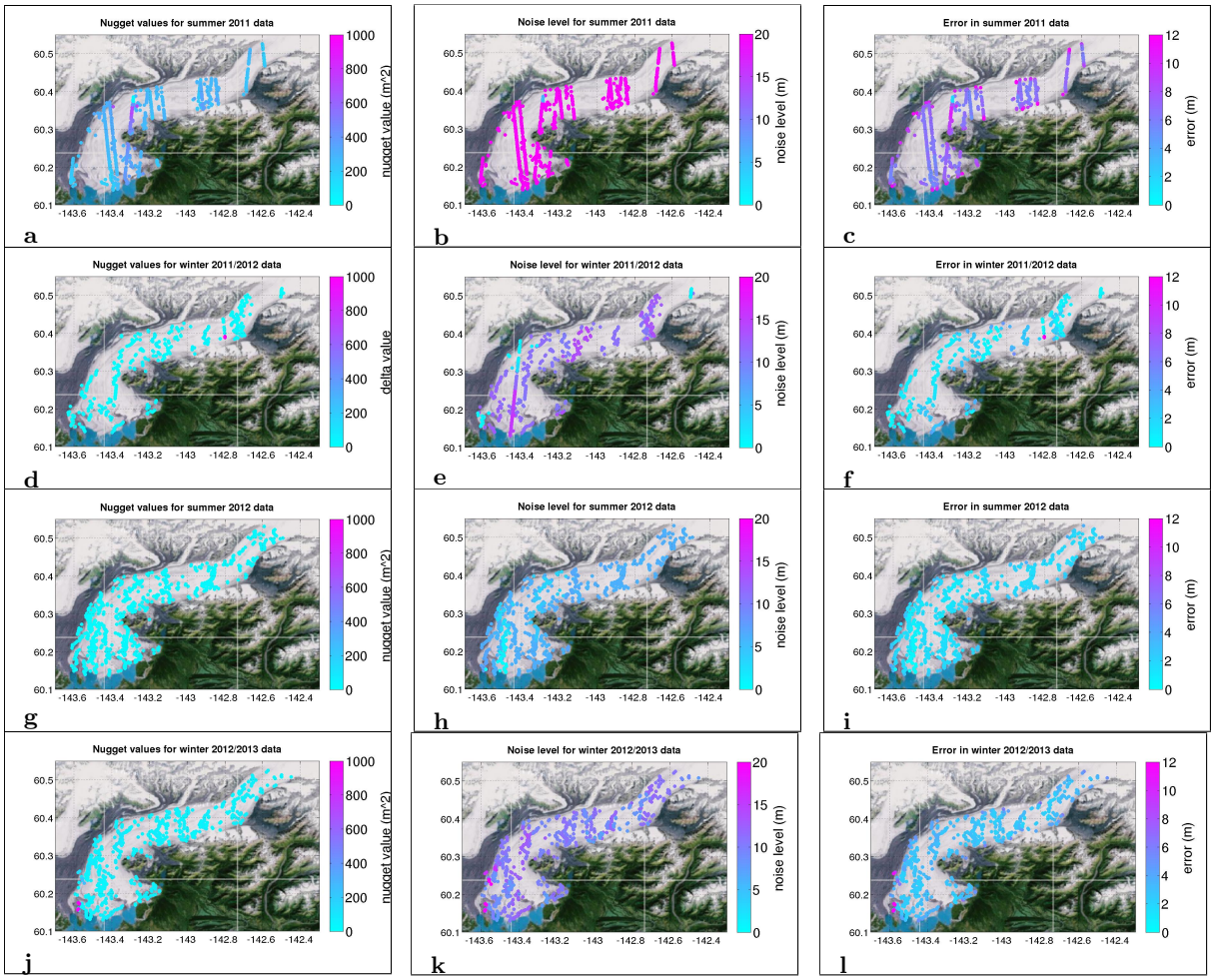

FIGURE 4.9: **Nugget values, noise levels and error values.** (a)(b)(c) Summer 2011, (d)(e)(f) winter 2011/2012, (g)(h)(i) summer 2012, and (j)(k)(l) winter 2012/2013. Nugget values are in the left column (a)(d)(g)(j), noise values in the middle column (b)(e)(h)(k) and errors in the right column (c)(f)(i)(l). Color scale is chosen to show variability in nugget, noise and error values. Values in very few points exceed the maximum of the color scales and are given in table 4.1.

Because this is the first ever application of CryoSat-2 data to glaciology, a future objective is a feasibility study to answer the question whether CryoSat-2 observation delivered the spatial coverage and accuracy needed to determine elevation change in large mountain glacier, like the Bering Glacier. Results are presented on several levels, (1) feasibility study of the use of CryoSat-2 data for analysis of elevation change in large mountain glaciers, (2) derivation of a time series of DEMs that can be used for numerical modeling and for elevation change mapping, (3) derivation of elevation change DEMs, and (4) analysis of elevation change and interpretation related to the surge process in Bering Glacier 2011-2013.

On the one hand, analysis of the surge evolution presents a challenge to CryoSat-2 altimeter data analysis, because mass transfers and hence elevation changes during the surge occur rapidly, so dense time series would be desirable. However, we determine that data from at least six months of observation are needed to yield sufficient coverage to derive DEMs.

4.3 Numerical experiments

After creation of surface and bedrock topographies and with an overall picture of the major surge event in the current surge, a numerical model can now be built and tested. Nearly 100 experiments were conducted over the course of this study and a summary of the interesting results are presented here. Many of these experiments are done in order to come to grips with how the model works and reacts to certain inputs. A lot of experimentation consisted of changing a single parameter, or omitting another, etc., to see how the model reacts. Once a comfortable feel of how the model works and reacts to inputs is gained, a realistic glacier model can start to be created. Parameter values describing the ice and its reaction to applied forces are kept constant through most of the experiments, except for those that aim to analyze the effects of changing these parameters, and are summarized in section 3.5.3 and table 3.1.

4.3.1 Early simulations: Experiments 1-30

Many of the early simulations consist of a very simplified picture of the BBGS and over time, complexity is added and a more refined and accurate picture of the system is eventually attained. For example, many of the early experiments only include the Bering Glacier and not the Bagley

Icefield due to a lack of bed topography data in that area. As time went on, more and better data describing glacier geometry, i.e. bed and surface topography, was attained and the model was updated accordingly. Interesting and insightful realizations can still be made from these early experiments despite their sometimes unrealistic simplicity and those results are given here.

4.3.1.1 Experiment 1: A first successful implementation

Experiment 1 represents a first, very crude, representation of Bering Glacier with parameter values describing the ice and its flow given in table 3.1. This experiment is run for a single time step and only considers Bering Glacier (not the Bagley Icefield). We start with a mesh that has elements in the plane averaging 2000 meters in length and is comprised of 20 vertically extruded levels. The Navier-Stokes solver and the paraview output converter were used (see section 3.5.4) and so only the velocity, pressure, and Cauchy stress fields are solved for. The glacier outline is a different one than used in later simulations and includes many jagged edges that were originally included to represent the mountainous boundary but was quickly dropped as it was determined that these small snowpacks and overflow areas did not contribute to the overall behavior of the glacier flow. Sharp edges on the boundary also create a more complex body and can lead to some numerical behavior that is unrealistic. For example, a jagged boundary can lead to "hotspots" of high velocity near the edges. Figure 4.10 shows the velocity in magnitude after the single time step and these "hotspots" can be seen in the upper parts of the glacier. Although the scale in figure 4.10 goes only to 1000 m/a^{-1} in order to show contrast in velocities throughout the glacier, the "hotspots" actually give velocities of up to 2250 m/a^{-1}. Moreover high velocities in tiny pockets like these are not characteristic of glacier flow and have not been observed on the BBGS.

4.3.1.2 Experiments 2-8: Addition of solvers and refinement of the contour outline

After a first successful, albeit very crude, simulation of Bering Glacier, the next steps were to add more solvers to calculate additional interesting fields and smooth out the contour outline. Experiment 2 added the calculation of the eigenvalues and associated eigenvectors of the stress tensor so that the principle stresses and their directions could be identified. The principal stresses and their directions play an important role in calculating the strength of ice and its

tendency to deform in a ductile or brittle way by matching these principle stresses to observed crevasses (Vaughan, 1993). Although an analysis using modeled principal stresses and observed crevasses patterns on the BBGS could be done, it was not in the scope of this thesis. Experiment 2 also displays an intermediate contour refinement unique to this experiment. Figure 4.11 (a) and (b) displays maps of the maximal tensile stress and the associated direction respectively as example s of the types of output that can now be attained from the model.

Experiment 3 uses an even more refined contour outline of Bering Glacier that more accurately reflects the main flow. This outline of Bering is used for the remainder of the experiments and is only extended when the Bagley Icefield is included. The result of this experiment displays a velocity in the upper part of the glacier that spans the entire width (see figure 4.10), which is more characteristic of accelerated glacier flow (Burgess et al., 2012; Kamb et al., 1985; Raymond, 1987; Turrin et al., 2013).

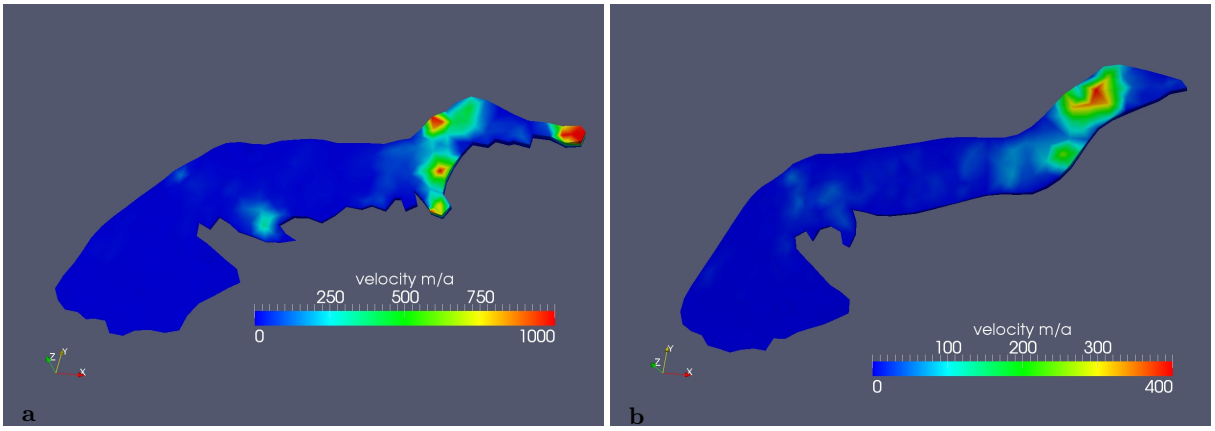

FIGURE 4.10: **Velocity maps of (a) experiment 1 and (b) experiment 3 displaying the effect of the glacier outline.** Both use identical parameters and whose only difference is the given contour outline.

Experiments 4 through 8 all deal with the implementation of an upper free surface (see section 2.2.4 for an overview of the concept and the mathematical details). This upper free surface allows the surface topography of the glacier to change over time so that we can analyze elevation change due to flow evolution and eventually accumulation and ablation (see experiments in section 4.3.7.2). Experiment 4 adds the free surface solver described in section 3.5.4.4 along with the mesh update solver described in section 3.5.4.5, but incorrectly implemented the required

changes to the material and boundary condition sections. Wild elevation gain and a sinking bed were observed in experiment 4's output, which served as a red flag for faulty implementation. The sinking bed occurred due to accidentally letting the bottom surface be a free surface as well, which was corrected in experiment 5, yet still displayed an unrealistic elevation gain throughout the glacier.

After an unsuccessful guess as to what the problem was in experiment 6, experiment 7 added an important criteria to the bed condition. This criteria states that the upper free surface cannot go below the fixed bed and that the glacier must be at its thinnest, one meter thick. That is, any place where the upper surface is calculated to be below the bed, that calculation is replaced by a command to set the upper surface one meter above the bed. This is an important criteria for not only for realistic results but also for numerical stability, and is used in the rest of the experiments. Despite this, it was still not the reason for the extreme elevation gain. After a lot of digging around through the Elmer/Ice documentation, it was determined that a variable called *Zs Top* needed to be defined to keep track of the changing elevation of the upper surface after each time step. This not only corrects the problem so that realistic elevation change is now displayed, but also gives us another variable that can be viewed in post-processing: surface elevation. This variable, along with a map of surface elevation gain, from a corrected experiment 8 can be found in figure 4.11 (c) and (d) respectively as more examples of what fields can be solved for and analyzed in the model.

4.3.1.3 Experiments 9-11: Increased simulation length

Experiments 9 through 11 are identical to experiment 8 and only seek to extend the simulation length by increasing the number of time steps. We go from 10 time steps corresponding to 10 days on experiment 8, up to 25 time steps in experiment 9, 50 in 10 and finally 100 in experiment 11. This was done in order to analyze longer term behavior of the glacier over the course of several months rather than 10 days. It is during these experiments where the matter of time required for a simulation to be computed and the amount of space required to store the generated data comes into serious consideration. At the current mesh resolution, each time step takes 30 seconds to a minute to complete and requires 2.4 MB of space to store.

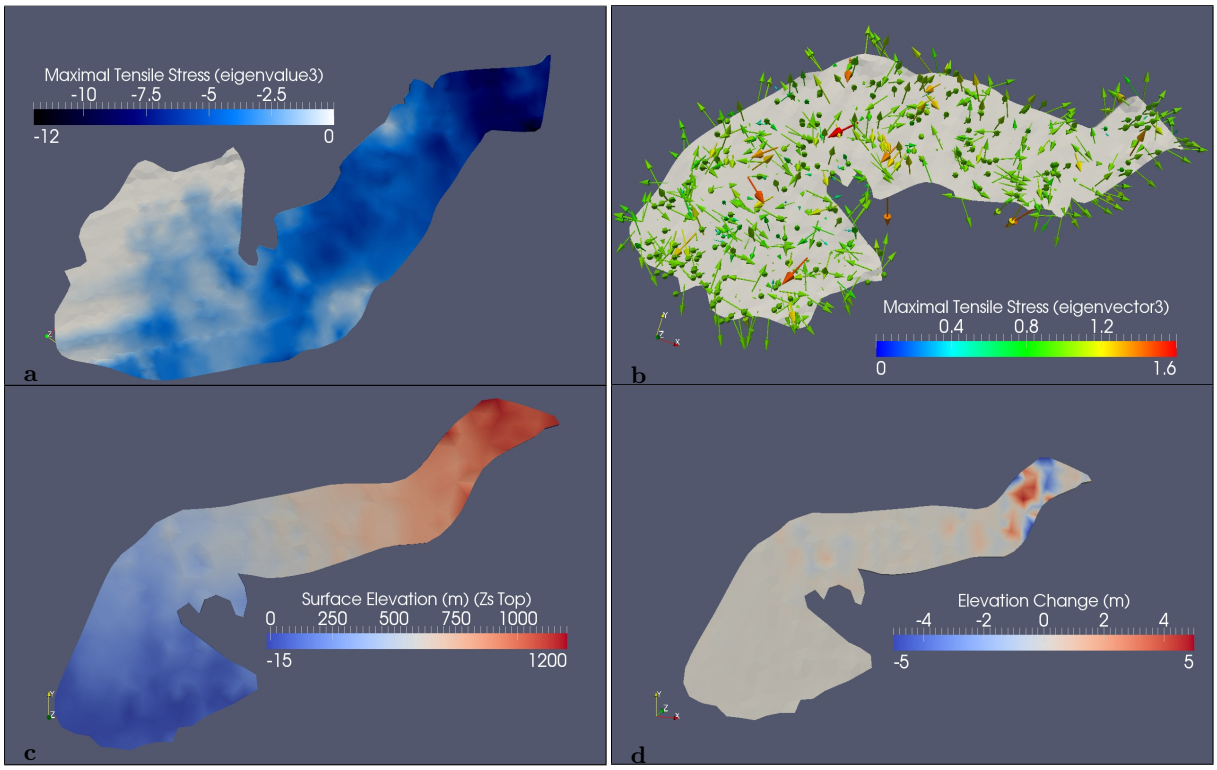

FIGURE 4.11: **Additional variable fields added in experiments 2 through 8 that can now be analyzed in the post-processing of simulations.** (a) The largest eigenvalue of the stress tensor corresponding to the maximal tensile stress that was added in experiment 2. Shown is the maximal tensile stress on the bottom of the glacier. Notice that it is negative everywhere, which corresponds to compressive stress. (b) Associated eigenvector to the largest eigenvalue in (a) corresponding to the direction of the maximal tensile stress. Note that (a) and (b) have a glacier shape that is unique to experiment 2. (c) Surface elevation above sea level, added in experiments 4-8. (d) Elevation change after 30 time steps (30 days) added in experiments 4-8.

Therefore, by increasing the amount of time steps by a factor of ten, we must wait 10 times as long for a simulation to complete and use 10 times more storage space to save our results. For simulations covering 100 days this is not that big of a deal, but eventually simulations over 25 years, corresponding to a full surge cycle of the BBGS, are sought and at the current rate, each model run could take upwards of a week and require almost 20 GB to store. Obviously, we want to run as many experiments as possible and so cutting down on the time of simulation is of high importance. One obvious way to decrease time and required storage of a model run is to decrease the resolution of the mesh and therefore the accuracy of our results, which is not ideal. The best way to decrease simulation length is to run the model in parallel on multiple processors,

preferably on a high performance super computer. An attempt at parallel implementation was done and the results of that enterprise are given in Appendix B. As time on University's super computer JANUS was limited, full simulations with all the desired complexities were not run in parallel. Therefore other methods or realizations are going to be needed to reduce time and storage, which will be addressed later in experimentation.

4.3.1.4 Experiments 12-28: Effects of a freely evolving mesh

With the addition of the mesh update solver, required when treating the upper surface as a free surface, specifications of the mesh update in all three cartesian directions need to be made on each boundary. On the bedrock boundary we set the mesh update in each direction equal to zero since we are assuming a rigid bedrock that does not change over time. At this point, this assumption holds for the lateral boundaries as well. For the upper free surface, the mesh update in the x and y-directions are set to zero and is left free to evolve in the z-direction. As mentioned previously, the elevation of the surface, i.e. the z-component of the glacier surface geometry, is stored after every time step. The reason we fix the update in the x and y-directions at zero is because we wish to analyze elevation change at fixed points on the glacier surface. If we let the x and y-components of our mesh nodes move throughout time, then elevation change in the vertical direction could not be properly analyzed because the points where we calculate elevation would be at different spots on the glacier after every time step. By not allowing our nodes to move horizontally, we can study the elevation change at fixed points on the surface throughout the simulation. To make sure that this assumption does not effect our results in any significant way, experiment 12 lets our mesh freely update in the x, y and z-directions. As is shown in figure 4.12 (e)-(h), velocity and elevation change (i.e. the z-component of the mesh update) does not change in any visible way, although the x and y-components of the mesh nodes did move slightly, bringing our elevation change results into question. Figure 4.12 (a)-(d) shows that the mesh would ideally update in the horizontal directions in places of high activity if we let it.

The remainder of the experiments in this section play with the assumption of fixing the mesh on the lateral and bedrock boundaries with the somewhat obvious conclusion that it is indeed

necessary to fix our mesh at the bottom and sides of the glacier. A fun, but not particularly enlightening experiment was done that placed no restrictions on the z-component of the mesh update variable at the bedrock. That is, the bottom boundary of the glacier is free to move up or down depending on the force acting upon it. The result, as shown in figure 4.13, shows the glacier bending downward more and more at the top of the glacier as time moves on.

As a quick side note, several experiments in this section consider the effects of a uniform accumulation rate across the entire glacier surface, each using a different mass gain constant. The results of these experiments are not shown here as a more accurate implementation of accumulation and ablation is done in later experiments and those results and subsequent analysis of the surface mass balance are given in section 4.3.7.2.

4.3.1.5 Experiments 29-30: Checking the numerics

An overview of the FEM formulation and the numerics used in this thesis is given in sections 2.3 and 3.5.4 respectively. The most computationally expensive, but also most important, numerics is done when evaluating the Stokes equations where there is a variety of direct and iterative methods to chose from for calculation. Direct methods are usually slower but do not use any approximations like the faster iterative methods (Atkinson, 2008). Based on later experiments with implementations in parallel, the iterative methods seem to be less stable and can lead to divergence at what seems to be random times. An elaboration on this experience can be found in Appendix B, where during an attempt of parallel implementation, the Stokes solver was forced to use iterative methods that behaved in unpredictable ways. For these reasons direct methods for solving the linear system in the Stokes calculations are chosen whenever possible. Up until this point, the direct method used was a Backwards Difference Formula of order one, or the *backwards Euler method*, given in one dimension as

$$\frac{u_i^{n+1} - u_i^n}{\Delta t} = F_i^{n+1}(u, x, t, \frac{\partial u}{\partial x}, \frac{\partial^2 u}{\partial x^2}), \tag{4.7}$$

for the partial differential equation $\frac{\partial u}{\partial t} = F(u, x, t, \frac{\partial u}{\partial x}, \frac{\partial^2 u}{\partial x^2})$. To see if simulation accuracy is changed, or time decreased, experiment 29 checks what would happen if a Crank-Nicholson

scheme was used instead. The Crank-Nicholson method is another implicit method and is actually a combination of the forward and backward Euler methods given as,

$$\frac{u_i^{n+1} - u_i^n}{\Delta t} = \frac{1}{2}[F_i^{n+1}(u, x, t, \frac{\partial u}{\partial x}, \frac{\partial^2 u}{\partial x^2}) + F_i^n(u, x, t, \frac{\partial u}{\partial x}, \frac{\partial^2 u}{\partial x^2})]. \tag{4.8}$$

Both methods are A-stable with the Backward Euler method having a larger absolute stability region encompassing all that of the Crank-Nicholoson method (Atkinson, 2008). After completion, experiment 29 yielded identical results and had no simulation time decrease and in fact ran about a minute longer than the BDF method for simulations of 25 years. For these reasons, and because backwards Euler has a larger stability region, only the BDF of order 1 is used for the remainder of the experiments when solving the linear system of the Stokes equations.

The BDF of order one has a local truncation error $\mathcal{O}(h^2)$ meaning we would expect to see a larger error for larger time steps (Atkinson, 2008). Wondering if time steps that corresponded to weeks instead of days would yield different results, experiment 30 uses 1300 time steps with intervals of 1/52 years rather than the day, or 1/365 year, time step used previously. After a 25 year simulation, comparisons to an identical run with day time steps show that the results are indistinguishable implying that for the current set up, simulations could be done using larger time steps if desired[1]. When only general overarching behavior is desired, these week time steps are used, but sometimes glacier evolution is interesting on the order of days. For example, most early simulations have a rapid change in behavior in the the first few time steps and therefore day length time intervals make sense to use.

4.3.2 Experiments 31-38: Simulations with an artificial bulge

Experiments done in this section alter the initial glacier surface in order to observe how glacier dynamics would behave.

For many surge-type glaciers a large "bulge" is observed in the reservoir area indicating that a glacier surge may initiate soon (Burgess et al., 2012; Frappé and Clarke, 2007; Herzfeld et al., 2013a; Lingle et al., 1993; Molnia, 1993; Shuchman and Josberger, 2010). This bulge then

[1] Often times, figures are not provided when experiments yield identical results.

collapses sending mass to the receiving areas. This is not to be confused with a surge front: a kinematic wave that propagates up and down-glacier thought to initiate the surge. A surge-front may at times be associated with a surface height increase, but here we define a bulge as the build up of mass in the reservoir area. A picture of such a surge-front taken during the summer 2012 campaign near the Khittrov Hills is shown in figure 4.14, shows an increase in surface elevation due to the collapse of a bulge in the reservoir area up-glacier.

The experiments done in this section introduce an artificial bulge to the surface DEM in order to observe its propagation through the glacier. A perfect model would produce a bulge after some 20 years of quiescent flow based on complex physical descriptions of the glacier and its reaction to its surroundings, but for now a bulge is given as an input to the model. These bulges are observed to be upwards of 2 km wide along the wave crest traverse to the flow, and 70 m high and can be observed anywhere between upper Bering to the lobus area (Herzfeld et al., 2013a; Lingle et al., 1993). Staring with experiment 31, an exaggerated bulge, 3 km wide, 7.8 km long and 400 m in height, is introduced at mid-glacier. While this bulge may be unrealistic in size and shape, it still serves as an interesting experiment of mass transfer throughout the glacier. Figure 4.15 gives an initial surface elevation plot with the introduction of this extremely large bulge.

The results of experiment 32 (an extended version of experiment 31) are shown in figure 4.16. Notice that we can observe propagation both up and down-glacier, with most mass moving down, by looking at the elevation gain as time moves forward. This bulge does not propagate down and up-glacier at speeds observed in the previous surges (Burgess et al., 2012; Lingle et al., 1993). This is because no change in the basal friction has occurred allowing for proper movement. If a surge front propagating at observed speeds is to be acquired, a change in the basal hydrologic system must be modeled as well. This could be done with a multivalued friction law. With an increased driving stress induced by the increased mass, we would expect the surge front to act like an activation wave changing the system as it moved past. Without this, the surge front will not resemble the observed propagation.

Experiment 33 seeks to observe the effect that basal friction has on the collapsing bulge. By

increasing the linear slip coefficient from 0.1 to 0.4, results are compared to the previous experiment after 500 time steps. Looking closely we can see that the bulge front down-glacier has not moved as far when the basal friction is increased. This tells us that basal friction effects the propagation of the bulge. It also shows that evolution of the surface topography is certainly affected by basal friction, which is what we expect (Cuffey and Paterson, 2010). Notice as well that the small pockets of elevation gain above and below the bulge seen in figure 4.17 (a) have almost disappeared in 4.17 (b). This shows once again that what happens on the surface of the glacier is strongly coupled to what is going on at the bottom.

Experiment 34 extends the simulation done in 32 up to 25 years, i.e. the approximate length of the surge cycle on the BBGS. This simulation is particularly interesting in that we can observe the long term mass redistribution of the bulge.

Figure 4.18 appears to show that after 1000 days, the bulge propagating downstream appears to break up into several pieces. As seen in figure 4.18 (c) and (d), some mass moves into the overflow area while most of the mass slowly moves down glacier into the lobus area. But if we compare this experiment to an identical one done without the addition of a bulge, as was done in experiment 38, we see that after 25 years of evolution, elevation gain throughout the glacier looks very similar. This tells us that the normal flow of ice is not interrupted by the bulge and that the course of overall mass redistribution of the glacier as a whole is not altered in any significant way. We can also see that most of the mass introduced as the bulge was redistributed to the glacial margins and the overflow area and not, as we may have guessed from experiment 34, down into the lobus. Clearly, more than just steepening of glacier geometry is needed to simulate a surge. By changing the hydrologic system, the bulge should effect the mass redistribution, and not simply by an addition of extra mass.

Due to the artificial nature of such an input, this path of experimentation was quickly abandoned in favor of simulations using only measured inputs and varied treatments of the glacier physics. If similar experiments were run again, a more realistic bulge would be introduced in a spot where the glacier bulge is thought to originate (in a reservoir area) coupled with the mathematical treatment of a hydrological switch at the base of the glacier.

4.3.3 Experiments 39-57: Alterations of boundary conditions

So far we have set the velocity in the direction normal to the bedrock equal to zero since ice should not be passing through the bedrock and we prescribe a linear friction law, described in section 2.2.5.2, with a slip coefficient of 0.1, in the tangential directions. Treatment of this friction law is a main focus of later experiments since basal sliding can account for the majority of ice movement (Cuffey and Paterson, 2010). No specifications of velocity are given to the upper free surface since we are letting the ice move freely.

Up to this point we have fixed the horizontal velocity on the lateral boundary equal to zero. In places along the lateral boundary constrained by mountains, this assumption makes sense because ice should not be allowed to pass through the rock. But in other places along the sides of the glacier, such as the Bering-Bagley junction, the glacier terminus or the boundary with the central moraine between the Bering and Steller Glaciers (see figure 2.1), this assumption is not necessarily accurate. With this realization, the assumption of treating the entire lateral boundary the same starts to come into question.

Experiment 39 looks to split up the side boundary into several different sections so that each can be given different conditions depending on where on the glacier they are. For example, most of the glacier boundary that runs parallel to the flow is restricted by mountains whereas the glacier terminus has no such restriction and in fact has a negative mass flux, that is, ice is being lost through this boundary via calving into a pro-glacial lake called Vitus Lake. On top of this, without the addition of the Bagley Icefield in the model yet, we should allow a positive net flux through the upper boundary at the Bering-Bagley junction representative ice being fed from the icefield to the Bering Glacier.

For the first couple of experiments, the lateral boundary was only split into two parts: the boundary of the glacier constraints by mountains and and glacier terminus. The Bering-Bagley junction and the boundary with the central moraine are included in the mountainous boundary and are not yet given separate treatment. The lateral sides constrained by mountains are now treated the same way as the bed. That is, the velocity is set to zero in the normal direction and the tangential directions are given a linear slip coefficient or 0.1. This means that sliding can occur along, but not through, the rocky boundary.

The glacier terminus in experiment 39 allows for a mass flux through the boundary in the normal direction. The mass lost through this boundary is thought of as ice lost from Bering via calving into Vitus lake. Unfortunately, this simulation diverged after only a few iterations for reasons not fully known. Instead, experiment 40 fixes this problem by dropping the flux boundary condition, yet allowing the mesh at the terminus to change in the vertical direction. Now any mass that would have been lost through the terminus now simply builds up at this boundary. Any vertical elevation change observed at the terminus can be thought of as ice lost via calving. Most simulations do not produce much activity near the glacier snout and therefore this effect of build up at the terminus is not noticeable. Because of this, later simulations will drop the division of the terminus from the rest of the lateral boundary.

We now wish to split up the lateral boundary even further to include a separate consideration of the Bering-Bagley junction. In experiment 42, we treat the glacier terminus and the lateral sides constrained by mountains the same as experiment 40 but now, at the Bering-Bagley junction, a positive normal mass flux is induced at the boundary. A total of 30 kg/m^2 per year is set. The actual amount of mass flux from the Bagley Icefield to the Bering Glacier is unknown and changes depending on the season and on which part of the surge cycle the ice mass is in, and therefore varying amounts of mass flux are tested.

This division of the lateral boundary to include the Bering-Bagley junction produces some very peculiar results. Some numerical inconsistency led to a massive loss of ice at the top part of glacier as seen in figure 4.20. This mass is lost to the entire system since we do not see an equal mass gain at other parts of the glacier.

Nearly every experiment that treats the Bering-Bagley junction boundary, and the conditions set there, separately resulted in identical behavior. Table 4.2 gives a list of these experiments and their respective boundary conditions on both the lateral mountain constrained boundary and the Bering-Bagley junction boundary.

Experiment 52 has a very large slip coefficient, on the order of 1e8, which is essentially the same condition as setting the velocity equal to zero since the friction would act as infinite. The only difference between the results of the experiments in table 4.2 is that in experiments with flux, there would be a buildup of mass near the Bering-Bagley junction as can be seen in figure 4.21.

Experiment	Lateral B.C.	Bering-Bagley Junction B.C.
42	Tangential slip condition	Mass flux of 30 kg/m^2
43	Tangential slip condition	Mass flux of 3000 kg/m^2
44	Tangential slip condition	Tangential slip condition
51	No fixed velocity of mesh update	No fixed velocity of mesh update
52	High slip coefficient in normal direction	High slip coefficient in normal direction
53	Velocity fixed at zero in every direction	Velocity fixed at zero in every direction

TABLE 4.2: **Experiments resulting in extreme mass loss in an indistinguishable manner.** A variety of experiments with different boundary conditions all behave nearly identical. Unless otherwise stated, the above experiments have a fixed mesh update at the two boundaries.

The only experiment that did not result in this extreme mass loss, but included a separate boundary for the BBJ, was experiment 50, which fixed velocity and the mesh update at zero in only the x and y-directions. For reasons that are unclear these were the only conditions that give different results than those listed previously. Perhaps the similarity of this condition to that at the free-surface is significant. The elevation change from this experiment after 150 days can be seen in figure 4.22

As one can see, the elevation change is drastically different and is in fact very small. It is interesting to notice that there is a small surface lowering near the BBJ and a small surface gain radiating outward from that lowering.

Despite this unfortunate and unrealistic result of extreme mass loss, interesting behavior can still be gleaned from these simulations. By looking at only the positive elevation change, we can track the mass flow of ice that is not lost through the edges near the Bering-Bagley junction boundary. The extreme mass loss acts like the collapse of a very large bulge or subglacial cavity. This massive lowering sends a wave of mass down glacier and the path of this ice movement follows the progression of observed surge fronts (Herzfeld et al., 2013a; Lingle et al., 1993). Figure 4.23 shows the propagation of this mass by tracking positive elevation gain over the course of approximately two years.

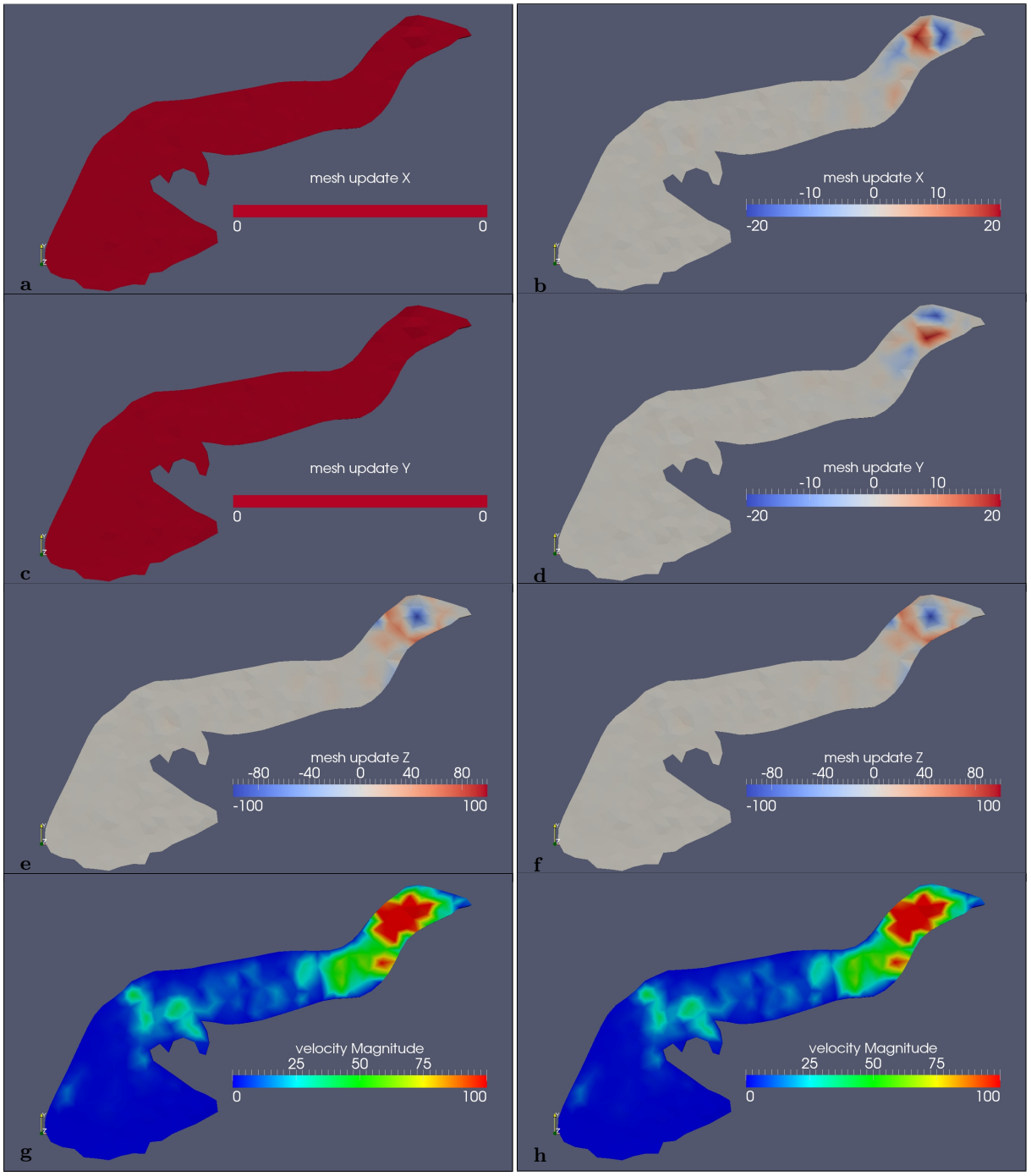

FIGURE 4.12: **Effects of allowing the glacier upper surface mesh to change in the horizontal directions.** Maps of the mesh updates in the x, y and z-directions and velocity magnitude from experiment 11 (left) that does not allow the mesh to update in the horizontal directions and experiment 12 (right) that does. Notice that elevation change (maps (e) and (f)) as well as velocity (maps (g) and (h)) are identical whether or not this assumption is held. Mesh updates are in meters and velocity is in meters per year.

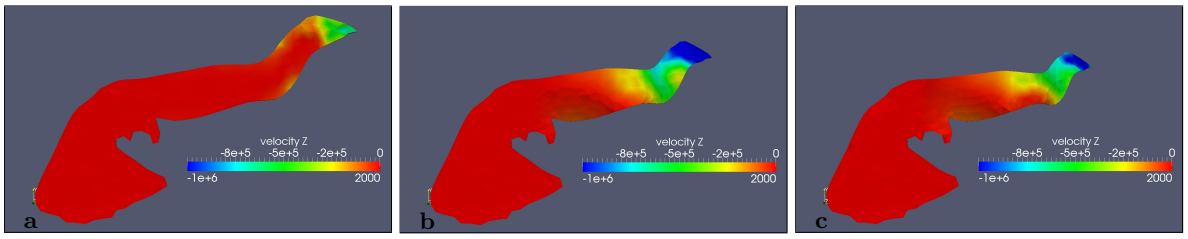

FIGURE 4.13: **Free mesh evolution of the bedrock boundary in the z-direction.** The results of experiment 20, where the z-compnent of the mesh update variable was not fixed at zero after (a) 1 time step, (b) 50 time steps, and (c) 150 time steps. Shown is the velocity in the z-direction in meters per year.

FIGURE 4.14: **Observed surface elevation increase on Bering Glacier in July 2012 due to the collapse and propagation of a bulge.**

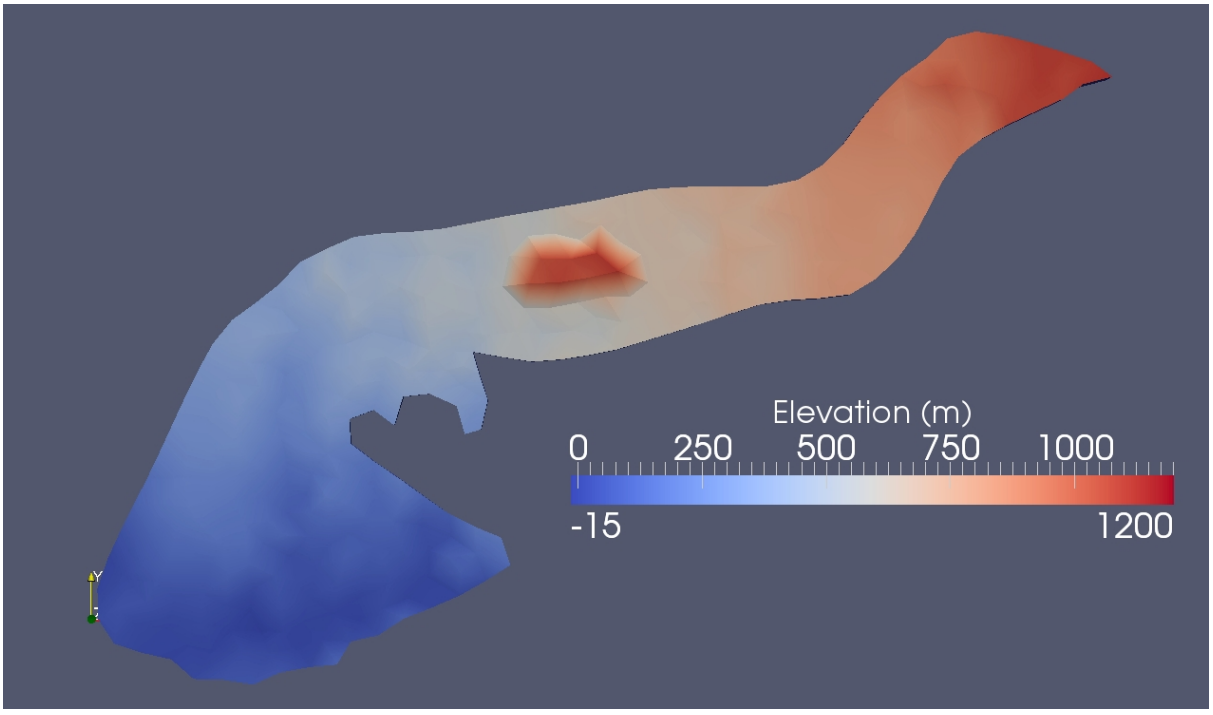

FIGURE 4.15: **Exaggerated bulge spanning 2 km wide and 400 meters tall, artificially introduced into the model.**

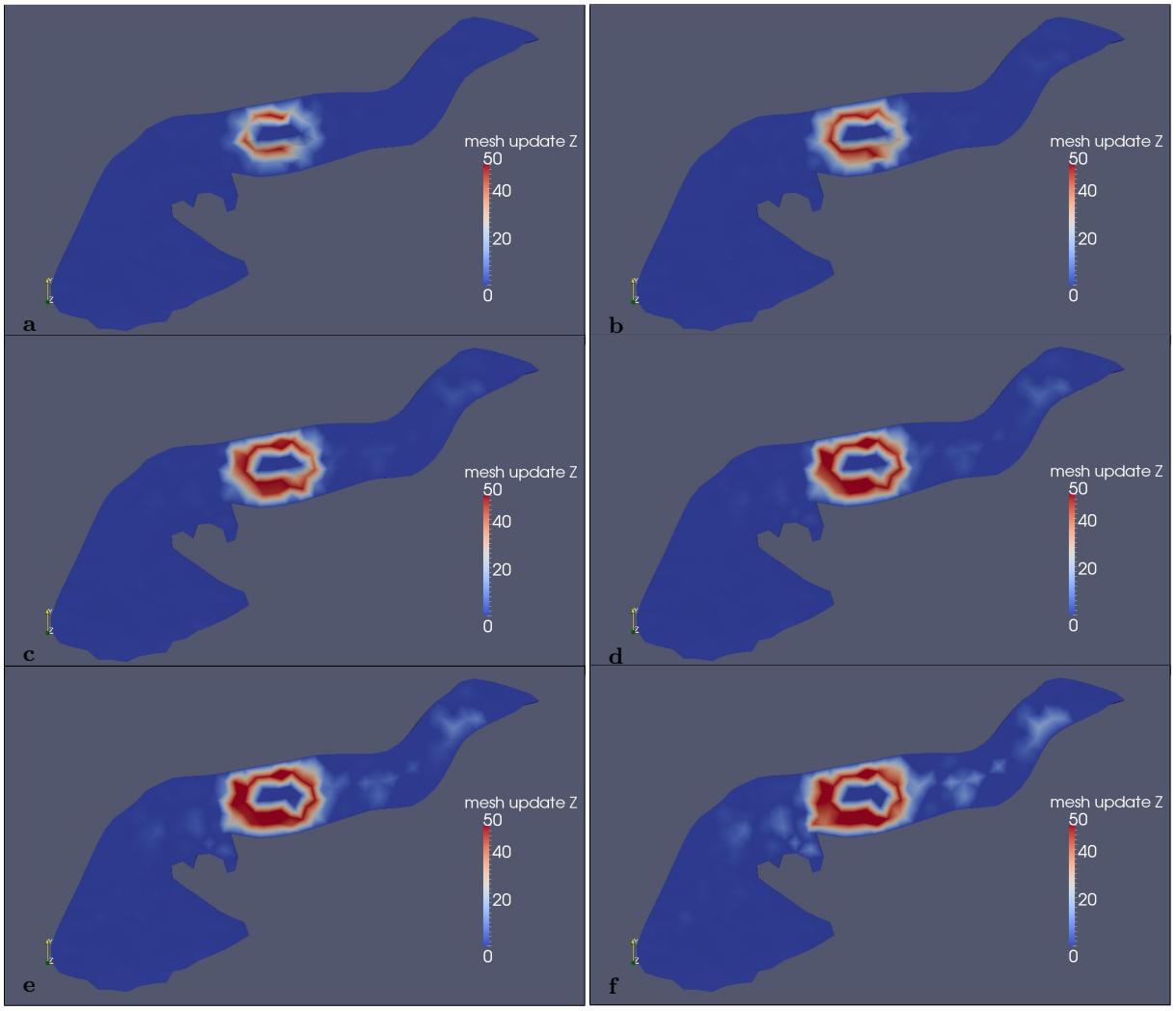

FIGURE 4.16: **Propagation of a bulge up and down-glacier.** The propagation of the bulge is measured by looking at elevation gain (m) as time moves on. Displayed is cumulative elevation change after (a) 5 time steps (or 5 days), (b) 20 time steps, (c) 50 time steps, (d) 100 time steps, (e) 200 time steps, and (f) 500 time steps.

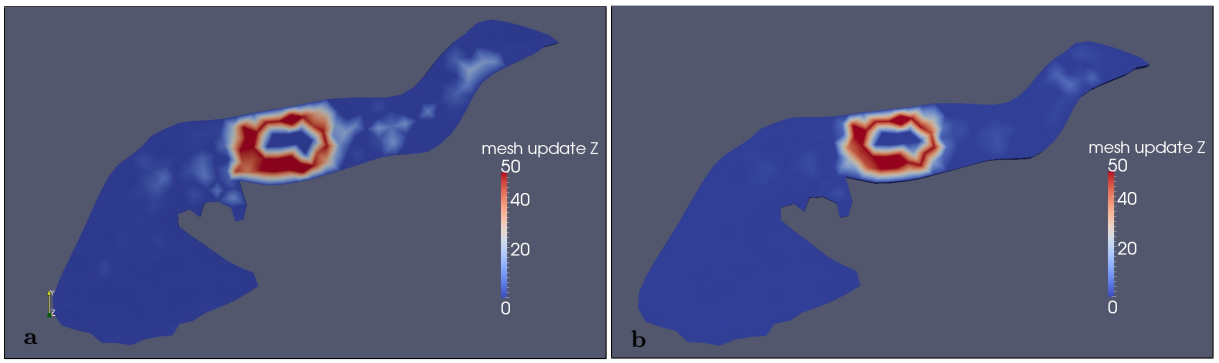

FIGURE 4.17: **Effect of bulge propagation with increased basal friction.** (a) shows the bulge propagation via elevation gain that obeys a linear basal friction law with coefficient 0.1 after 500 days. (b) The same thing only with a higher linear friction coefficient of 0.4. By looking directly above the overflow area and observing the extent of the high elevation gain (red), one can see that the bulge is propagating slower on the surface when basal friction is higher.

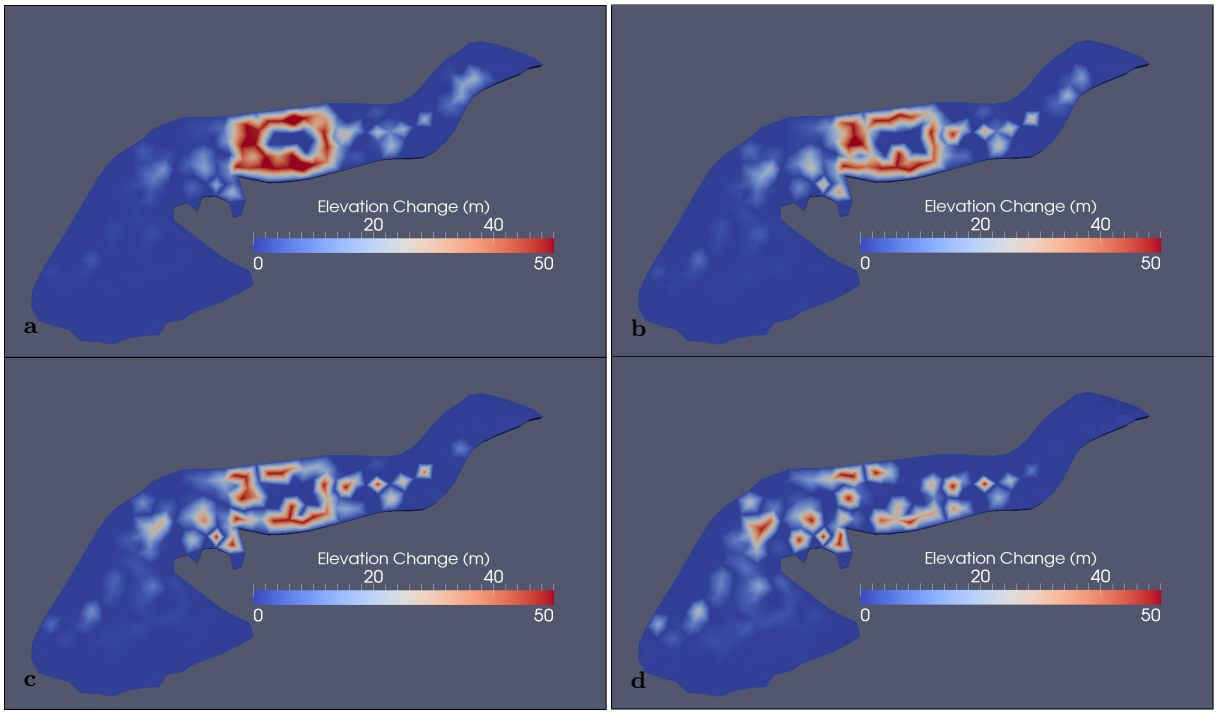

FIGURE 4.18: **Long term mass redistribution with a bulge.** Using the same 400 m tall bulge, glacier evolution was carried out for 25 years (the approximate length of a surge cycle of the BBGS). (a) After 1000 days, (b) after 2000 days, (c) after 4000 days and (d) after 9125 days (or 25 years).

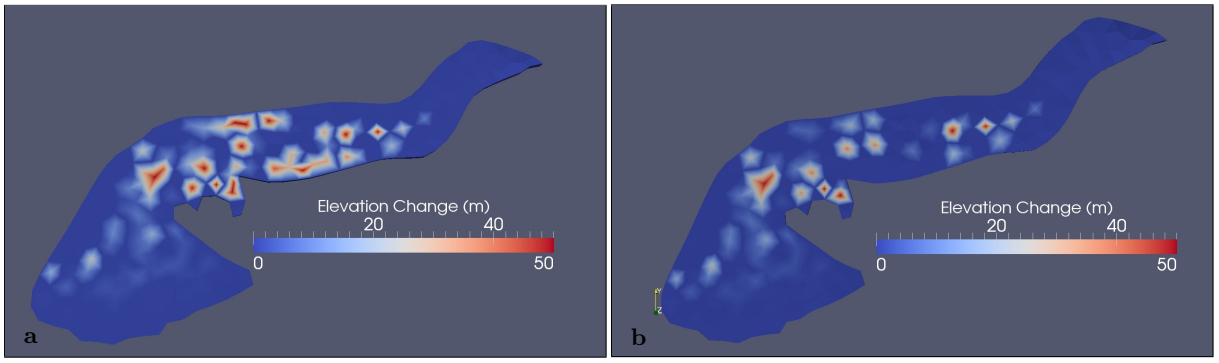

FIGURE 4.19: **25 year flow evolution comparison (a) with and (b) without a bulge.** Notice the differences around the overflow area as well as the glacier margins near where the bulge originates.

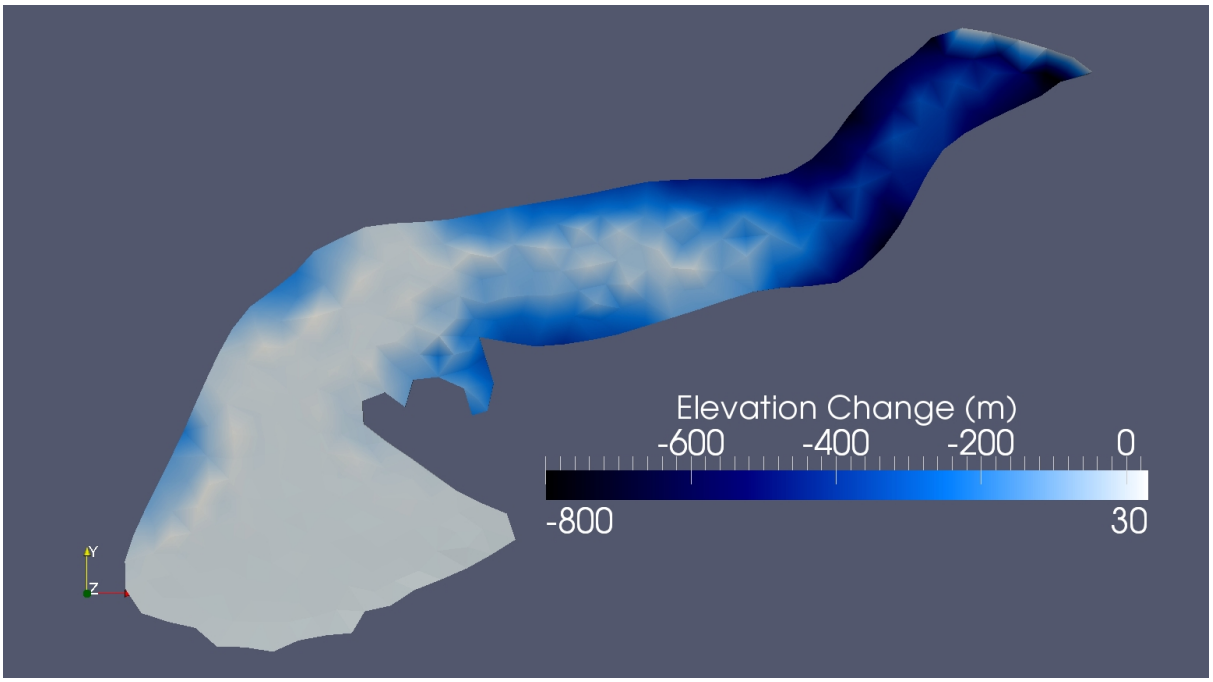

FIGURE 4.20: **Extreme mass loss observed in experiments that have a separate boundary for the BBJ.** After two years, surface elevation has dropped over 800 meters in some places near the margins in the upper glacier. Yet there are a few places throughout the glacier that have small ($<< 800m$) positive elevation gains.

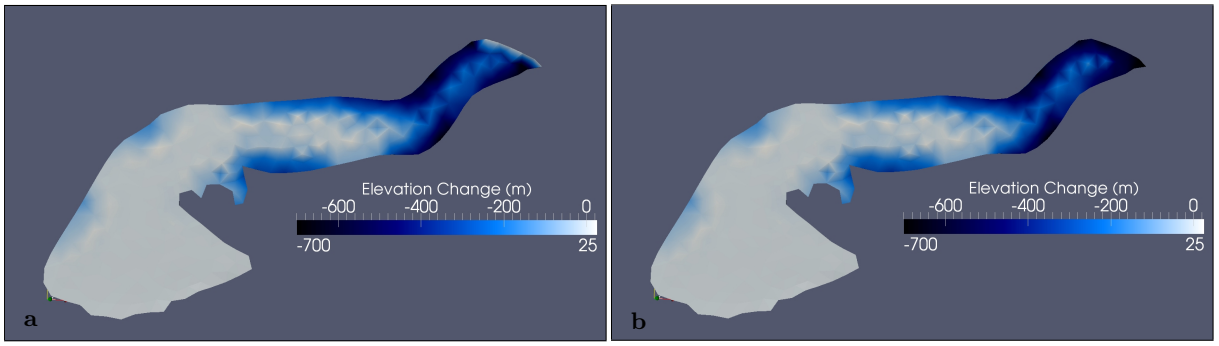

FIGURE 4.21: **Difference between (a) flux and (b) no flux in simulations with the BBJ boundary after 150 time steps.** The simulations displaying extreme mass loss are almost identical except for a small mass buildup near the BBJ when there is a positive flux coming through the boundary.

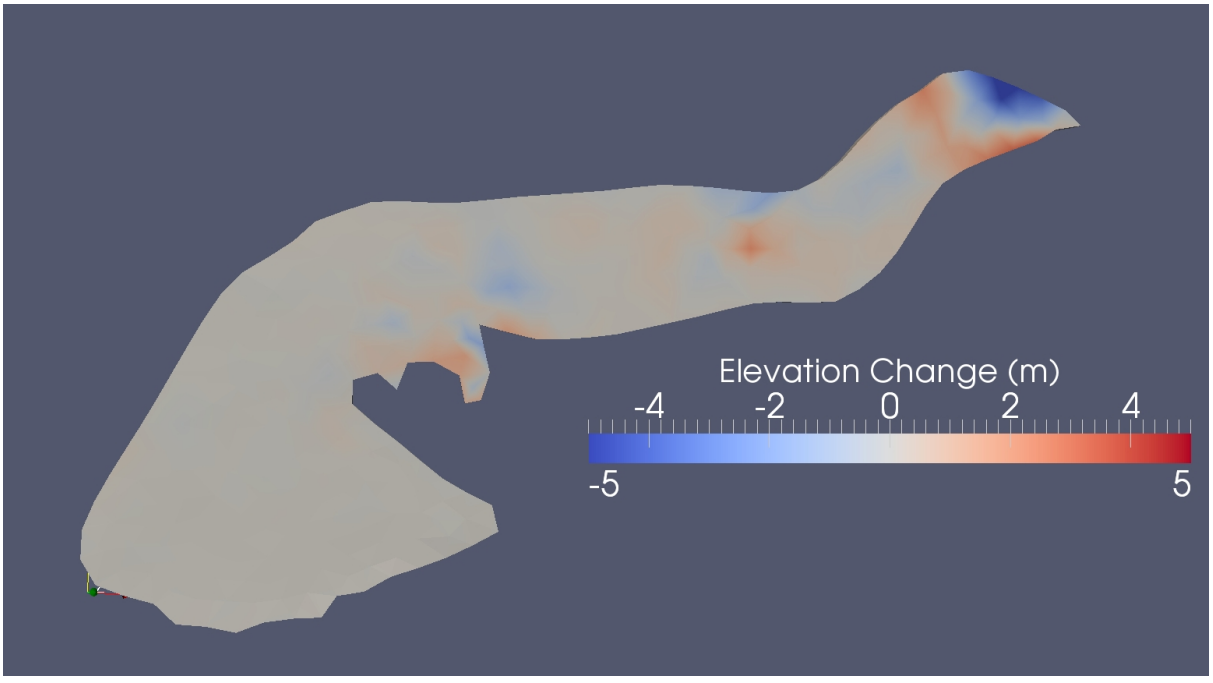

FIGURE 4.22: **Elevation change from experiment 50.** This is the only experiment with the BBJ boundary that did not result in an extreme mass loss in the upper part of the glacier.

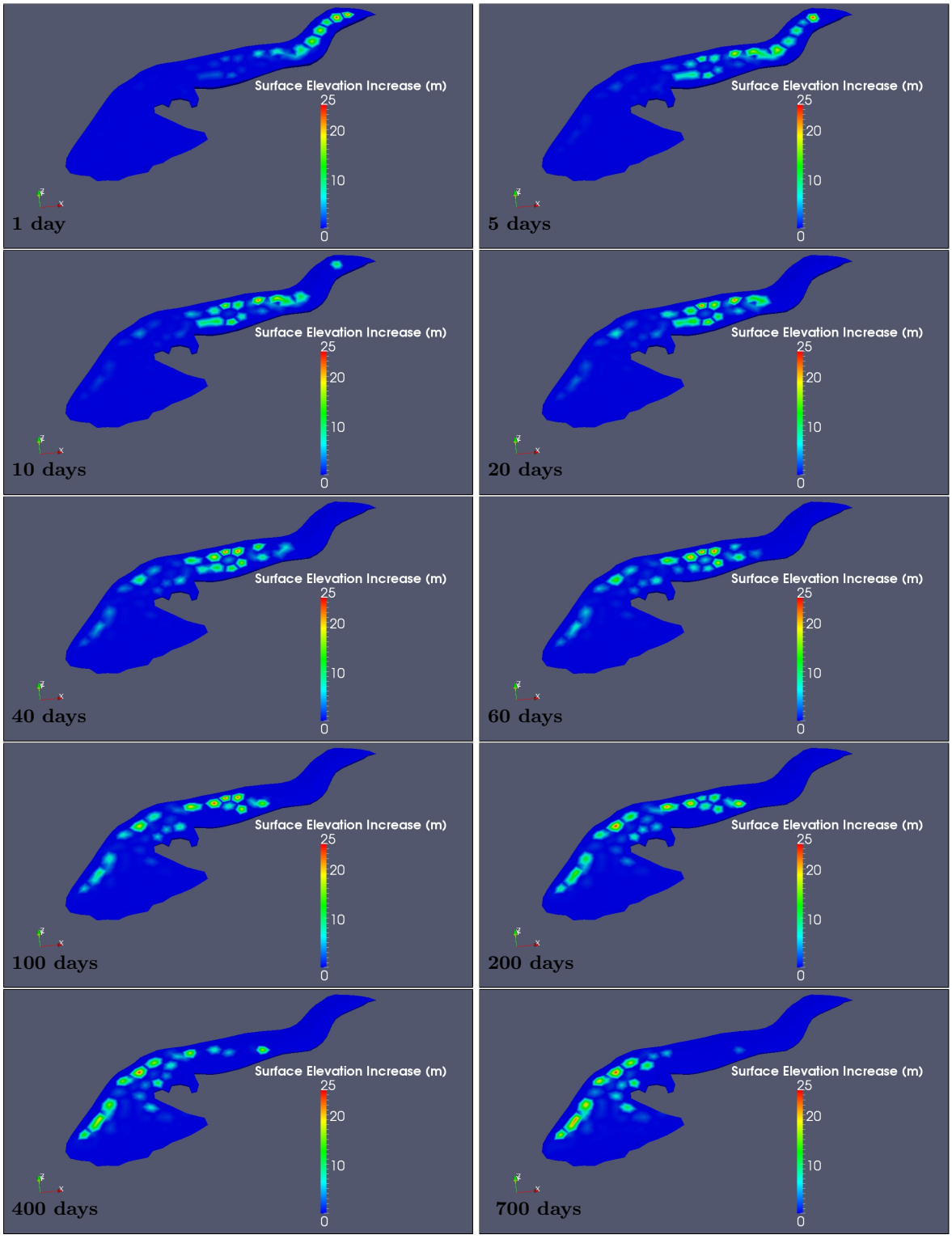

FIGURE 4.23: **Propagation of elevation gain down Bering Glacier.** By only looking at positive elevation gain, we can see the mass from a giant surface collapse flow down-glacier in way that resembles mass flow in the BBGS.

Notice that this experiment also shows two different flow regimes: a northern one that extends through Tashalich arm and into the lobus area and a southern one that eventually curves around the Grindle Hills. An attempt to try and realistically recreate this interesting event, due to its similarity to a surge front, is done in one of the final presented experiments when a large subglacial cavity is introduced near the Bering-Bagley junction.

There are a few experiments in this section that were not mentioned because they dealt with failing attempts at implementing nonlinear friction laws, which will be attempted again in later experiments.

4.3.4 Experiments 58-60: Introduction of the Bagley Icefield

Up until this point in experimentation, the Bagley Icefield was not included in the model because of a lack of bed elevation data there. After the JPL WISE campaigns in 2008 and 2012, access of the bed data, introduced in section 3.3.1.2, was finally given to our group. Once attained, a full bedrock DEM was generated for the entire Bering-Bagley System using the combined bed measurements of the three expeditions described in section 3.3.1.2 (see section 4.1.3 for the DEM).

As for the surface topography, Cryosat-2 data from summer 2012 was still used over Bering Glacier, but coverage from a six month interval was deemed insufficient for a proper DEM for the Bagley Icefield and so surface elevation data from the entire two year period was used when kriging for that area. This lack of coverage on the Bagley from six months of measurements, which provided sufficient for coverage over Bering, is due in part to the track lines being perpendicular to the length of Bagley. For this reason, every pass of the satellite measures only a small amount of the surface of Bagley Icefield, whereas because parts of Bering are more parallel to the tracks, it receives many more measurements per pass (see figure 4.25). Adding to this dilemma are the large and rugged mountains on either side of the ice valley. Faulty phase information returned to CryoSat-2 can cause inaccurate measurements when steep and rugged terrain is passed over. As seen in figure 4.25 (b) and (d), the data over Bagley was already filtered by the time we got the L2 data product most likely due to the effect of the mountains. On top of all this, there are many bad tracks displaying unrealistic measurements that need to be thrown out. Because no time series analysis is done for the Bagley Icefield, and since most

surge activity is in Bering Glacier, a combination of data over the two-year period for the Bagley Icefield is acceptable with BBGS simulations. Figure 4.24 shows the center flow line spanning the entire system.

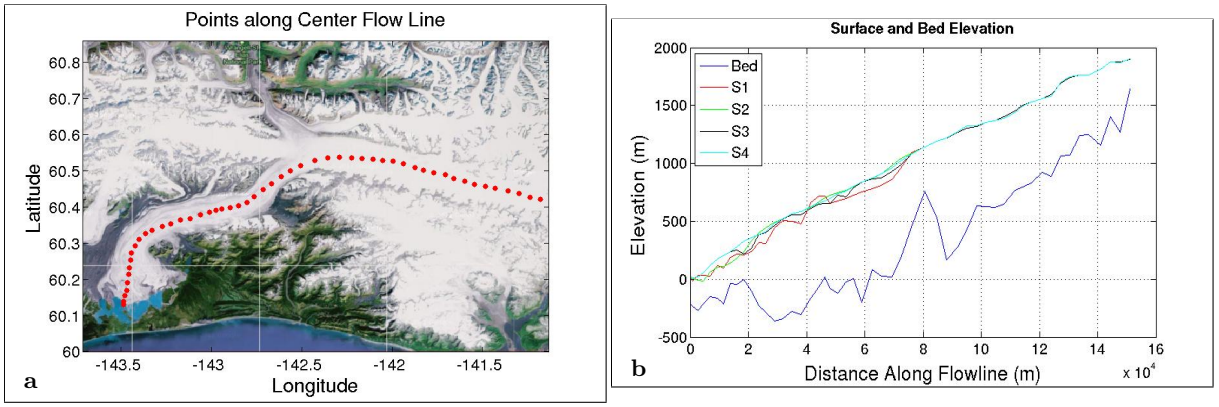

FIGURE 4.24: **(a) The central flow line along the BBGS at discrete points and (b) the bedrock and surface profiles along this path.**

Experiment 58 simulates the entire BBGS for the first time over the course of two years. Due to the doubling of our problem size, simulations now take about twice as long and take up to twice as much space as simulations of Bering Glacier only. Experiment 59 checks that time intervals of 1/150 years results in a well-behaving simulation, so that experiment 60 can use that step size to execute a model run that simulates 25 years of glacier evolution. The elevation change results at different time steps throughout the 25 year simulation are shown in figure 4.26.

Experiments with the inclusion of the Bagley Icefield are kept consistent with previous simulations in material and body force specifications and solve for the same field variables. Experiment 60 uses a linear friction law at the bedrock boundary condition with a slip coefficient of 0.1. The upper surface remains a free surface that moves in the z-direction and the singular lateral boundary is fixed and has a zero-velocity condition in each direction. Note that there is no longer a reason for a Bering-Bagley junction boundary, and since little activity occurs at the terminus (see figure 4.26), only a single lateral boundary is considered. Notice the high activity near the Bering-Bagley junction and right above the overflow area. These are areas of particular interest for surges in the BBGS as they are thought to be the possible nucleation point of the

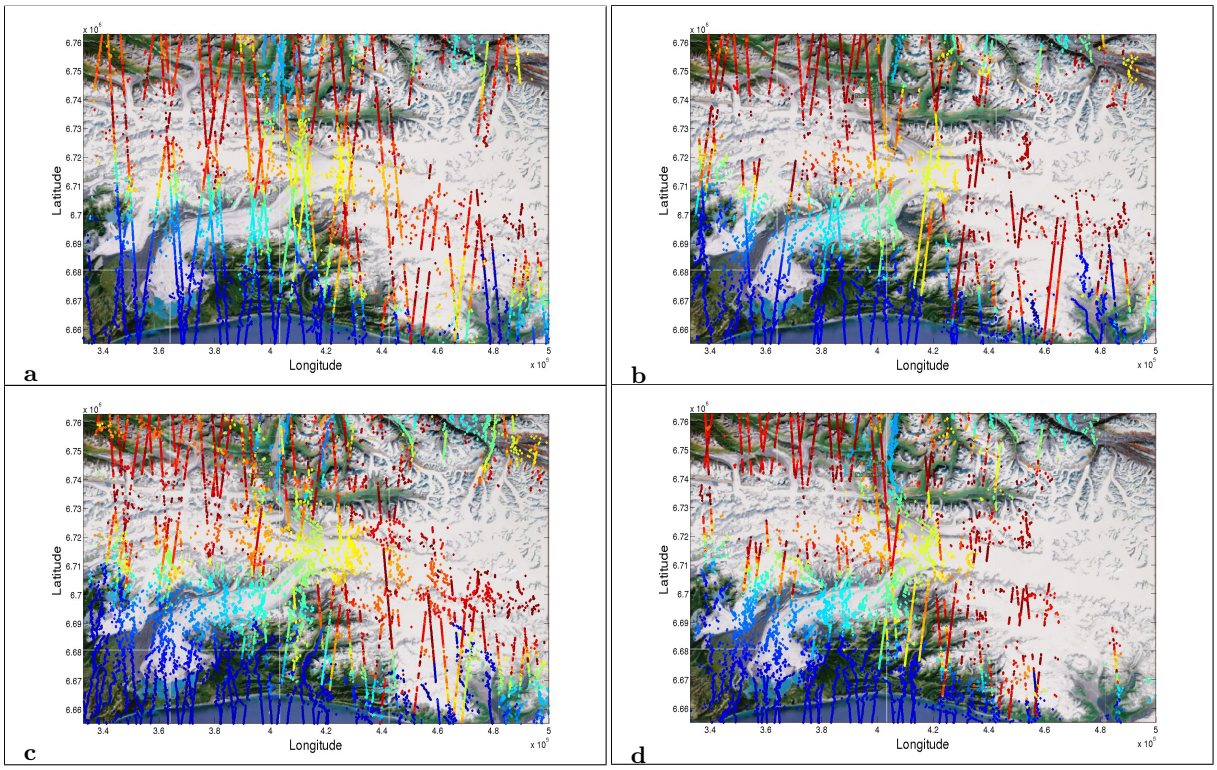

FIGURE 4.25: **Unfiltered CroySat-2 data over Bering Glacier and Bagley Icefield for four time periods.** (a) Summer 2011 (May 2011 to September 2011), (b) winter 2011/2012 (October 2011 to April 2012), (c) summer 2012 (May 2012 to September 2012), and (d) winter 2012/2013 (October 2012 to April 2013). All the surface data over Bagley was combined into a single data set for deriving a surface DEM in that region.

kinematic wave and trigger point of the surge respectively (Burgess et al., 2012; Roush et al., 2003; Turrin et al., 2013). This leads us to believe that while the actual surge acceleration may be due to the basal hydrology, the triggers of the surge may be due to the bedrock topography or some other mechanism that is currently included in the model.

4.3.5 Experiments 61-75: Revelations from parallel implementation

Experiments 61 through 73 all had to deal with the parallelization implementation on the University of Colorado's supercomputer JANUS. Many of these dealt with various mesh refinements, i.e. different problem sizes, by checking their serial run times. Elmer/Ice gives an estimated total run time after every iteration based on the time it takes to calculate each previous iteration, and so run times can be estimated without having to calculate the entire simulation. In the end,

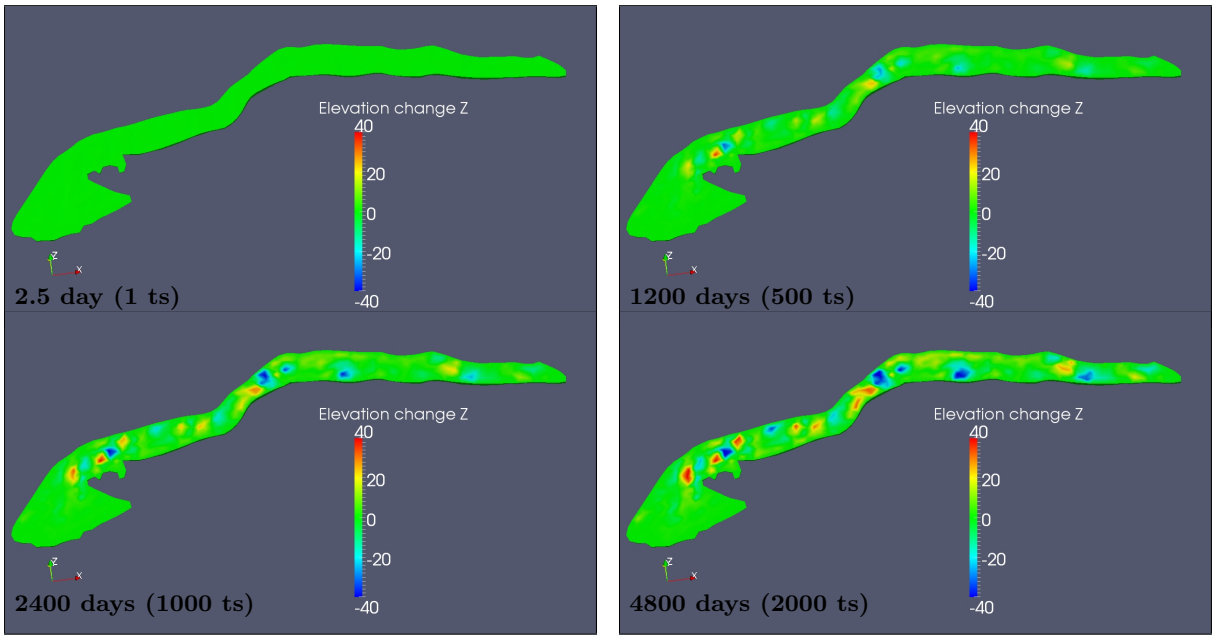

FIGURE 4.26: **Elevation change over the entire BBGS.** Time steps is 2.4333 days (1/150 years), elevation gain in meters (experiment 60).

serial times were calculated by running experiments on a single processor on JANUS, rather than the aforementioned method on the local desktop. Results of the parallel experiments can be found in Appendix B.

Implementation in parallel is all about reducing time of calculation and so after experimenting on JANUS, a somewhat obvious way a reducing time was uncovered. Up until this point a total of 20 vertical layers were being extruded in a fashion described in section 2.3.1. There was no particular reason for such a high number of layers other than the ratio of layers to average glacier depth was kept constant compared to other glacier models implemented in Elmer/Ice. After a single experiment it was uncovered that cutting the total amount of vertical layers down to three does not effect our solution on the surface or the bottom where we are most interested, but does reduce the number of nodes, and therefore calculation time and required storage are cut down by a factor of 20 to 3 (since each vertical layer is comprised of the same amount of nodes).

With the problem size cut down by so much, the resolution of the mesh can be increased and total execution time would be the same or less than it always had. A new mesh was created with element sizes of about 1000 meters (reduced from 2000 m) bringing the total amount of nodes

to 6993 (2331 per layer). This is half of the total amount of nodes previously at 12,780 (639 nodes per layer) but with four times the resolution on a horizontal layer. Identical simulations were carried out on the two different meshes and is shown in figure 4.27.

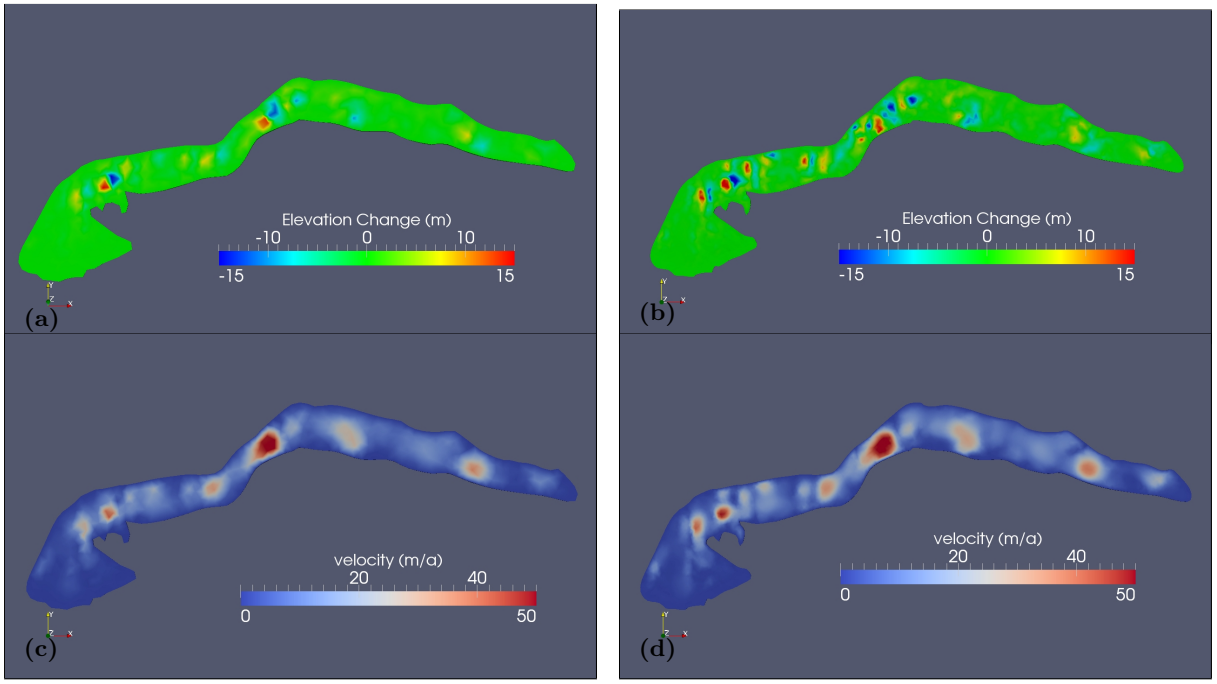

FIGURE 4.27: **Effects of refining the mesh by a factor of four after a year-length simulation.** By decreasing the length of the element in the plane by half, we increase the horizontal resolution by a factor of four. (a) and (c) show elevation change and velocity at low resolution while (b) and (d) show them at high resolution.

Places where there was once only a mild elevation change now have a much more pronounced gain and/or loss. This is due to the fact that before, elements were so large that they covered surfaces that would have experienced both an elevation loss and a gain, and thus evened out to show only a mild change over the element as a whole. With smaller element sizes, tiny surface mass transfers are uncovered and we find that the surface is much more active than previously thought. Velocity maps are still very similar, but we can now see more refined areas of movement with a higher resolution.

4.3.6 Experiments 76-79: Simulations using each of the derived surface DEMs

Up to this point in experimentation, all simulations have taken the DEM from summer 2012 (abbreviated by s3) for the initial surface elevation of Bering since it has the lowest average error margin as determined in section 4.2. This series of experiments uses each of the four derived Bering Glacier DEMs from CryoSat-2 data as inputs for the model. Doing this allows us to attain numerically derived difference maps that can be compared to those created in section 4.1.2. For example, if we start with the DEM from summer 2011 (s1) and we let it evolve for six months and then find the difference in surface elevation, we could compare this with the difference map of winter 2011/2012 - summer 2011 as seen in figure 4.28 (a) and (b). Since there has been nothing added yet that tells the model it should surge (i.e. rapidly accelerate), we do not expect to see exact correlation between the two difference maps. This may however, allow us to distinguish what changes are surge features and what are due to normal flow.

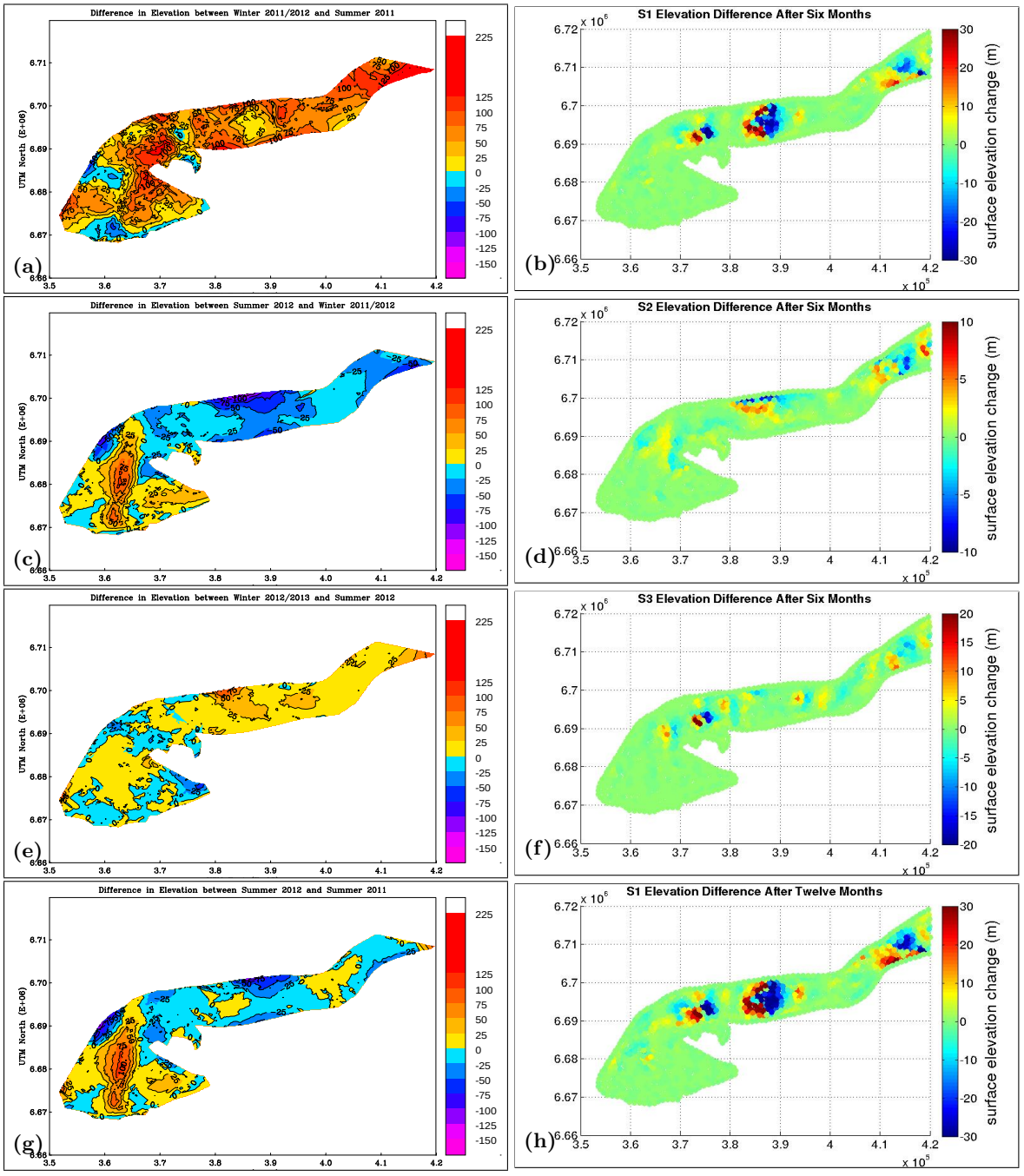
Difference in Elevation between Winter 2011/2012 and Summer 2011
Difference in Elevation between Summer 2012 and Winter 2011/2012
Difference in Elevation between Winter 2012/2013 and Summer 2012
Difference in Elevation between Summer 2012 and Summer 2011
UTM North (E+06)
S1 Elevation Difference After Six Months
S2 Elevation Difference After Six Months
S3 Elevation Difference After Six Months
S1 Elevation Difference After Twelve Months
surface elevation change (m)
x 10^6
x 10^5
(a)
(b)
(c)
(d)
(e)
(f)
(g)
(h)

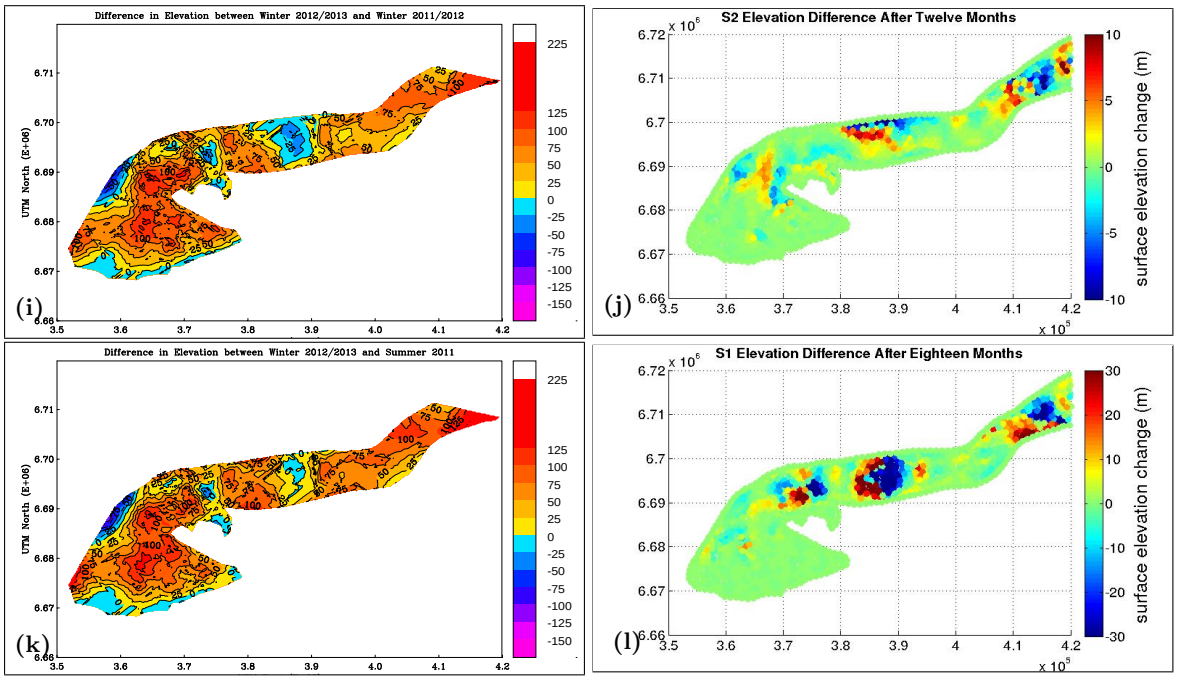

FIGURE 4.28: **Comparisons between observed elevations differences and simulated ones.** The figures on the left are those created from CryoSat-2 observations and geostatistics, while those on the left were numerically derived. Notice the different scales.

Comparing figure 4.28 (a) and (b) we see that the large surface lowering in the central-Bering that was numerically simulated corresponds nicely to the yellow anomaly in the observed difference map. The anomaly is a small surface increase (less than 25 meters) compared to the much larger surface increases surrounding it. Accounting for error and accumulation (which is not yet considered in the model), this anomaly could very likely have been a surface lowering. The small surface lowering right above the overflow area is also shared by both maps as well as a large surface increase closely down-glacier. A slight surface decrease can be seen in Tashalich arm in both maps. The activity simulated near the Bering-Bagley junction is not reflected in the observed difference map although keep in mind that this was the area of maximum error.

Figure 4.28 (c) and (d) share the characteristic of surface lowering along the northern margin at mid-glacier. Note that the boundary conditions fix the elevation at the lateral boundary for numerical stability and therefore the green outline surrounding the numerically derived difference maps should be ignored. A surface increase is shared in the middle of the upper lobus between areas of surface lowering, but elevation gain in the center of the mid and lower lobus is

not found in the numerical map. Once again the two maps do not agree at the BBJ, but there is little observational data near the junction for winter 2011/2012.

Maps (e) and (f) have very little in common. A surface increase (and down-glacier increase) is found in (f), similar to the one in (b), but no such change was reflected in (e). There is however a small surface increase near the bend in the mid-upper glacier that is shared by both maps.

Maps (g) and (h) also display little similarity. There is an observed surface increase along the bend in the mid-upper glacier in (g) whose upper part is shared by (h). During a surge we expect high water pressure at the base in water filled cavities that usually form on the lee-side on a bedrock undulation such as the one observed at the BBJ. This leads us to suspect high water pressure there, and thus faster sliding speeds, right below the BBJ during a surge that could explain why the observed elevation gain in (g) extends further down glacier than in (h). The small elevation gain at mid glacier in (g) trailed by a larger elevation decrease near the margins is somewhat similar to that of (h). Once again, ignoring the green outline of the glacier, we could assume that the surface lowering found in (h) would extend to the margins.

Figure 4.28 (i) and (j) share the behavior of surface lowering along the northern margin at mid-glacier, but (i) shows lowering along the entire width of the glacier where (j) does not. Lowering along Tashalich arm is also shared in both but there is a discrepancy along the Grindle Hills area. Map (i) shows large surface increases along the bend whereas map (j) shows a lowering. This could imply that the observed elevation increase in this area is a surge effect. Once again, activity near the BBJ is dissimilar.

Lastly, maps (k) and (l), corresponding to a full 18-24 month change in surface elevation, clearly share similar properties. The large area of surface lowering and down-glacier rising found in central-Bering is shared by both maps as well as the smaller but similar one above the overflow area. A small lowering can be seen along Tashalich arm in (l) but not near the magnitude of drop observed in (k). Again, the large observed elevation increases surrounding the Grindle Hills was not simulated by the model, pointing to it being a side effect of the surge. Elevation changes below the BBJ also differ.

4.3.7 Experiments 80-91: Flow parameters, accumulation and sliding laws

4.3.7.1 Changing flow law parameters

Glen's flow law given by equations 2.8 - 2.10 tells us how our flow would be altered by changing the parameters that relate the deviatoric stress to the strain-rate. The effective viscosity is restated,

$$\eta = \frac{1}{2}(EA)^{-1/n}\dot{\epsilon}_e^{(1-n)/n}. \tag{4.9}$$

Elmer/Ice requires that we give it the values of the n, E and A before any calculations are done. The Glen exponent n can range anywhere from 1.5 to 4.2 but has solid empirical evidence for being equal to 3 for temperate ice (Shroder et al., 2011). None the less, experiment 81 looks at the effect of reducing the Glen parameter from 3 to 2 and thus exponentially reducing the effective viscosity of ice. The difference in flow velocity at the surface can be seen by comparing figure 4.29 (a) and (b). A nice and well-defined table for values of the prefactor A is given in Cuffey and Paterson (2010) for given ice temperatures. With a constant ice temperature of $-1°C$, a value for A can be found and used with high confidence. The effect of increasing it by a factor of ten would decrease our viscosity by $\frac{1}{1000}$ assuming our Glen exponent is equal to three. This could physically represent warmer ice, whose viscosity is lower, and its effect on surface velocity is seen in figure 4.29 (c). With n and A having values that are well known, the only parameter that makes sense to vary is the enhancement factor E. The enhancement factor exists in Glen's Flow Law to account for variations that are not explained by stress and temperature, which could include effects of grain size, impurities, or fabrics (Cuffey and Paterson, 2010). Therefore we could increase E if the model produces flow velocities that seem too slow as a simple way to match observations. Increasing the enhancement factor by 5 would decrease the effective viscosity by $\frac{1}{125}$ (with $n = 3$) and its effect of surface speeds can be seen in figure 4.29 (d).

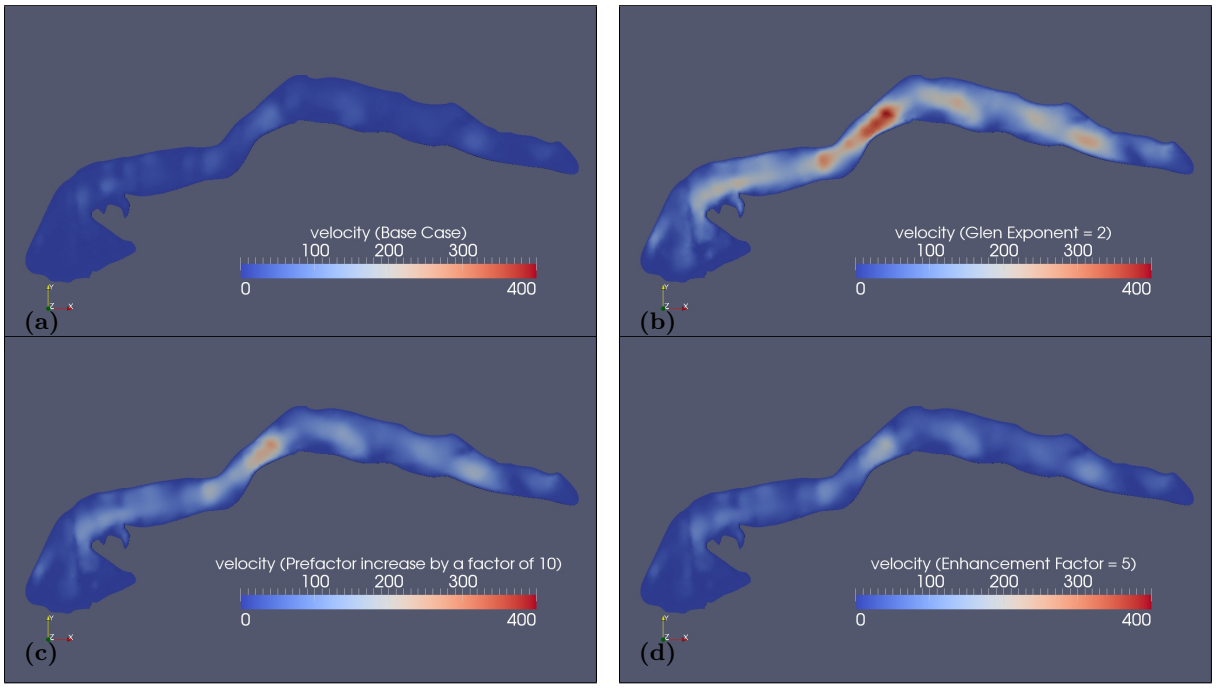

FIGURE 4.29: **Effects of certain ice flow parameters on surface velocity after one day.** (a) The base case simulation using the DEM from summer 2012. Parameter values for this case can be found in table 3.1. (b) Decreased Glen Exponent from 3 to 2. (c) Prefactor increased by a factor of 10. (d) Enhancement factor increased from 1 to 5.

4.3.7.2 Addition of accumulation

Accurate accumulation is now added into the model as a way to add mass to the system in non-uniform yet realistic way. Accumulation measurements on the Bering Glacier were made and graphed versus altitude by Muskett et al. (2009). This graph gave accumulation measurements over a 16 day period that showed a near linear relationship with altitude. Using this information, a linear relation between annual snowfall and elevation was derived. This expression is given by,

$$a_s = 1 + 0.003 \cdot z_s \tag{4.10}$$

where a_s is accumulation and z_s is surface elevation, both given in meters. This would suggest that snowfall near the highest elevations in the east Bagley Icefield ($\sim 2000\ m$) would receive about 7 meters of snowfall, which is on par with other estimates of snowfall in that region (Osborn, 2013). If one wanted to account for surface melting, or ablation, we could subtract

the snowfall total at the ELA, i.e. the division between ablation and accumulations zones, so that annual atmospheric contributions to surface elevation change are positive in accumulation zones and negative in ablation zones. A net positive accumulation throughout the entire glacier using equation 4.10 is done in experiment 85, whose elevation change results after five years is shown in figure 4.30.

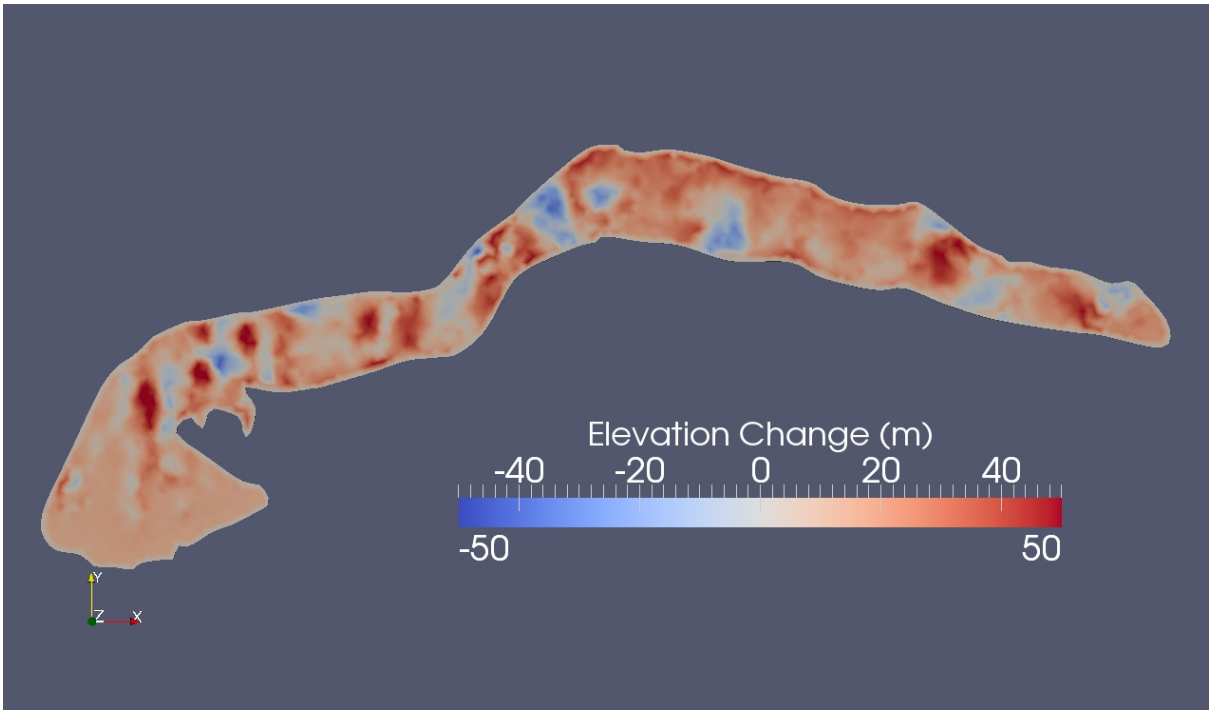

FIGURE 4.30: **Elevation change from experiment 85 that adds accumulation.** After five years, an overall elevation gain is seen throughout the glacier with most of the larger elevation changes remaining unchanged from previous experiments.

Adding uneven accumulation tends to steepen the glacier geometry, but over time periods much longer than five years. Glacier dynamics seem to be unchanged by the addition of accumulation, except for an over all general increase in surface elevation. Simulations will need to be carried out for much longer time periods, at least on the order of a surge cycle, to see the full effects of accumulation. Unfortunately the addition of accumulation/ablation came late in experimentation and a longer simulation was never run out of preference to other, shorter experiments.

It is noted here of a potential downfall of the elevation change maps that are created for longer simulation lengths. Since these maps measure the *cumulative* elevation change starting from initial surface DEM, any inherent instability in the glacier geometry will always even out fairly

quickly and these immediate, sometimes drastic changes will be seen throughout the entire long-term simulation. This is true especially for initial glacier topography that was measured in a surge such as the ones used in these experiments. A way to correct for this when running longer experiments, is to first run a steady-state simulation using the initial geometry and then feed the steady state glacier geometry into a longer transient run.

4.3.7.3 Addition of a nonlinear friction law

The next few experiments look to tamper with the basal friction laws given in section 2.2.5.2. Many attempts were made to implement the nonlinear friction laws but every try resulted in instability. Some implementations took longer to diverge and those results are presented here to see the effect that various friction laws had on ice velocity. The easiest and most stable way to alter the basal friction law is to change the linear slip coefficient. The effect of reducing the slip coefficient from 0.1 to 0.01 on ice velocity at the surface and at the base is given in figure 4.31 (c) and (d). The Weertman sliding law seemed to always diverge the quickest but its effect on velocity, despite the emerging instability, is shown in figure 4.31 (e) and (f). The Weertman coefficient used was 0.025 and the exponent was 1/3. A Schoof-Gagliardini friction law was also implemented and it too presented some instability. A module is needed that calculates the surface normal at the bedrock when implementing this law. A sliding coefficient of 4e5 was used with a post-peak exponent q of 1.0, a max value C of 1.0 and a Glen exponent of 3. The results of the implementation of this sliding law is given in figure 4.31 (g) and (h). Both nonlinear implementations required a linear coefficient for times when the sliding law required the use of a linear approximation. The linear slip coefficient was set to 0.1 for both experiments to match the linear friction law used in figure 4.31 (a) and (b). Further experimentation is needed to discover the source of the instability and the best parameter values for each law.

The choices of the nonlinear friction law parameter values may lead to unfair comparisons in velocity magnitude, but the *locations* of high velocities can still be compared. Obviously, by decreasing the linear friction coefficient, surface velocities in (c) are much higher than those in (a). Looking at basal speeds in (d) we see two small pockets of high speed. These little pockets always seem to be the only areas of high basal velocities observed for any linear friction implementation. Notice how the Schoof-Gagliardini (h), and even the Weertman (f) sliding

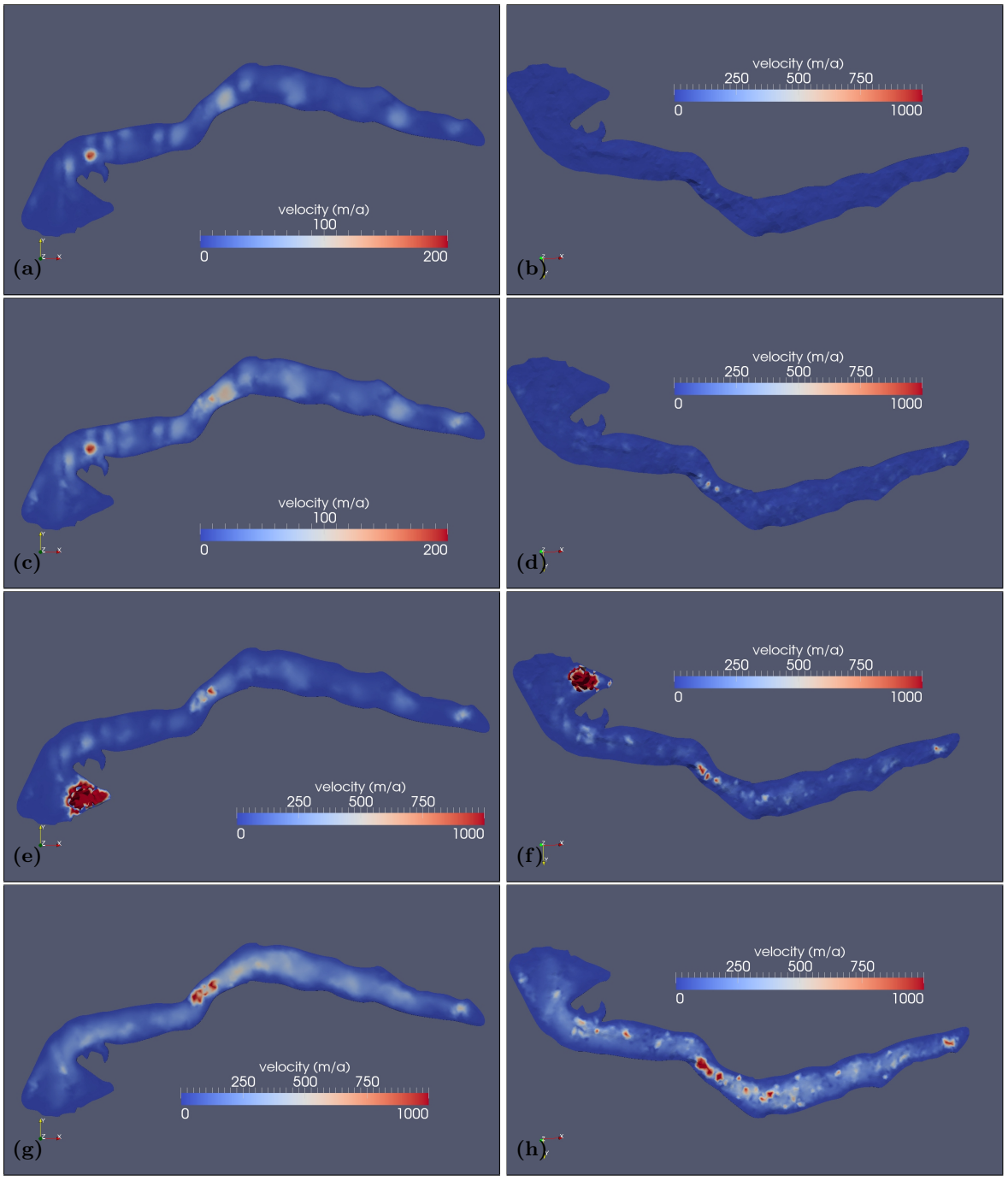

FIGURE 4.31: **Implementations of various friction laws and their effect on velocity at (left) the surface and (right) the base.** (a) and (b) Linear sliding law with coefficient 0.1. (c) and (d) Linear sliding law with coefficient 0.01. (e) and (f) Weertman nonlinear sliding law (displays instability). (g) and (h) Schoof-Gagliardini nonlinear sliding law. Results shown after 10 time steps.

laws show a more distributed and diverse pattern of ice velocities at the base. Ideally the Schoof-Gagliardini sliding law should be used due to its multivaluedness that may be required

in periodic switches of flow velocities in surge-type glaciers, but until the source of instability is found, a linear friction law must be used. This may be the most important next step in the BBGS model.

4.3.8 Experiments 92-98: Considerations of hydrology

4.3.8.1 Hydropotential

Calculations of the hydropotential are conducted for each of the four inputs of surface topography. Since the simple calculation given in section 2.2.6 relies of surface elevation, the hydropotential is expected to be different for each season. The addition of a solver that calculates glacier height is added. Contour maps of the hydropotential gradient at the glacier base for each season is given in figure 4.32.

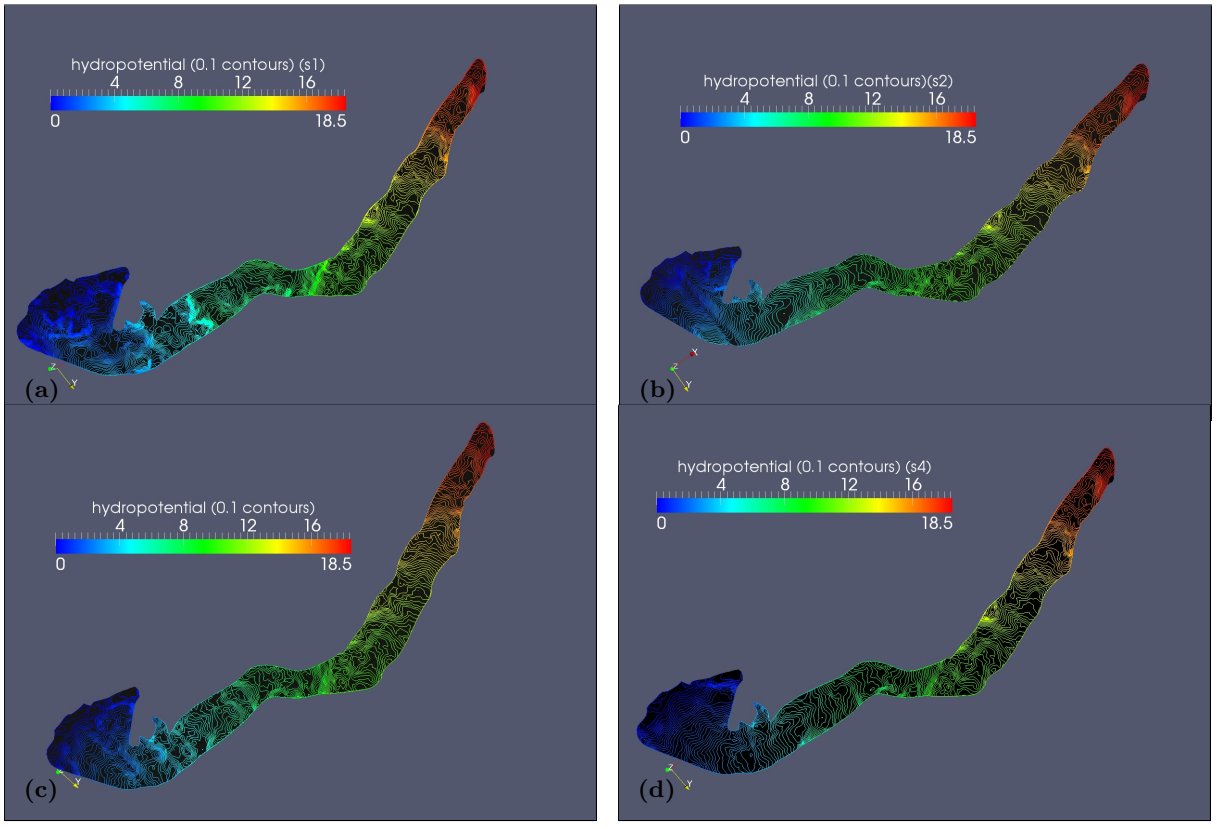

FIGURE 4.32: **Contour maps of the hydropotential gradient at the base of the BBGS.** (a) Summer 2011, (b) winter 2011/2012, (c) summer 2012 and (d) winter 2012/2013.

Contours of hydropotential in summer 2011 show areas of fast flow at the glacier bed and also many potential wells throughout the glacier base. This would lead to the assumption that cavities are formed in these wells thus implying a linked-cavity system of inefficient flow, or an IDS. This is what we would expect from a glacier in a surging state. The hydropotential in winter 2011/2012 seems to even out slightly in contour spacing and has a reduced number of potential wells. In summer 2012, a switch back to a more chaotic gradient is observed with more areas of fast flows and various potential wells pointing to an IDS still in existence. The hydropotential map for winter 2012/2013 exhibits the nicest contour map with mostly even spaced contours and a simple flow path down the glacier. The basal hydrological system could have possibly switched back to an efficient one at this point.

4.3.8.2 Double continuum hydrological system

An attempt was made to model the hydrological system at the base of the glacier by using the porous medium, double continuum approach given by Fleurian et al. (2014). Recent Elmer/Ice modules were created for this approach but effective implementation is not so straight forward. The new modules calculate the inefficient drainage system (IDS) and equivalent porous layer (EPL) water heads that are used to identify the state of the basal hydrological system. At the moment, only a switch from an IDS to an EDS is possible to observe with the current implementation. This is alright in our case since we expect a change from an inefficient system (as displayed in figure 4.32) to an efficient one when our surface topography is given in a late surge state. An attempt at modeling the basal hydrological system using the double continuum approach was done and the progression of the EPL water head, the emergence of which gives a state of transition from an IDS to an EDS, is shown in figure 4.33.

It is hard to interpret the results of this experiment but it seems to point to the transition of the IDS to an EDS occuring initially at the Bering-Bagley junction and spreading outward up and down-glacier. Theories presented in section 2.1.4 suggest that the kinematic wave that radiates outward, switching the drainage system from an EDS to and IDS, originates in this area. The small pockets, or rather elements, that remain dark blue say that these areas are still in IDS mode, as can be seen by looking at the IDS water head results, but whether this

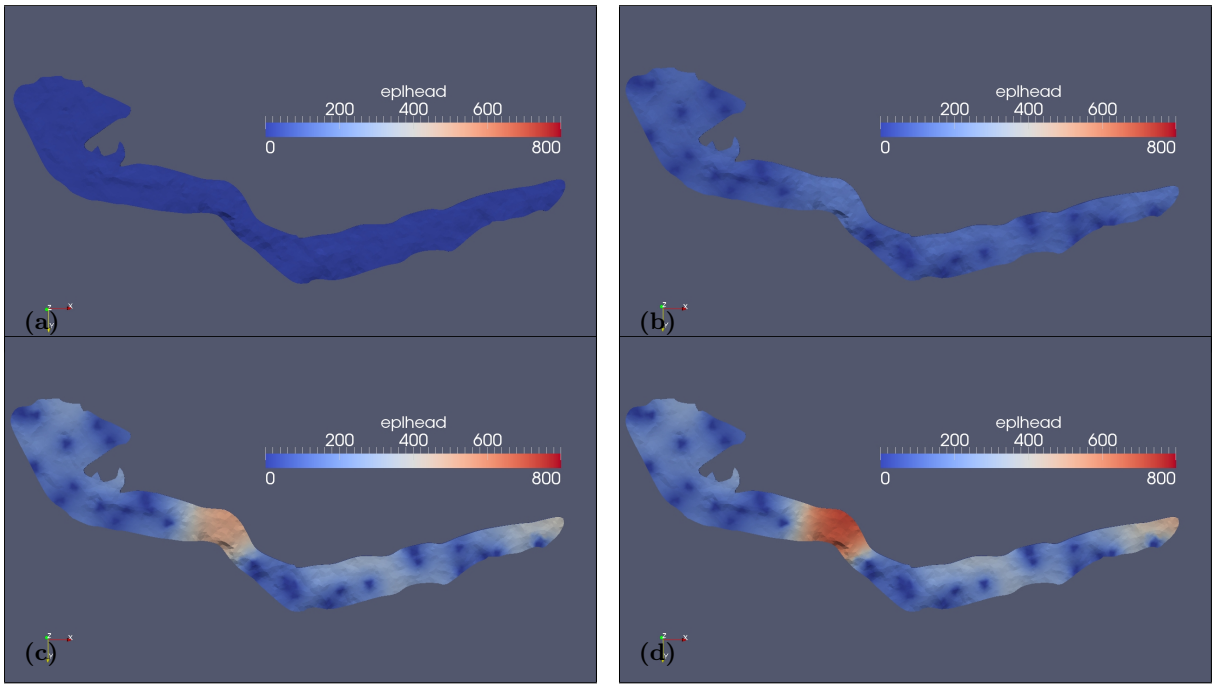

FIGURE 4.33: **Emergence of a state of transition to an efficient drainage system (EDS) from an inefficient one.** (a) After one day , (b) one week (c) two weeks and (d) four weeks.

means these are cavities of a linked-cavity system or is just some numerical error, is unknown. According to Fleurian et al. (2014), the time during which the EPL water head emerges (i.e. has a positive value, see figure 4.33 (c)) and the time at which the positive EPL water head reaches the terminus represents a transition period from an IDS to an EDS. Once the EPL head reaches the terminus, an efficient drainage system has been achieved. With the current simulations, the EPL head did not propagate down-glacier to the terminus thus implying only a transition phase throughout simulation. More experiments must be done with different hydrological parameter values to see if a full EDS can be achieved.

4.3.8.3 Inclusion of a large basal cavity

These last experiments seeks to add a large cavity at the base on the lower side of the BBJ. The existence of water-filled cavities reduces basal shear stress and thus allows for high flow velocities. The opening and closing of such cavities could be a factor in simulating a surge. Cavities are known to form on the lee-side of bedrock undulations and since there is a large one

at the BBJ, see figure 4.24, a large cavity is placed just below the junction as seen in figure 4.34.

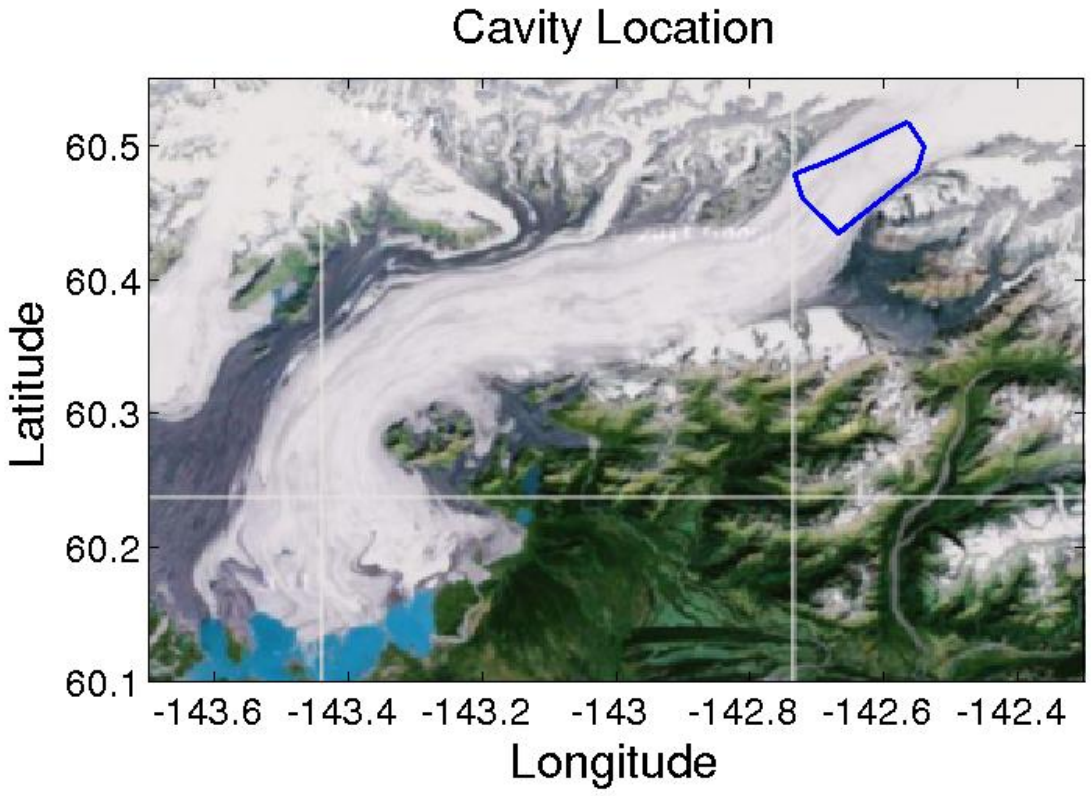

FIGURE 4.34: **Location of the artificially placed cavity at the bed of Bering Glacier.** A glacier cavity of 10 meters in height was placed just below the Bering-Bagley junction.

The addition of this cavity requires the treatment of the bottom glacier surface as a free surface. This in turn requires the creation of a DEM with the induced cavity to represent the base of the glacier. This simulation also requires the bedrock topography so that during calculation we make sure we do not go below that elevation. Simulations that include this cavity resulted in an immense amount of numerical instability, but in the end, by limiting the amount of allowed surface displacement per time step, a full model run was acquired. Not much information is gained from these experiments other than in the presence of a cavity, ice flows much quicker in the region directly above it. When adding a water pressure in the cavity, the ice velocities will increase even further. The increased velocities actually extend quite a way up and down glacier as seen in figure 4.35. Obviously, the simulated velocities are much higher than realistic speeds and this may be due to the size of the cavity, or in some mistreatment of the the bottom free surface.

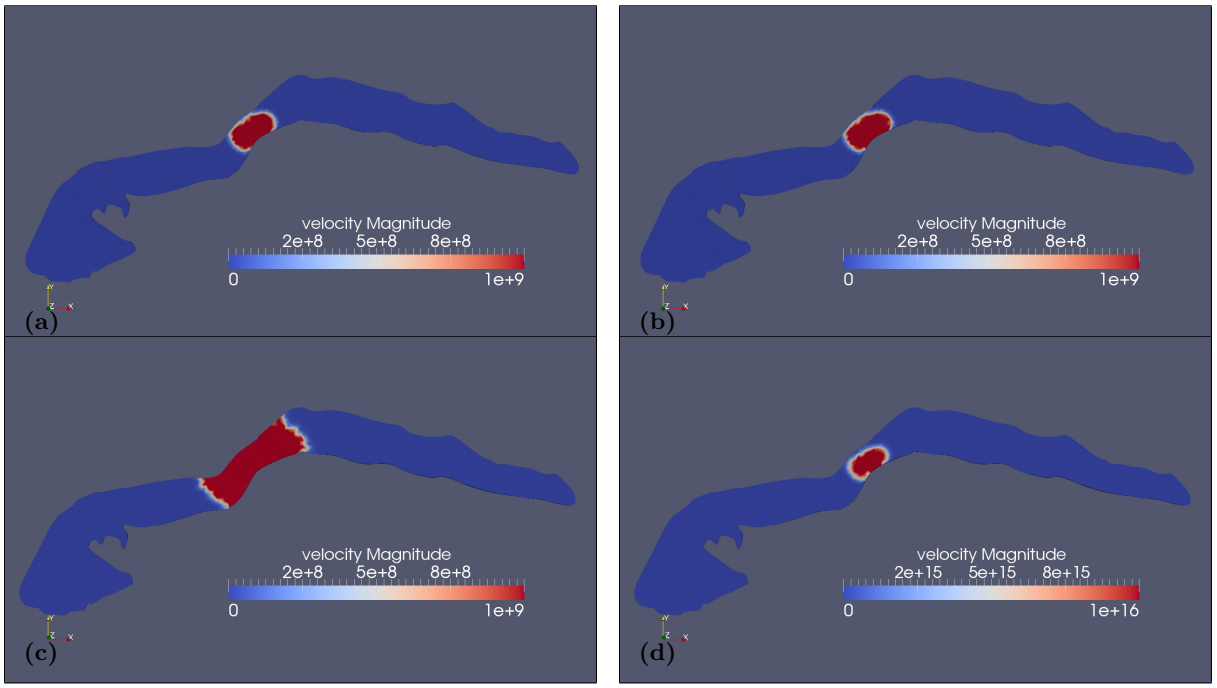

FIGURE 4.35: **Ice surface velocities when a large cavity is introduced below the BBJ.** (a) An empty cavity after 1 day. (b) An empty cavity after two years. (c) A pressurized cavity after one day. (d) A pressurized cavity after 1 day with a different scale to show the increased surface speeds when the cavity is pressurized.

Chapter 5

Conclusion

This thesis provides a variety of results of interest to the glaciological community and gives insight into the surge process in the Bering-Bagley Glacial System. A first application of CryoSat-2 data is presented to glaciology in the study of elevation change and mass transfer during the surge of Bering Glacier, Alaska, in 2011-2013. From this, a time series of Digital Elevation Maps were derived for uses in modeling and elevation change mapping. Four surface DEMs were created by application of ordinary kriging: (1) summer 2011 (May to October), (2) winter 2011/2012 (November to April), (3) summer 2012, and (4) winter 2012/2013. This in turn led to derivations of difference maps spanning the time periods of the surge process, which allowed analysis of elevation change and to relate this to geophysical processes that occur during the surge. Elevation change is analyzed in detail and field/aerial observations collected during the surge were used for validation. The feasibility of using CryoSat-2 data in large mountain regions was deemed sufficient for analysis of large surface changes due to a complete error analysis of the altimeter data and its use in kriging. For six-month data sets, DEMs have average error levels of 3.67 m (maximum 21.75 m), noise levels of 12.10 m (maximum 44.70 m) and nugget values of 28.5502 m^2 (maximum 999 m^2), which allows to map elevation change with an error level of 42.5 m maximally and generally 7.33 m. The maximal values occur only in isolated areas of the DEMs. Analysis of this elevation change and its interpretation related to the surge of Bering Glacier came a result. An advantage of the surge problem is that elevation changes are typically large on the order of 10s of meters to over 100 meters and hence the accuracy of the CryoSat-2 maps is sufficient.

Processes that we can observe include the following: (1) Collapse of the reservoir area and resultant mass transfer down Tashalich arm (the northern arm of lower Bering Glacier), (2) mass transfer up-glacier, (3) surface lowering in the northern arm and southern arm of central Bering Glacier, indicative of a restart of the surge in 2012, (4) longitudinal differentiation of elevation change processes, which indicate that Bering Glacier flows in a complex system of longitudinally oriented branches, (5) mass change along the front of the lobus, matching the several branches, (6) especially high rates of change in an area just below the junction of Bering Glacier and Bagley Icefield, where new formations of crevasses is prevalent throughout the surge, (7) continuation of mass transfer down-glacier in the Tashalich arm to 2012/2013, and (8) thickening in an area in the central lobus between 2011 and 2013. All of the changes match field observations except observation (8).

Sufficient data coverage over a smaller time frame would be more ideal to study the surge process. Large-scale surge phenomena can occur on the order of weeks or even days and so a six-month time span may be missing key processes or could be lumping separate surge events together. In general, CryoSat-2 SIRAL data can be employed to investigate large elevation changes that may occur in large mountain glaciers over the timeframe of six months to several years. Relatively high error levels in CryoSat-2 data may otherwise preclude analysis of elevation change in mountain glaciers or may require longer time series to aggregate data for better coverage and to average out errors.

The analysis then switched gears and jumped into the main part of the thesis dedicated to the modeling experiments. A successful representation of the glacial geometry was attained using derived DEMs and an ironed-out contour outline. Field variables that the model can calculate at any point forward in time include (1) velocity, (2) pressure, (3) stress, (4) strain-rate, (5) the eigenvalues/vectors of (3) and (4), (6) cumulative elevation change, (7) surface elevation, and later in experimentation, (8) glacial height, (9) hydropotential and (10) the IDS and EPL water heads.

Ideal time intervals were discovered based on the type of simulation that was being run. For longer simulations, on the order of a surge phase, larger time steps can be used, without loss of accuracy, to observe the results of a long term evolution with less amount of required computation. If a shorter simulation was sought, smaller time intervals can be used to analyze

changes that occur on the order of days. The effects of mesh evolution were investigated with the conclusion that only the z-component of the free surface should be allowed to update in time. Experiments were carried out using several different numerical schemes including the Backwards Difference Formula of order one, and the Crank-Nicholson method, which offered no noticeable accuracy or speedup from the more stable BDF.

Experiments with the introduction of an exaggerated bulge were conducted and showed that the collapse of this mass was redistributed both up and down-glacier. By increasing the basal slip coefficient, the bulge propagated outward at a slower rate, displaying the effect that basal friction has on surface events. The addition of a bulge did not disrupt the normal flow of the glacier as a whole. The bulge did not propagate at observed speeds. Ideally the propagation of a surge front induced by the bulge should act like an activation wave that switches the drainage system from an efficient one to an inefficient one, which would require the modeling and coupling of basal hydrology to the model. In the end, the simple addition of a large bulge in a suspected reservoir area was not enough to simulate a surge.

The effects of parsing up the lateral boundary into differently behaving segments gave a mixed bag of results. The division of the terminus gave us a way to account for calving of Bering Glacier into its pro-glacial lake, yet setting a flux condition here yielded unstable results. Although later experiments abandoned the separate treatment of the terminus, its addition may be interesting to account for once again when accumulation and ablation processes are added into the model and long-term simulations analyzing mass balances are sought. With the introduction of the Bering-Bagley junction, extreme mass loss was observed in the upper glacier in all but one simulation. By looking only at the positive elevation gain, the massive and sudden ice loss in the upper glacier sent a small amount of ice hurdling the other way down-glacier. Looking at this, two different flow paths were identified: one along the upper margins of the glacier that follows Tashalich Arm all the way to the terminus, and a second southern flow that curves around the Grindle Hills at a slower pace. Both flows were tracked by watching elevation rise and fall as small bulges moved down glacier. Despite being unrealistic with an extreme mass loss, this simulation accidentally produced the closest thing to a surge front that was observed. In an effort later in experimentation, cavitation near the BBJ was introduced to try and realistically reproduce these results.

The need to treat the BBJ as a separate boundary soon evaporated with the introduction of the Bagley Icefield to the model thanks to the acquisition of bed data there. A DEM of the bedrock along the entire BBGS was quickly generated and used, along with an extended CryoSat-2 derived surface DEM, as the glacier geometry in a full BBGS model. Immediate results of this model extension displayed behavior of mass transfer into known receiving zones.

After a failed attempt at parallelizing the full BBGS model and all of its complexities, insight was gained into the optimization of the problem size. It was deemed sufficient to only extrude three vertical layers to get the exact same behavior as 20. This reduced the problem size significantly and allowed for a refinement of the mesh to four times the resolution on a two-dimensional surface. This also reduced the size of the output files and run times since even with the quadruple amount of nodes in the horizontal planes, the total amount of nodes was still less than before. New and more refined processes on the surface were uncovered immediately. If given another shot on JANUS, a successful parallel implementation would most likely ensue thus allowing for an even more refined mesh on the order of the resolution of the input DEM itself.

The model was then run using each of the four derived surface DEMs to define the initial geometry. The evolution of each of these runs was displayed by finding their simulated elevation changes in a map that resembled the derived difference maps from the CryoSat-2 data. Comparisons were made that showed both similarities and dissimilarities. The best correlation happened when the glacier was allowed to evolve for a longer period of time. The surface lowering in central-Bering was shared by several maps as well as a small mass transfer above the overflow area. Behavior near the Bering-Bagley junction was disagreed on as the CryoSat-2 maps showed no sign of a decrease near the top with in increase right below. However, CryoSat-2 data lacked in this region of Bering and photo evidence actually supports the model's prediction of evolution.

The effect of changing the ice effective viscosity by varying the rheological parameters defined in Glen's flow law were then analyzed. By observing their effects on flow velocity, the increase or decrease of the variables showed a way to increase the overall speeds of the glacier flow. The only variable that one should tamper with is the enhancement factor, which is heuristically

determined for each individual glacier. This serves as a simple way to match observations by increasing or decreasing a single parameter.

The last portion of experiments represent roads down which further exploration could enhance the model's ability to simulate the surge process. The first of these is the addition of accumulation and ablation throughout the entire glacier surface. Simulations could be done on longer time scales on the order of a surge cycle, with varying degrees of accumulation, to see if ice acceleration occurs. A very complicated addition would be to couple the ice body to the atmospheric environment by allowing the surrounding temperature to effect ablation on the glacier surface. This could also allow the generation of melt water to supply the base with a source of liquid between the ice/bedrock interface.

Probably the most essential direction this thesis should go, is the way of the nonlinear, multivalued friction law. Because it is well known that basal slipping accounts for up to 90% of glacial movement, the importance of the relationship between the ice and the bed is of utmost importance. The Schoof-Gagliardini law is currently the only friction law that is multivalued, therefore allowing switches between fast and slow flow and its inclusion in the model without numerical instability could be a crucial step into successfully simulating a full surge model. Preliminary results show an increased overall picture of the basal velocity not seen with linear friction laws.

Another powerful advantage of the Schoof-Gagliardini friction law is that is has the ability to couple the glacier dynamics to the basal hydrological system. Inclusion of some type of basal hydrology is an important factor in a surge model as it is known that an increase in water pressure leads to fast flow velocities. Hydropotential maps were created displaying signs that the glacier was in a state of inefficient drainage during the surge and looked to be transforming into a more efficient one by the winter of 2012/2013. An attempt at the double continuum model of basal hydraulics was employed where clouded results seem to indicate that the transition to an efficient drainage system might start at the Bering-Bagley junction and extend outward from there. More accurate experimentation is needed to validate this claim.

Lastly, a look into sub-glacial cavities and an evolving bottom surface as another option that could simulate surge behavior was taken. The opening and closing of water-filled cavities could produce periodic flows of fast and slow ice. Once again the Schoof-Gagliardini friction is ideal

for this type of model. A large cavity at the bed, below the Bering-Bagley junction, a place where such a cavity could possibly form, was placed in the bottom surface DEM for a first simulation. Results showed that there was a massive increase in ice velocity at and around the BBJ and when water pressure was added, those velocities increased even more.

This model still has a ways to go before it can simulate the periodic surging behavior observed in the BBGS, but already is has provided some key insight into what makes a glacier surge and how a surge progresses. Through experimentation, the behavior of the current model has been documented, pointing out key aspects and demonstrating important factors in a surge model for the BBGS. Places of high activity on the glacier have been reproduced implying that these locations are due to the topography of the glacier, yet actual triggers of a surge were not observed leading to the conclusion that more must be added to the model for a surge to occur. The additions that are most likely to induce surge behavior, including basal hydrology, a better friction law and the inclusion of sub-glacial cavities, were implemented and the first steps were taken to introduce them into the current model. The foundation of a surge model for the Bering-Bagley Glacial System has been successfully created and the next logical extensions for improvements were identified and steps for their implementations have already begun.

Bibliography

P.R. Amestoy, I.S. Duff, and J.Y. L'Excellent. MUMPS multifrontal massively parallel solver version 2.0. 1998.

K.E. Atkinson. *An introduction to numerical analysis*. John Wiley & Sons, 2008.

A.H. Baker, R.D. Falgout, T.V. Kolev, and U.M. Yang. Scaling HYPRE's multigrid solvers to 100,000 cores. In *High-Performance Scientific Computing*, pages 261–279. Springer, 2012.

H. Björnson, F. Pálson, O. Siggurdsson, and G.E. Flowers. Surges of glaciers in Iceland. *Annals of Glaciology*, 36:82–90, 2003.

R.L. Bruhn, R.R. Forster, A.L.J. Ford, T.L. Pavlis, and M. Vorkink. Structural geology and glacier dynamics, Bering and Steller Glaciers, Alaska. *Geological Society of America Special Paper*, (462):217–234, 2010.

W.F. Budd. A first simple model for periodically self-surging glaciers. *Journal of Glaciology*, 14:3–21, 1975.

E.W. Burgess, R.R. Forster, C.F. Larsen, and M. Braun. Surge dynamics on Bering Glacier, Alaska, in 2008–2011. *The Cryosphere*, 6:1251–1262, 2012.

W.J. Campbell and L.A. Rasmussen. Three-dimensional surges and recoveries in a numerical glacier model. *Canadian Journal of Earth Sciences*, 6(4):979–986, 1969.

J.A. Church, P.U. Clark, A. Cazenave, J.M. Gregory, S. Jevrejeva, A. Levermann, M.A. Merrifield, G.A. Milne, R.S. Nerem, P.D. Nunn, A.J. Payne, W.T. Pfeffer, D. Stammer, and A.S. Unnikrishnan. *2013: Sea Level Change. In: Climate Change 2013: The Physical Science*

Basis. Contribution of Working Group I to the Fifth Assessment Report of the Intergovernmental Panel on Climate Change. Cambridge University Press, Cambridge, United Kingdom and New York, NY, USA, 2013.

G.K.C. Clarke. Fast glacier flow: Ice streams, surging, and tidewater glaciers. *Journal of Geophysical Research: Solid Earth (1978–2012)*, 92(B9):8835–8841, 1987.

G.K.C. Clarke, S.G. Collins, and D.E. Thompson. Flow, thermal structure, and subglacial conditions of a surge-type glacier. *Canadian Journal of Earth Sciences*, 21(2):232–240, 1987. doi: 10.1139/e84-024.

H. Conway, B. Smith, P. Vaswani, K. Matsuoka, E. Rignot, and P. Claus. A low-frequency ice-penetrating radar system adapted for use from an airplane: test results from Bering and Malaspina Glaciers, Alaska, USA. *Annals of Glaciology*, 50(51):93–97, 2009.

L. Copland, M.J. Sharp, and J.A. Dowdeswell. The distribution and flow characteristics of of surge-type glaciers in the Canadian High Arctic. *Annals of Glaciology*, 36:73–81, 2003.

K.M. Cuffey and W.S.B. Paterson. *The Physics of Glaciers*. Elsevier Science, 2010. ISBN 9780080919126. URL http://books.google.com/books?id=Jca2v1u1EKEC.

M. Drinkwater, R. Francis, G. Ratier, and D. Wingham. The European Space Agency's Earth Explorer Mission CryoSat: Measuring Variability in the Cryosphere. *Annals of Glaciology*, pages 313–320, 2004.

O. Eisen, W. Harrison, and C. Raymond. The surges of Variegated Glacier, Alaska, USA, and their connection to climate and mass balance. *Journal of Glaciology*, 47:351–358, 2001.

O. Eisen, W. Harrison, K. Echelmeyer, G. Bender, and J. Gorda. Variegated Glacier, Alaska, USA: a century of surges. *Journal of Glaciology*, 51:399–406, 2005.

European Space Agency: ESA. CryoSat Mission and Data Description (MDD). page 82 pp., 2007. URL http://eopi.esa.int.

D.R. Fatland and C.S. Lingle. Analysis of the 1993-95 Bering Glacier (Alaska) surge using differential SAR interferometry. *Journal of Glaciology*, 44(148):532–546, 1998.

D.R. Fatland and C.S. Lingle. InSAR observations of the 1993-95 Bering Glacier (Alaska, USA) surge and a surge hypothesis. *Journal of Glaciology*, 48(162):439–451, 2002.

D.R. Fatland, C.S. Lingle, and M. Truffer. A surface motion survey of Black Rapids Glacier, Alaska, U.S.A. *Annals of Glaciology*, 36:29–36, 2003.

B. de Fleurian, O. Gagliardini, T. Zwinger, G. Durand, E. Le Meur, D. Mair, and P. Råback. A double continuum hydrological model for glacier applications. *The Cryosphere*, 8(1):137–153, 2014.

G.E. Flowers and G.K.C. Clarke. An integrated modelling approach to understanding subglacial hydraulic release events. *Annals of Glaciology*, 31:222–228, 2000.

G.E. Flowers and G.K.C. Clarke. A multicomponent coupled model of glacier hydrology, 1, Theory and synthetic examples. *Journal Geophys. Res.*, 107(B11):2287, 2002a. doi: 10.1029/2001JB001122.

G.E. Flowers and G.K.C. Clarke. A multicomponent coupled model of glacier hydrology, 2, Application to Trapridge Glacier, Yukon, Canada. *Journal Geophys. Res.*, 107(B11):2288, 2002b. doi: 10.1029/2001JB001124.

G.E. Flowers, N. Roux, S. Pimentel, and C.G. Schoof. Present dynamics and future prognosis of a slowly surging glacier. *The Cryosphere*, 5:299–313, 2011.

A.C. Fowler. A theory of glacier surges. *Journal of Geophysical Research*, 92(B9):9111–9120, 1987.

A.C. Fowler. A mathematical analysis of glacier surges. *SIAM J. Appl. Math.*, 49(1):246–263, 1989.

T.P. Frappé and G.K.C. Clarke. Slow surge of Trapridge Glacier, Yukon Territory, Canada. *Journal of Geophysical Research: Earth Surface (2003–2012)*, 112(F3), 2007.

O. Gagliardini and T. Zwinger. The ISMIP-HOM benchmark experiments performed using the finite-element code Elmer. *The Cryosphere*, 2(1):67–76, 2008. doi: 10.5194/tc-2-67-2008. URL http://www.the-cryosphere.net/2/67/2008/.

O. Gagliardini, D. Cohen, P. Råback, and T. Zwinger. Finite-element modeling of subglacial cavities and related friction law. *Journal of Geophysical Research*, 112, 2007. doi: 10.1029/2006JF000576.

O. Gagliardini, F. Gillet-Chaulet, G. Durand, C. Vincent, and P. Duval. Estimating the risk of glacier cavity collapse during artificial drainage: The case of Tête Rousse Glacier. *Geophysical Research Letters*, 38(10), 2011.

O. Gagliardini, T. Zwinger, F. Gillet-Chaulet, G. Durand, L. Favier, B. de Fleurian, R. Greve, M. Malinen, C. Martín, P. Råback, et al. Capabilities and performance of Elmer/Ice, a new generation ice-sheet model. *Geoscientific Model Development Discussions*, 6(1):1689–1741, 2013.

R. Greve and H. Blatter. *Dynamics of Ice Sheets and Glaciers*. Springer, Berlin, Germany etc., 2009. ISBN 978-3-642-03414-5. doi: 10.1007/978-3-642-03415-2.

W. Harrison and A. Post. How much do we really know about glacier surging? *Annals of Glaciology*, 36(1):1–6, 2003.

W. Harrison, R. Motyka, M. Truffer, O. Eisen, M. Moran, C. Raymond, M. Fahnestock, and M. Nolan. Another surge of Variegated Glacier, Alaska, USA, 2003/04. *Journal of Glaciology*, 54(184):192–194, 2008.

U.C. Herzfeld. Least-squares collocation, geophysical inverse theory and geostatistics: a bird's eye view. *Geophysical Journal International*, 111(2):237–249, 1992.

U.C. Herzfeld. *The 1993-1995 surge of Bering Glacier (Alaska) — a photographic documentation of crevasse patterns and environmental changes*, volume 17 of *Trierer Geograph. Studien*. Geograph. Gesellschaft Trier and Fachbereich VI – Geographie/Geowissenschaften, Universität Trier, 1998.

U.C. Herzfeld. *Atlas of Antarctica: Topographic maps from geostatistical analysis of satellite radar altimeter data*, volume 1. Springer Verlag, 2004.

U.C. Herzfeld and H. Mayer. Surge of Bering Glacier and Bagley Ice Field, Alaska: an update to August 1995 and an interpretation of brittle-deformation patterns. *Journal of Glaciology*, 43(145):427–434, 1997.

U.C. Herzfeld, C.S. Lingle, and L. Lee. Geostatistical evaluation of satellite radar altimetry for high resolution mapping of Antarctic ice streams. *Annals Glaciol.*, 17:77–85, 1993.

U.C. Herzfeld, B. McDonald, B. Wallin, W. Krabill, S. Manizade, J. Sonntag, W. Yearsley, P. Chen, and A. Weltmann. Relationships between satellite laser altimetry and spatial ice surface roughness. *Computers & Geosciences*, 2012 in prep.

U.C. Herzfeld, B. McDonald, M. Stachura, R.G. Hale, P. Chen, and T. Trantow. Bering Glacier surge 2011: Analysis of laser altimeter data. *Annals of Glaciology*, 54(63):158–170, 2013a. doi: 10.3189/2013AoG63A348.

U.C. Herzfeld, B. McDonald, and A. Weltman. Bering Glacier and Bagley Ice Valley surge 2011: crevasse classification as an approach to map deformation stages and surge progression. *Annals of Glaciology*, 54(63):279–286, 2013b.

J.S. Howell and N.J. Walkington. Inf–sup conditions for twofold saddle point problems. *Numerische Mathematik*, 118(4):663–693, 2011.

N. Humphrey, C. Raymond, and W. Harrison. Discharges of turbid water during mini-surges of Variegated Glacier, Alaska, U. S. A. *Journal of Glaciology*, 32(111), 1986.

M. Jay-Allemand, F. Gillet-Chaulet, O. Gagliardini, and M. Nodet. Investigating changes in basal conditions of Variegated Glacier prior to and during its 1982–1983 surge. *The Cryosphere*, 5(3):659–672, 2011. doi: 10.5194/tc-5-659-2011. URL http://www.the-cryosphere.net/5/659/2011/.

H. Jiskoot, T. Murray, and A. Luckman. Surge potential and drainage-basin characteristics in East Greenland. *Annals of Glaciology*, 36:142–148, 2003.

A.G. Journel and C. Huijbregts. *Mining Geostatistics*. Academic Press, London, 2nd edition, 1989.

W. Kamb. Glacier surge mechanism based on linked cavity configuration of the basal water conduit system. *Journal Geophys. Res.*, 92(B9):9083–9100, 1987.

W. Kamb, C. Raymond, W. Harrison, H. Engelhardt, K. Echelmeyer, N. Humphrey, M. Brugman, and T. Pfeffer. Glacier surge mechanism: 1982-1983 surge of Variegated Glacier, Alaska. *Science*, 227(4686):469–479, 1985.

W. Krabill, E. Hanna, P. Huybrechts, W. Abdalati, J. Cappelen, B. Csatho, S. Frederick, E .and Manizade, C. Martin, J. Sonntag, et al. Greenland ice sheet: increased coastal thinning. *Geophysical Research Letters*, 31(24), 2004.

L.E. LeBlanc. *Icequakes and ice motion: A time-series analysis of the dynamics of the Bering Glacier, Alaska*. PhD thesis, University of Alaska Fairbanks, 2009.

C.S. Lingle and D.R. Fatland. Does englacial water storage drive temperate glacier surges? *Annals of Glaciology*, 36:14–20, 2003.

C.S. Lingle, A. Post, U.C. Herzfeld, B.F. Molnia, R.M. Krimmel, and J.J. Roush. Bering glacier surge and iceberg-calving mechanism at vitus lake, alaska, usa. *Journal of Glaciology*, 39: 722–727, 1993.

L. Lliboutry. Sub-glacial supercavitation as a cause of the rapid advances of glaciers. 1964.

L. Lliboutry. General theory of subglacial cavitation and sliding of temperate glaciers. *Journal of Glaciology*, 7:21–58, 1968.

G. Matheron. Principles of geostatistics. *Economic Geology*, 58(8):1246, 1963.

H. Mayer and U.C. Herzfeld. The rapid retreat of Jakobshavns isbræ, West Greenland: field observations of 2005 and structural analysis of its evolution. In *Progress in Geomathematics*, pages 113–130. Springer, 2008.

M.F. Meier and A. Post. What are glacier surges? *Canadian Journal of Earth Sciences*, 6(4): 807–817, 1969.

W.H. Mitchell. Exact and numerical solutions for Stokes flow in glaciers. Master's thesis, University of Alaska Fairbanks, Fairbanks, Alaska, 2012.

F.H. Moffitt and H. Bouchard. *Surveying*. The Intext Educational Publishers series in civil engineering. Intext Educational Publishers, 1975. ISBN 9780700224722.

B. Molnia and R. Williams. *Glaciers of Alaska*, volume 28-2. Alaska Geographic Society, 2001.

B. F. Molnia. *Alaska*. Satellite Image Atlas of Glaciers of the World. U.S. Geological Survey Professional Paper 1386-K, Washington, D.C., 2008.

B. F. Molnia and A. Post. Surges of the Bering Glacier. *Geological Society of America Special Paper*, (462):251–270, 2010a.

B.F. Molnia. Major surge of the Bering Glacier. *Eos, Transactions American Geophysical Union*, 74(29):322–322, 1993.

B.F. Molnia and A. Post. Holocene history of Bering Glacier, Alaska: A prelude to the 1993–1994 surge. *Physical Geography*, 16(2):87–117, 1995.

B.F. Molnia and A. Post. Introduction to the Bering Glacier system, Alaska/Canada: Early Observations and scientific investigations, and key geographic features. *Geological Society of America Special Paper*, (462):13–42, 2010b.

T. Murray, A. Luckman, T. Strozzi, and A. Nuttall. The initiation of glacier surging at Fridtjovbreen, Svalbard. *Annals of Glaciology*, 36:110–116, 2003.

R.R. Muskett, C.S. Lingle, J.M. Sauber, A.S. Post, W.V. Tangborn, B.T. Rabus, and K.A. Echelmeyer. Airborne and spaceborne DEM-and laser altimetry-derived surface elevation and volume changes of the Bering Glacier system, Alaska, USA, and Yukon, Canada. *Journal of Glaciology*, 55(190):316–326, 2009.

J.F. Nye. The flow of a glacier in a channel of rectangular, elliptic or parabolic cross-section. *Journal of Glaciology*, 5:661–690, 1965.

J.F. Nye. Water flow in glaciers: jokulhlaups, tunnels and veins. *Jour nal of Glaciology*, 17(76), 1970.

E. Osborn. Current Results, 2013. URL http://www.currentresults.com/Weather/Alaska/annual-snowfall.php.

M.S. Pelto, S.M. Higgins, T.J. Hughes, and J.L. Fastook. Modeling mass-balance changes during a glaciation cycle. *Annals of Glaciology*, 14:238–241, 1990.

A. Post. Periodic surge origin of folded medial moraines on Bering Piedmont Glacier, Alaska. *Journal of Glaciology*, 11:219–226, 1972.

D.J. Quincey, M. Braun, N.F. Glasser, M.P. Bishop, K. Hewitt, and A. Luckman. Karakoram glacier surge dynamics. *Geophys. Res. Let.*, 38:L18504, doi:10.1029/2011GL049004, 2011.

C. Raymond. How do glaciers surge? A review. *Journal of Geophysical Research*, 92(B9): 9121–9134, 1987.

C.F. Raymond. Evolution of Variegated Glacier, Alaska, USA, prior to its surge. *J. Glaciol*, 34 (117):154–169, 1988.

E. Rignot, J. Mouginot, C.F. Larsen, Y. Gim, and D. Kirchner. Low-frequency radar sounding of temperate ice masses in Southern Alaska. *Geophysical Research Letters*, 40(20):5399–5405, 2013.

H. Rothlisberger. Water pressure in subglacial channels. *Journal of Glaciology*, 11(62):177–203, 1972.

J.J. Roush, C.S. Lingle, R.M. Guritz, D.R. Fatland, and V.A. Voronina. Surge-front propagation and velocities during the early 1993-95 surge of Bering Glacier, Alaska, USA, from sequential SAR imagery. *Annals of Glaciology*, 36(1):37–44, 2003.

J. Ruokolainen, M. Malinen, P. Råback, T. Zwinger, A. Pursula, and M. Byckling. ElmerSolver manual. 2013.

J. Ruokolainena, P. Rabacka, M. Lylya, T. Kozubekb, V. Vondrakb, V. Karakasisc, and G. Goumasc. Improving the scalability of Elmer finite element software. 2013.

C. Schoof. The effect of cavitation on glacier sliding. *Proceedings of the Royal Society A: Mathematical, Physical and Engineering Science*, 461(2055):609–627, 2005.

H. Seddik, R. Greve, T. Zwinger, F. Gillet-Chaulet, and O. Gagliardini. Simulations of the Greenland ice sheet 100 years into the future with the full Stokes model Elmer/Ice. *Journal of Glaciology*, 58(209):427–440, 2012.

E.M. Shoemaker. Subglacial hydrology for an ice sheet resting on a deformable aquifer. *J. Glaciol*, 32(110):20–30, 1986.

J.F. Shroder, V.P. Singh, and U.K. Haritashya. *Encyclopedia of snow, ice and glaciers*. Springer, 2011.

R.A. Shuchman and E. G. Josberger. Bering Glacier: Interdisciplinary studies of Earth's largest temperate glacier. *Geological Society of America Special Paper*, (462):384, 2010.

U.S. Geological Survey. Bering Glacier [map]. Version 3. 1:250,000. In *Alaska Topographic Series*. Reston, Va: U.S. Department of the Interior, USGS, 1983.

W. Tangborn. Mass balance, runoff and surges of Bering Glacier, Alaska. *The Cryosphere*, 7 (3):867–875, 2013.

J. Turrin, R.R. Forster, C. Larsen, and J. Sauber. The propagation of a surge front on Bering Glacier, Alaska, 2001-2011. *Annals of Glaciology*, 54(63):221–228, 2013. doi: 10.3189/2013AoJ63A341.

C.J. Van der Veen. *Fundamentals of Glacier Dynamics*. CRC Press, 2013.

D.G. Vaughan. Relating the occurrence of crevasses to surface strain rates. *Journal of Glaciology*, 39(132):255–266, 1993.

J. Weertman. General theory of water flow at the base of a glacier or ice sheet. *Reviews of Geophysics*, 10(1):287–333, 1972.

D.J. Wingham, L. Phalippou, C. Mavrocordatos, and D. Wallis. The mean echo and echo cross-product from a beamforming interferometric altimeter and their application to elevation measurements. *IEEE Trans. Geoscience and Remote Sensing*, 42(10):2305–2323, 2004.

D.J. Wingham, C.R. Francis, S. Baker, C. Bouzinac, R. Cullen, P. de Chateau-Thierry, S.W. Laxon, U. Mallow, C. Mavrocordatos, L. Phalippou, G. Ratier, L. Rey, F. Rostan, P. Viau, and D. Wallis. CryoSat: A mission to determine the fluctuations in Earth's land and marine ice fields. *Advances in Space Research*, pages 841–871, 2006.

Y. Yang, A. Marshak, S.P. Palm, T. Várnai, and W. Wiscombe. Cloud impact on surface altimetry from a spaceborne 532-nm micro-pulse photon counting Lidar - System modeling for cloudy and clear atmospheres. *IEEE Transactions on Geoscience and Remote Sensing*, 2010.

T. Zwinger. Elmer/Ice, 2011. URL http://elmerice.elmerfem.org/.

T. Zwinger and J.C. Moore. Diagnostic and prognostic simulations with a full Stokes model accounting for superimposed ice of Midtre Lovăšnbreen, Svalbard. *The Cryosphere Discussions*, 3(2):477–511, 2009.

Appendix A

Example Solver Input File

```
!!!!!!!!!!!!!!!!!!!!!!!!!!!!!!!!!!!!!!!!!!!!!!!!!!!!!!!!!!!!!!!!!!!!!!!
!!
!! Elmer/Ice February 19th, 2014
!!
!! Thomas Trantow
!!
!! Bering Glacier - Experiment #80
!!
!!!!!!!!!!!!!!!!!!!!!!!!!!!!!!!!!!!!!!!!!!!!!!!!!!!!!!!!!!!!!!!!!!!!!!!

check keywords warn
echo on

$Step = "exp80"

! Define the parameter in MPa - a - m

$yearinsec = 365.25*24*60*60
$rhoi = 916.2/(1.0e6*yearinsec^2)
$rhow = 1000.0/(1.0e6*yearinsec^2)
```

```
! Prefactor from Cuffey and Paterson (2010) in MPa^{-3} a^{-1}
$A1 = 2.89165e-13*yearinsec*1.0e18
$A2 = 2.42736e-02*yearinsec*1.0e18
$gravity = -9.81*yearinsec^2


Header
  Mesh DB "." "bering_1000_ex"
End

Constants
  Water Density = Real $rhow
End

!!!!!!!!!!!!!!!!!!!!!!!!!!!!!!!!!!!!!!
Simulation
  Coordinate System  =  Cartesian 3D
  Simulation Type = Transient

  Timestepping Method = "bdf"
  BDF Order = 1
  TimeStep intervals = 1460
  Timestep Sizes =  $1.0/365.
  Output Intervals = 1

  Steady State Min Iterations = 1
  Steady State Max Iterations = 1

  Output File = "bering_$Step".result"
  Post File = "bering_$Step".ep"
  max output level = 10
```

```
End

!!!!!!!!!!!!!!!!!!!!!!!!!!!!!!!!!!!!
! The ice
Body 1
  Equation = 1
  Body Force = 1
  Material = 1
  Initial Condition = 1
End

! The Upper Free surface
Body 2
  Equation = 2
  Body Force = 2
  Material = 1
  Initial Condition = 2
End

!!!!!!!!!!!!!!!!!!!!!!!!!!!!!!!!!!!!
Initial Condition 1
  Pressure = Real 0.0
  Velocity 1 = Real 0.0
  Velocity 2 = Real 0.0
  Velocity 3 = Real 0.0
End
Initial Condition 2
  Zs Top = Variable Coordinate 1
    Real Procedure "USF_Bering" "TopSurface"
End
```

```
!!!!!!!!!!!!!!!!!!!!!!!!!!!!!!!!!!!!!!
Body Force 1
  Flow BodyForce 1 = Real 0.0
  Flow BodyForce 2 = Real 0.0
  Flow BodyForce 3 = Real $gravity
  Mesh Update 1 = real 0.0
  Mesh Update 2 = real 0.0

End

!! accumulation flux in m/year
Body Force 2
   Zs Top Accumulation Flux 1 = Real 0.0e0
   Zs Top Accumulation Flux 2 = Real 0.0e0
   Zs Top Accumulation Flux 3 = Real 0.0e0
End

!!!!!!!!!!!!!!!!!!!!!!!!!!!!!!!!!!!!!!
Material 1
  Density = Real $rhoi

  Viscosity Model = String "glen"
  Viscosity = 1.0 ! Dummy but avoid warning output
  Glen Exponent = Real 3.0

  Limit Temperature = Real -10.0
  Rate Factor 1 = Real $A1
  Rate Factor 2 = Real $A2
  Activation Energy 1 = Real 60e3
  Activation Energy 2 = Real 115e3
  Glen Enhancement Factor = Real 1.0
```

```
  Critical Shear Rate = Real 1.0e-10

  Constant Temperature = Real -1.0

  Cauchy = Logical True

  Mesh Youngs Modulus = Real 1.0
  Mesh Poisson Ratio = real 0.3

  ! Bed condition
  Min Zs Bottom = Variable Coordinate 1
    Real Procedure "./USF_Bering" "MinZsBottom"
  Max Zs Bottom = Real +1.0e10
End

!!!!!!!!!!!!!!!!!!!!!!!!!!!!!!!!!!!!!!
Solver 1
  Equation = "Navier-Stokes"

  Stabilization Method = String Stabilized
  Flow Model = Stokes

  Linear System Solver = Direct
  Linear System Direct Method = umfpack

  Nonlinear System Max Iterations = 50
  Nonlinear System Convergence Tolerance  = 1.0e-6
  Nonlinear System Newton After Iterations = 5
  Nonlinear System Newton After Tolerance = 1.0e-02
  Nonlinear System Relaxation Factor = 1.00
  Nonlinear System Reset Newton = Logical True
```

```
  Steady State Convergence Tolerance = Real 1.0e-3
End



Solver 2
  Equation = Sij
  Procedure = "ElmerIceSolvers" "ComputeDevStress"
  Variable = -nooutput "Sij"
  Variable DOFs = 1
  Exported Variable 1 = "Stress"
  Exported Variable 1 DOFs = 6

  Stress Variable Name = String "Stress"

  Flow Solver Name = String "Flow Solution"

  Linear System Solver = Direct
  Linear System Direct Method = umfpack
End

Solver 3
   Equation = "EigenStresses"
   Procedure = "ElmerIceSolvers" "ComputeEigenValues"
   Variable = -nooutput dumy
   Variable DOFs = 1

   ! The 3 eigenvalues
   Exported Variable 1 = EigenStress
   Exported Variable 1 DOFS = 3
```

```
  ! The 3 eigenvectors (Option)
   Exported Variable 2 = EigenVector1
   Exported Variable 2 DOFS = 3
   Exported Variable 3 = EigenVector2
   Exported Variable 3 DOFS =  3
   Exported Variable 4 = EigenVector3
   Exported Variable 4 DOFS = 3
End

Solver 4
  Equation = "Free Surface Top"
  Variable = String "Zs Top"
  Variable DOFs =  1
  Exported Variable 1 = String "Zs Top Residual"
  Exported Variable 1 DOFs = 1

  Procedure = "FreeSurfaceSolver" "FreeSurfaceSolver"
  Before Linsolve = "EliminateDirichlet" "EliminateDirichlet"

  Linear System Solver = Iterative
  Linear System Max Iterations = 1500
  Linear System Iterative Method = BiCGStab
  Linear System Preconditioning = ILU0
  Linear System Convergence Tolerance = Real 1.0e-9
  Linear System Abort Not Converged = False
  Linear System Residual Output = 1

  Nonlinear System Max Iterations = 100
  Nonlinear System Convergence Tolerance  = 1.0e-6
  Nonlinear System Relaxation Factor = 1.00
```

```
  Steady State Convergence Tolerance = 1.0e-03

  Stabilization Method = Bubbles
  Apply Dirichlet = Logical False ! No limiter needed for the upper surface

! How much the free surface is relaxed
  Relaxation Factor = Real 1.00

! Is there a maximum step-size for the displacement
! use/or not accumulation
  Use Accumulation = Logical True

! take accumulation to be given normal to surface/as vector
  Normal Flux = Logical False
End

Solver 5
  Equation = "Mesh Update"

  Linear System Solver = "Direct"
  Linear System Direct Method = umfpack

  Steady State Convergence Tolerance = 1.0e-04
End

Solver 6
  Exec Solver = After TimeStep
  Exec Interval = 1
  Equation = "result output"
  Procedure = "ResultOutputSolve" "ResultOutputSolver"
  Output File Name = String "bering_$Step".vtu"
```

```
  Output Format = String vtu
End

!!!!!!!!!!!!!!!!!!!!!!!!!!!!!!!!!!!!

Equation 1
  Active Solvers(5) = 1 2 3 5 6
End

Equation 2
  Active Solvers(1) = 4
  Flow Solution Name = String "Flow Solution"
  Convection = String Computed
End

!!!!!!!!!!!!!!!!!!!!!!!!!!!!!!!!!!!!
! Bedrock
Boundary Condition 1
  Target Boundaries = 1
! Sliding
  Flow Force BC = Logical True
  Normal-Tangential Velocity = Logical True

  Velocity 1 = Real 0.0e0
  Slip Coefficient 2 = Real 0.1
  Slip Coefficient 3 = Real 0.1

  Mesh Update 1 = real 0.0
  Mesh Update 2 = real 0.0
  Mesh Update 3 = real 0.0
```

```
End

! Upper Surface
Boundary Condition 2
  Target Boundaries = 2
!!! this BC is equal to body no. 2 !!!
  Body Id = 2

  Mesh Update 1 = Real 0.0
  Mesh Update 2 = Real 0.0
  Mesh Update 3 = Variable Zs Top
    Real Procedure "ElmerIceUSF" "ZsTopMzsIni"
End

! Sides Glacier
Boundary Condition 3
  Target Boundaries = 3

! No Sliding
  Velocity 1 = real 0.0
  Velocity 2 = real 0.0
  Velocity 3 = real 0.0

  Mesh Update 1 = real 0.0
  Mesh Update 2 = real 0.0
  Mesh Update 3 = real 0.0

End
```

Appendix B

Parallel Implementation

This appendix deals with the experiment of parallelizing the Elmer/Ice code on the supercomputer JANUS at the University of Colorado at Boulder. This was done as a group project with Brian McDonald and Alex Weltman, fellow co-workers and students, for the High Performance Computing course offered at CU.

B.1 Problem description

When one creates and runs a model simulation, they are essentially conducting an experiment. Hundreds if not thousands of experiments must be done in order to understand the important features and parameters that make up the model. Therefore it is essential that the run times of simulations be as fast as possible. Since materials such as ice evolve very slowly, their simulations need to be carried out over a large time period. In this case, model runs corresponding to 25 years (the approximate surge-cycle length) are sought. Taking this into account with the desired refinement of the solution (see section B.1.1), model runs can take anywhere between a couple hours to several weeks. Cutting this time down allows for more runs and therefore a better understanding of the glacier. For reasons described later on, the full problem that we are interested in solving was not successfully implemented in parallel. Instead of using a parallel implementation to cut down on run times and increase mesh resolution (as was originally planned) this appendix looks at the scalability of Elmer by running a simplified code.

B.1.1 Problem sizes

To test the scalability of a parallelized Elmer, three different mesh sizes were chosen to serve as three problem sizes. For the smallest problem size, a mesh with element sizes that were approximately 2000 meters in length was used. Larger element sizes means less total elements are required to cover the glacier, implying solutions will have a lower resolution. When breaking up the Bering-Bagley Glacial System into finite elements with element sizes of 2000 meters, a mesh with 1917 nodes, or element intersection points, is created with 2196 total elements, and 2552 boundary elements.

In order to parallelize the processing of the glacier, Elmer partitions the glacier by assigning each processor a certain amount of nodes (Ruokolainen et al., 2013). Each processor will receive nodes that correspond to geographic locations that are physically close to each other, as opposed to randomly distributing sections of the glacier to each core. In this fashion, the logical partitioning of the glacier model can correspond directly to a physical partitioning of the glacier. When the number of nodes is not evenly distributable among the number of processors, ElmerGrid assigns the nodes so that each core receives close to the same number (see table B.1).

For the second problem size, a mesh with element lengths of 1000 meters was chosen. This medium resolution mesh contained a total of 6993 nodes, 8606 elements, and 9320 boundary elements. As is obvious by the number of nodes, although the element length was cut in half, the total number of nodes more than tripled.

For the largest problem size, a mesh with element lengths of 500 meters was used. This produced an incredibly high resolution grid, as seen in figure B.3. This grid contained a total of 26673 nodes, 34132 elements, and 35560 boundary elements. Again, even though the element length was only cut in half, the number of nodes increased by a factor of five. Although CryoSat-2 provides grid resolutions of up to 250 meters per element size, it was chosen to use 500 meter elements as the highest resolution to keep run times down to a reasonable length for the completion of the experiment.

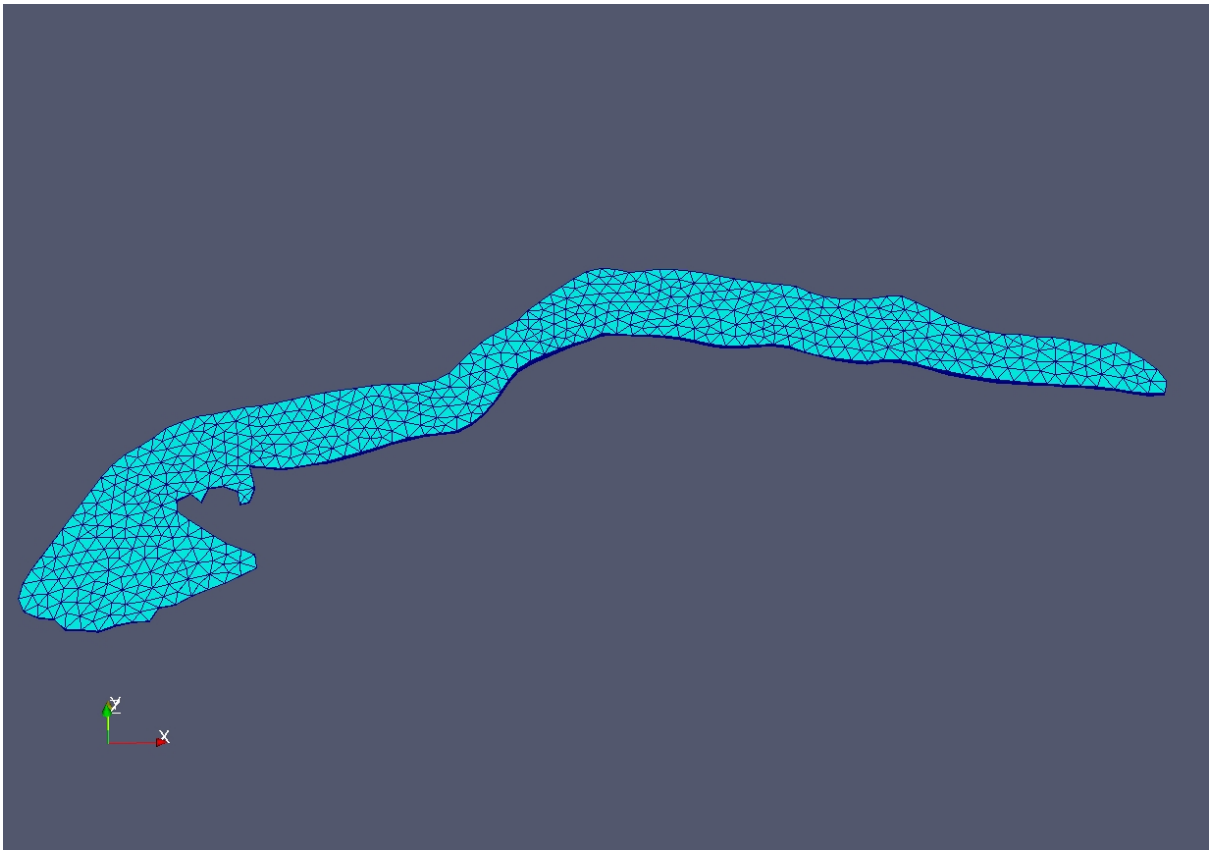

FIGURE B.1: **Low resolution mesh corresponding to element sizes of around 2000 meters. This mesh has a total of 1917 nodes, 2196 elements, and 2552 boundary elements.**

B.2 Implementation

B.2.1 Parallel installation

Elmer/Ice was not installed in serial on JANUS, and instead the parallel version was run with only one processor for serial results. This is ideal when comparing execution times and calculating speedup.

The first step in installing Elmer/Ice in parallel is deciding which solver to run. The solvers are covered in more detail in section B.2.3. If a direct solver is desired, the third party library MUMPS is required to be installed prior to the Elmer installation (Amestoy et al., 1998). If an iterative method is desired, either BiCGStab, which is built into the Elmer installation, can be used, or the third party library HYPRE needs to be installed (Baker et al., 2012). For this

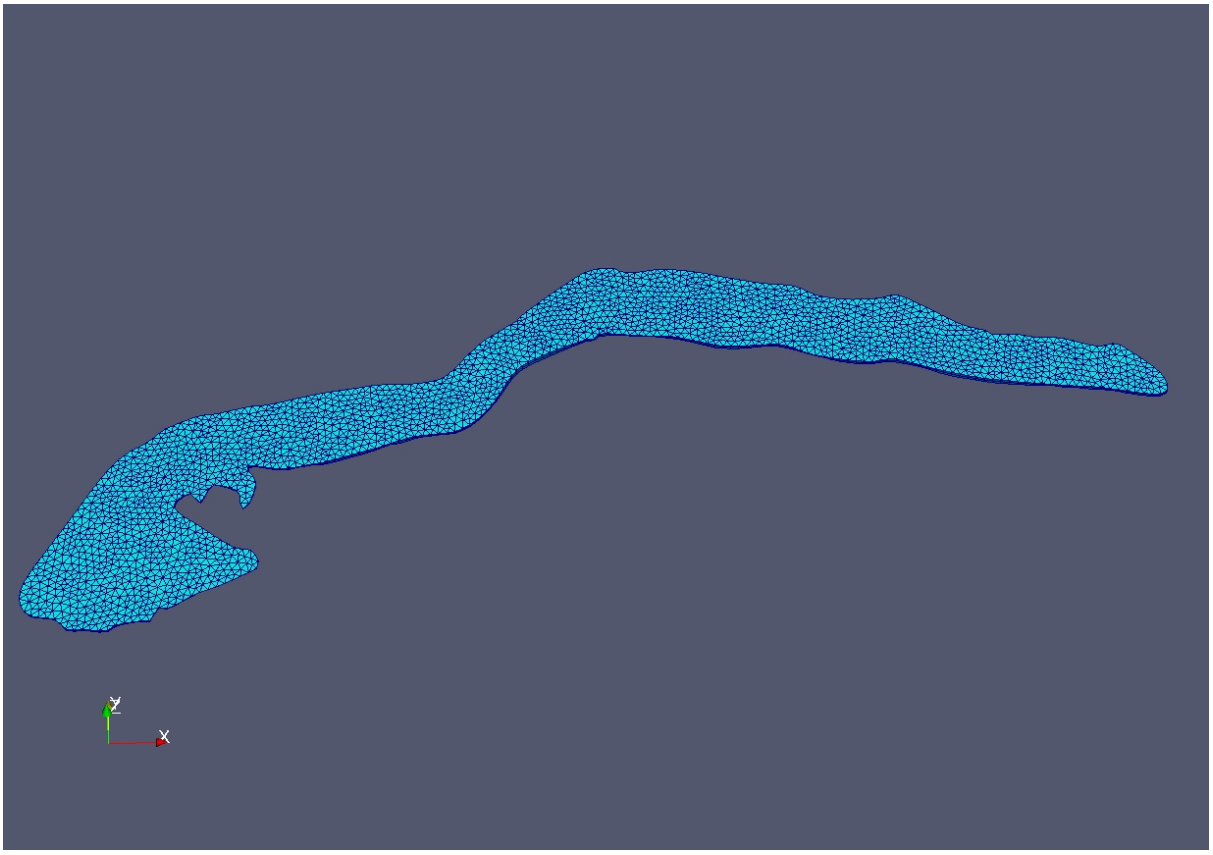

FIGURE B.2: **Medium resolution mesh corresponding to element sizes of around 1000 meters. This mesh has a total of 6993 nodes, 8606 elements, and 9320 boundary elements.**

experiment, all these options were explored but due to various reasons, only the BiCGStab solver was successfully installed (see section B.2.3). This section will describe the installation process for each of the options and the problems that arose. If admin rights were available, these libraries could be obtained using built in package installers such as apt-get or yum.

The installation of MUMPS requires a two other libraries, ScaLAPACK and BLACS. ScaLAPACK is a library of high-performance linear algebra routines used to solve dense and banded linear systems, least squares problems, eigenvalue problems, and singular value problems (Amestoy et al., 1998). The purpose of BLACS (Basic Linear Algebra Communication Subprograms) is to create a linear algebra oriented message passing interface. Both of these libraries can be attained as tar files from the websites (http://www.netlib.org/scalapack/) and (http://www.netlib.org/blacs/). The installation process of these libraries required environmental variables to be set since the paths to compilers on JANUS depend on the modules loaded

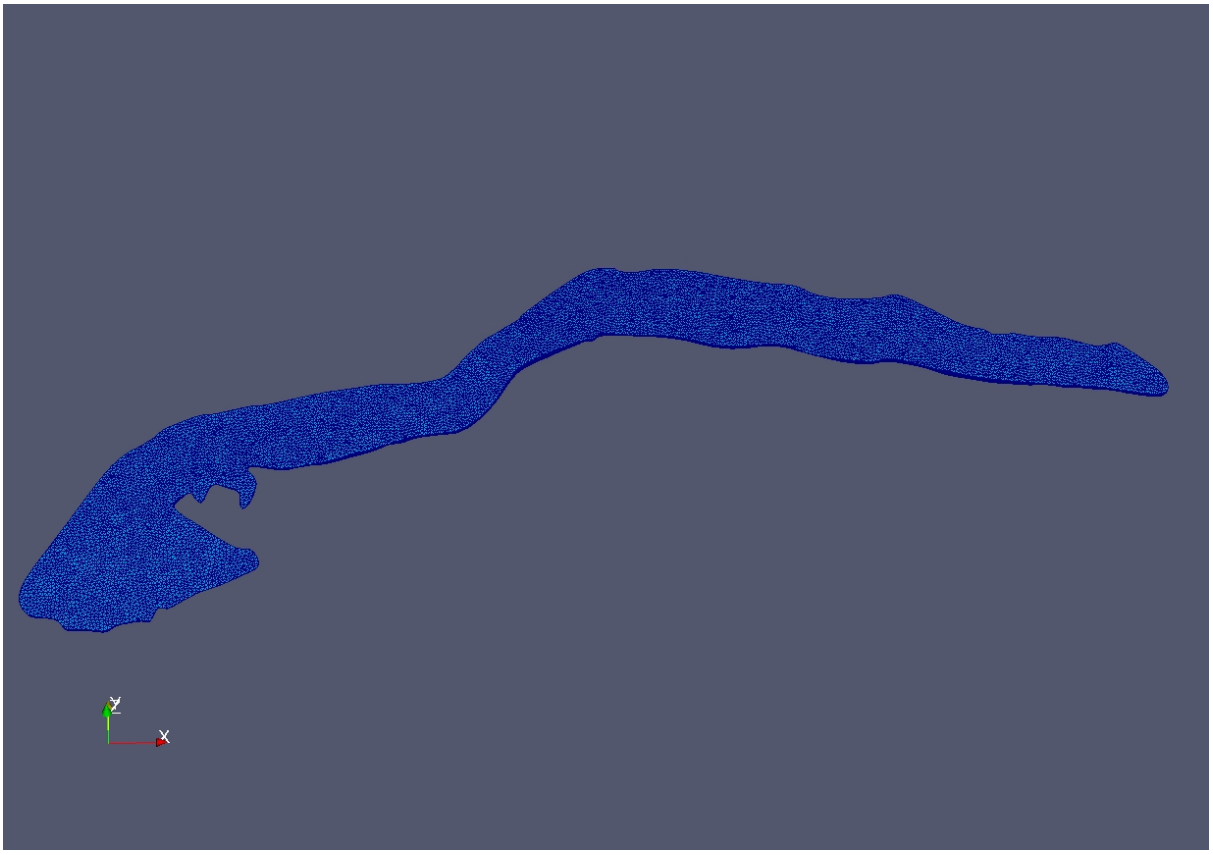

FIGURE B.3: **High resolution mesh corresponding to element sizes of around 500 meters. This mesh has a total of 26673 nodes, 34132 elements, and 35560 boundary elements.**

and are not standard Linux paths. Since we did not have admin rights, the installation paths would have to be set from the default opt directory to the project directory. After a lot of path finding and figuring out what version of compilers were required by the libraries, these two support libraries were successfully installed. A problem then arose when configuring and building the MUMPS library: despite installation paths being set to the project directory, some paths were hard-coded into certain files. This caused MUMPS to not find the commands it was looking for, even when the paths were loaded.

The installation of HYPRE is unnecessary since the BiCGStab solver is contained in the traditional, parallel Elmer installation. Given enough time, we would have compared the performance of these two solvers as an extra section to this study. Unfortunately, due to the numerous installation difficulties, we didn't have extra time for this experimentation. For this reason, a minimal amount of time was spent attempting to install HYPRE after installation failed due to

Partition #	Elements	Nodes	Shared	Boundary Elements
1	525	425	57	564
2	509	412	66	548
3	498	424	22	562
4	513	424	62	569
5	529	424	64	567
6	534	429	63	570
7	548	450	45	600
8	546	441	57	590
9	558	444	72	594
10	549	441	62	587
11	561	444	77	595
12	542	444	63	588
13	556	447	54	594
14	542	447	42	596
15	538	447	57	592
16	558	450	63	604

TABLE B.1: **Node distribution for a mesh size of 6993 nodes distributed to 16 processors.** Nodes are distributed among processors based on corresponding geographic location and number of processors.

pathing issues and lack of admin rights, and these were not investigated.

The installation of BiCGStab solver does not require any third party software. As such, only the Elmer/Ice installation steps were needed.

Finally, to install Elmer/Ice, acquisition of the directory which contains the code can be found on the following Github site (https://github.com/tehnick/elmerfem.git). The installation process requires the creation of a shell script that sets environmental variables and iterates over the directory's make files. Templates of makefiles can be found on the wiki-page: (http://www.elmerfem.org/elmerwiki/index.php/Compiling_Elmer_parallel_version_(Linux)). The shell script had to be changed depending on the solver being installed and the modules loaded. Similar to MUMPS, the installation had to be done locally in the project directory. There were a number of configuration errors. The majority of the installation time was spent finding the correct paths and linking the location of certain Elmer commands to each other.

The final result of the installation process was the Elmer/Ice software with the BiCGStab solver. All other solvers were not successfully installed. Fortunately, this solver was adequate for the scaling study.

B.2.2 ElmerGrid and ElmerPost

The first step when implementing a parallel run in Elmer is to partition the mesh used in serial and send those partitions to each processor for calculation (Ruokolainen et al., 2013). This is done by using the ElmerGrid command built into Elmer. The user must specify the number of partitions equal to the number of processors that will be used, and also the method of the partitioning. There are essentially two choices for the method of partition. The first, using the "-partition X Y Z" option when executing the ElmerGrid command, partitions the mesh in the x, y, and z directions X, Y, Z number of times respectively. The other option, induced by adding the option "-metis M N", uses the built in metis library that makes ideal partitions of the mesh into M parts via the method specified by N (Ruokolainena et al., 2013). We tried simulations that used every type of partition and found that the metis library that used PartGraphPKway method of partitioning yielded the quickest model runs. Once calculation on each processor is complete, results are combined via the ElmerPost command, which is also built into Elmer. Figure B.4 shows an overview of the parallel process with mesh partitioning.

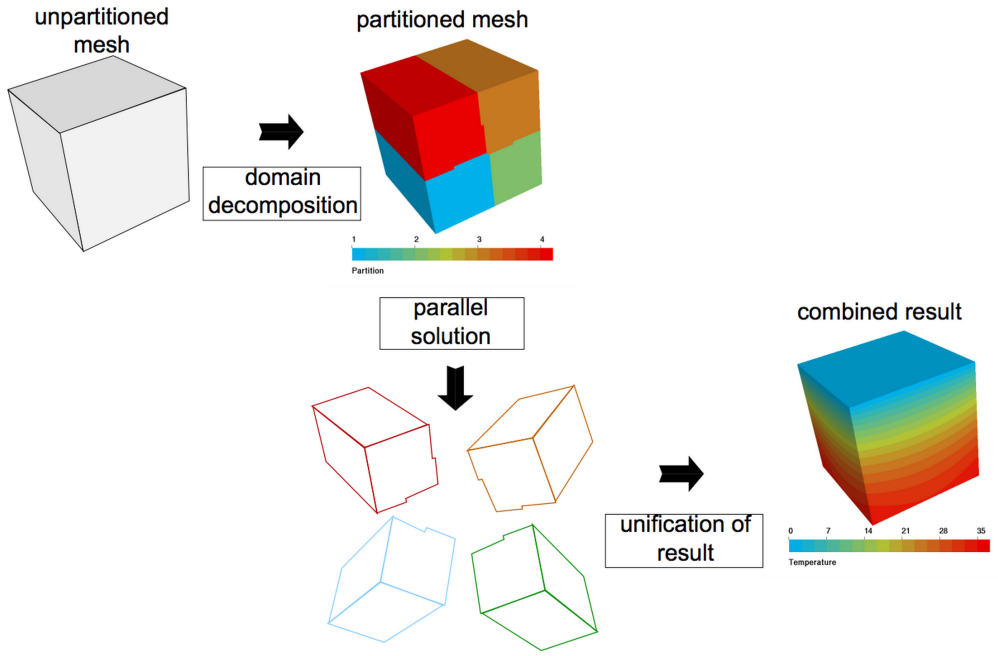

FIGURE B.4: **Overview of the parallel process using mesh partitioning in Elmer.** Illustration provided by Thomas Zwinger of CSC in Finland.

B.2.3 The Solver Input File and methods of calculation

In theory, the only part of the serial code that may need to be rewritten is the solver section corresponding to the Stokes equations (Zwinger and Moore, 2009). This is needed because the methods used to calculate the solution may have to be changed (see table B.2). Only in the case when the serial method is an iterative one, such as the Biconjugate Stabilize method, is there no need for a change in the SIF file. In this case, a direct method was used for solving using the Unsymmetric MultiFrontal sparse LU factorization Package (UMFPACK), which is not available in parallel and therefore the Stokes solver section needed to be changed to use one of the solution methods listed in the bottom row of table B.2. In general, direct methods are slower but do not use any approximations and are usually more stable. In order to avoid possible convergence issues that may arise with an iterative implementation, a direct method using the Multifrontal Massively Parallel sparse direct Solver (MUMPS) is ideally sought (Amestoy et al., 1998). Unfortunately, we were unable to install the MUMPS external library and link it with Elmer (see section B.2.1) thus forcing us to implement an iterative method.

Since implementation of the BiCGStab method required no compiling and linking of an external library (like HYPRE), we decided to change the SIF file to use it. This single SIF file can now be used in both serial and parallel runs and the Stokes solver section is shown in Appendix A. Few theoretical results are known about the convergence of the BiCGStab method and convergence behavior can be quite irregular, but as far as iterative methods for large sparse unsymmetric matrices go, it is the best option of those available in Elmer. The algorithm is actually slightly changed from serial to parallel, but there is no required action that needs to be taken in order to account for this.

An important part of the BiCGStab method is what is known as preconditioning. A preconditioner is a type of factorization or decomposition that is applied to the linear system before the iterations are done in order to optimize convergence (Gagliardini and Zwinger, 2008; Gagliardini et al., 2013; Zwinger and Moore, 2009). In this we had many options and in the end the Incomplete LU factorization or (ILUT) preconditioner was selected due to the highest speed in iterative convergence compared to other preconditioners.

	Direct	Iterative
Serial	**UMFPACK** (**Unsymmetric MultiFrontal** sparse LU factorization **PACKage**)	**BiCGStab** (**BiConjugate Gradient Stabiliation method**)
Parallel	**MUMPS** (**Multifrontal Massively Parallel** sparse direct **Solver**)	**BiCGStab and HYPRE** (**Parallel High Performance Preconditioners**)

TABLE B.2: **Methods of solving the Stokes equations in serial and parallel.** Blue - Built in to Elmer Red - External Library

B.2.4 Simulation length

Diagnostic simulations were carried out for a single step in time consisting of 50 linear iterations of the BiCGStab method. By setting the steady-state convergence tolerance very small (1e-9), we force the simulation to iterate through 50 linear iterations. In practice a more relaxed convergence tolerance of 1e-3 is sufficient and most of the simulations will converge to a steady-state before 50 iterations. Note that some simulations will diverge and not complete 50 full iterations (see section B.3). Diagnostic simulations, also known as steady state, are done in order to identify stress distributions as well as pressure maps. With this knowledge, better prognostic (or transient) simulations can be run over multiple time steps (ideally enough time to represent a surge cycle $\approx$ 25 years), but these types of runs were not considered in this study.

B.3 Results

Figure B.5 shows the execution time for each grid given a certain number of processors. As can be seen, increasing the grid size caused the execution time to increase, as would be expected. Also, increasing the number of processors decreased the execution time up until a point. This is a good sign of parallelization working correctly.

Note that the small grid could not have over 32 processors. This is due to the number of elements per processor becoming too small at this point according to ElmerGrid. Also, note that the Divergent Simulation X refers to runs that did not converge on a solution. The results corresponding to the divergent solutions, which are shown in figures B.5-B.8, should not be

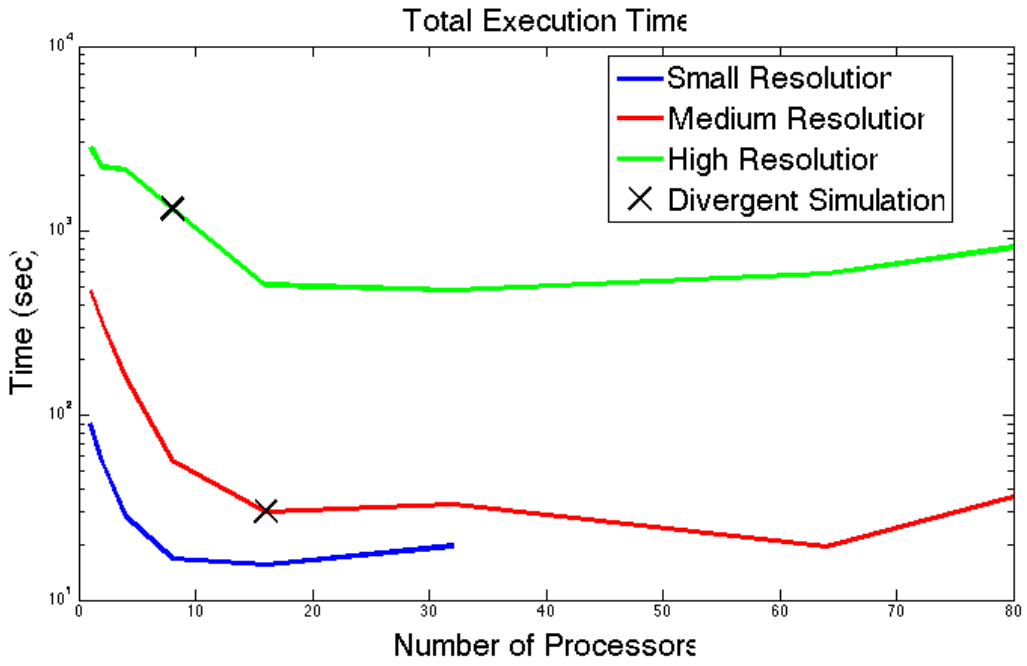

FIGURE B.5: **Total execution time of the simulations.** The low resolution simulation (blue) was run using 1, 2, 4, 8, 16 and 32 processors. The medium (red) and high (green) resolution simulations were run on 1, 2, 4, 8, 16, 32, 64 and 80 processors. The simulations using the medium resolution on 16 processors and high resolution on 8 processors diverged denoted by an X.

trusted for their accuracy. When a simulation diverged, the time of execution was very small since the calculation stopped prematurely.

B.3.1 Speedup

These results show the speedup per grid and number of processors. The speedup graphs for each grid look correct, that is there exists a speedup region, then a 'knee', then a segment of speedup decrease due to communication costs of shared node data. In 3-D the number of shared nodes for each partition is $\approx (N/P)^{2/3}$, and therefore if we have a fixed problem size N, and we double the number of partitions P, the shared nodes, i.e. the parallel overhead, increases by approximately 1.58. What is unexpected is the small and high resolution grid having similar max speedup (5) whereas the medium grid has a much higher max speedup (24). We believe this to be due to the relative fast serial speed of the high grid run. This would cause high grid speedup to be much lower.

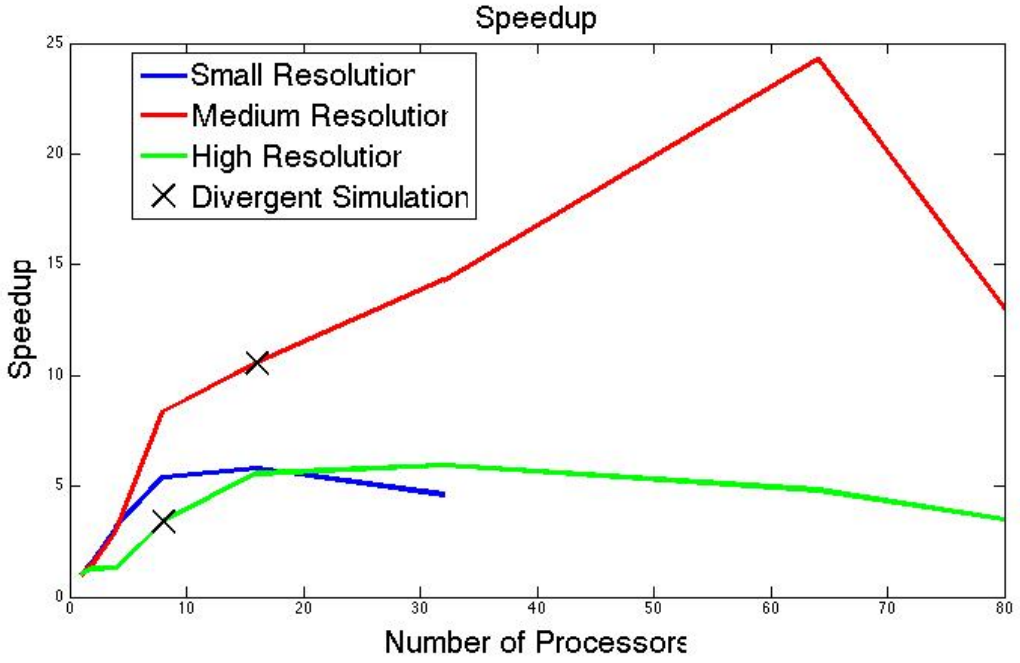

FIGURE B.6: **Speedup of simulations for low, medium and high resolution grids.** Note that speedup is calculated as serial time over parallel time.

B.3.2 Efficeincy

The efficiency for the software is in general pretty poor. Usually an efficiency of about 80% would be good, but all grids result in less than a 80% efficiency for processor numbers greater than 8. There is one point in the medium resolution grid that was over 100% efficiency. This unusual result can be explained by having an optimal element per processor configuration. Other parallel performance tests done with Elmer have observed superlinear speedup at times when the local linear problem fits to the cache memory. Assuming that the cache was optimally used, an above 100% efficiency would make sense.

B.3.3 Karp-Flatt metric

The results from the Karp-Flatt metric show what could be dominating the speedup. For the constant region in the center of the plot, this shows a large portion of the code is serial and isn't being parallelized. The last portion of the plot that shows an increase in Karp-Flatt over all grid sizes indicates that the overhead of communication between processors had a large effect on the speedup.

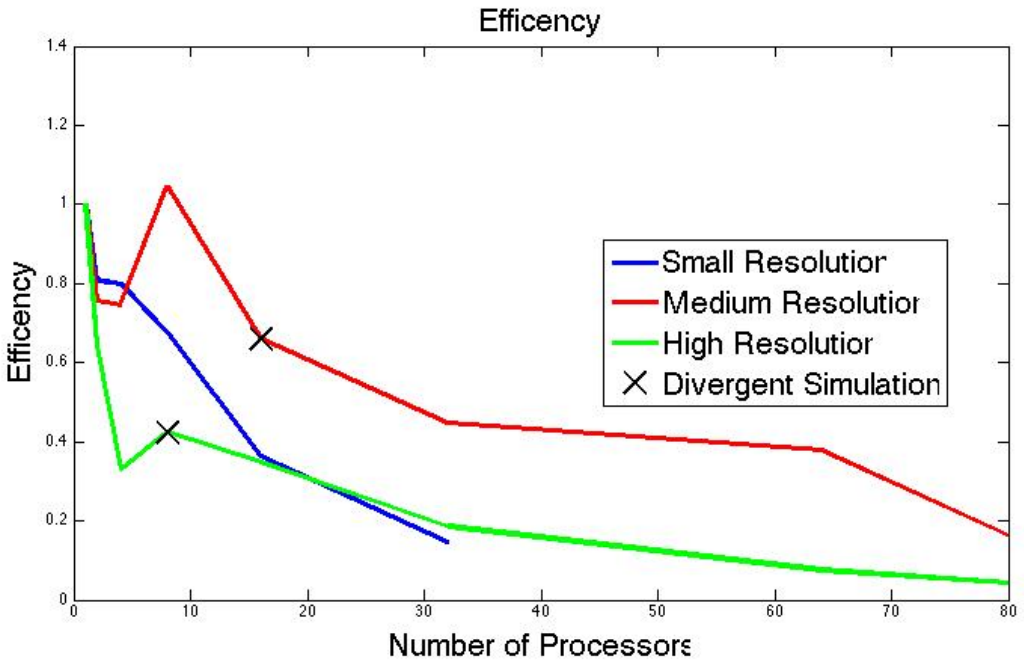

FIGURE B.7: **Efficiency of the simulations run at the various resolutions.** The efficiency bump at 8 processors is due to the local matrix size lining up nicely with the cache size for the medium resolution run whereas the the high resolution run using 8 processors cannot be taken as an actual boost in efficiency do to a divergent solution. Efficiency was calculated by speedup over the number of processors used.

B.3.4 Post-processing

Figure B.9 illustrates the stress distribution for each grid size. As can be seen, the results are the same except for some resolution effects. These results were checked for different numbers of processors as well (except when the model diverged).

B.4 Discussion

Figures B.10, B.11 and B.12 show the results of the HPCtoolkit analysis of grids with a different number of processors. As can be seen, the processors are generally very efficient. That is to say, there are not large gaps of idle processor time. However, looking at figures B.10 and B.11, it is apparent that the majority of time was spent on the ILU matrix solver, which is the preconditioner step in the iterative processes. This is in concordance with the fact that figures

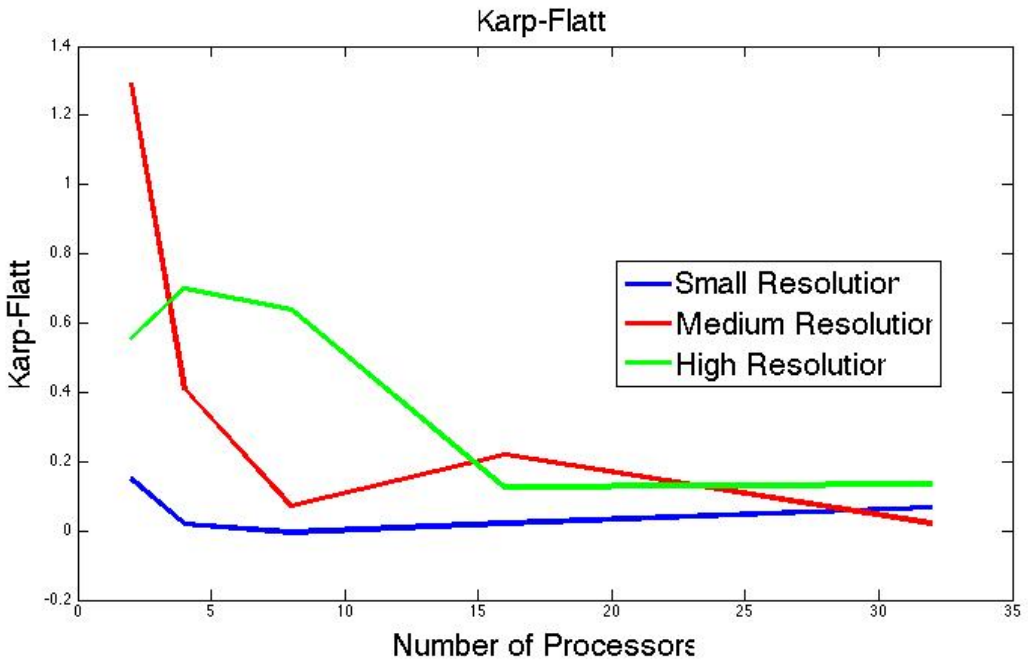

FIGURE B.8: **Karp-Flatt metric for the various resolutions.** The Karp-Flatt metric was calculated as $(1/speedup - 1/N)/(1 - 1/N)$, where N is the number of processors.

B.10 and B.11 display trace views of runs that diverged because the iterative preconditioner failed to factor the matrix. The HPCtoolkit allowed us to pinpoint the reason for divergence in these two simulations. To address this issue, we changed the preconditioner from "ILUT" to "Diagonal" and re-ran the divergent simulations. No divergence issues were found with this change in preconditioners and reasonable runtimes were obtained. Figure B.12 shows the toolkit trace view of the high resolution run using the "Diagonal" preconditioner, and the majority of computation time is spent in the iterative solver instead of the preconditioner, which is to be expected. An important note is that, as seen in figures B.10 and B.11, a few processors appear completely white, as if they have no trace data. This was a rendering problem with the toolkit and, although the data was not initially visible, it was still available via clicking.

B.5 Conclusion

The goal of this project was to analyze the effectiveness of a parallel implementation of Elmer/Ice. Though the installation process took the majority of the time due to numerous unforeseen complications, once it was successfully running the results proved favorable. We found a speedup

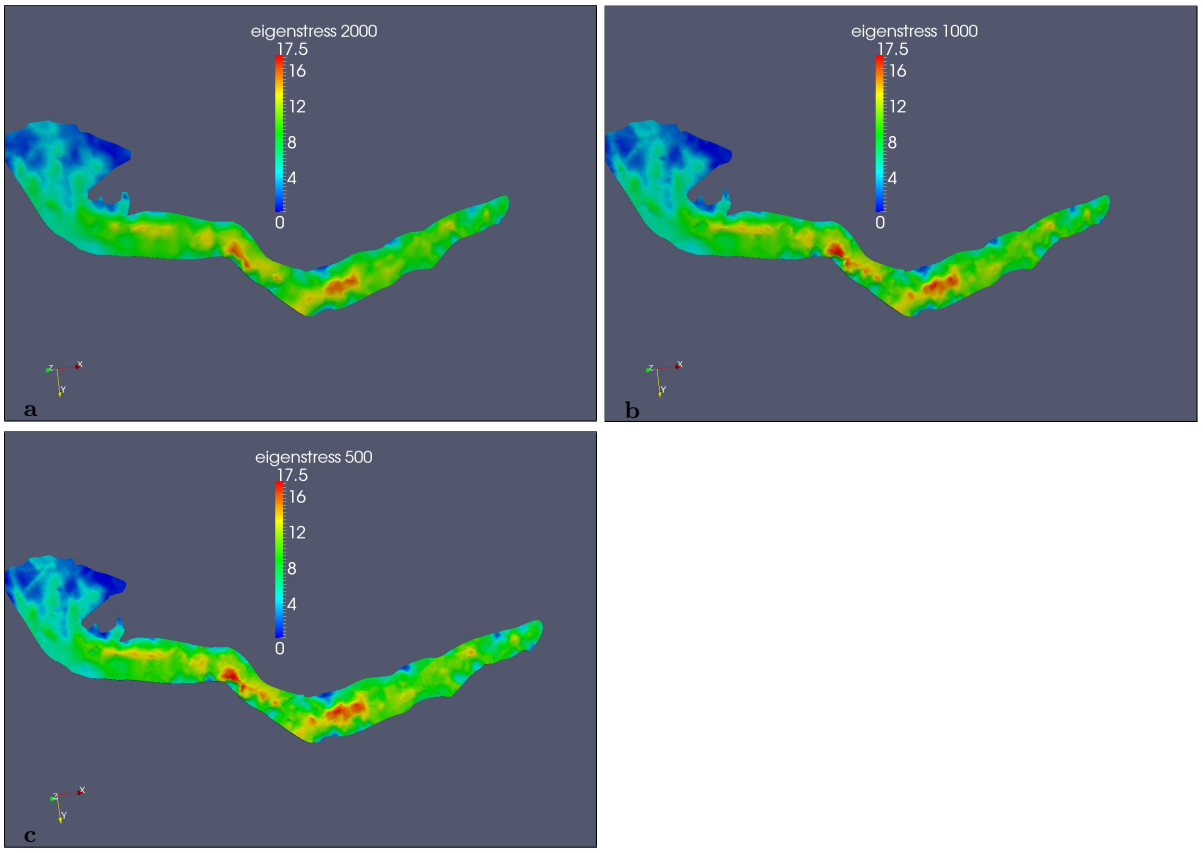

FIGURE B.9: **Stress distribution at the bed of the glacier at the three different resolutions.** (a) Low resolution corresponding to element sizes of around 2000 meters. (b) Medium resolution corresponding to element sizes of 1000 meters. (c) High resolution corresponding to element sizes of 500 meters.

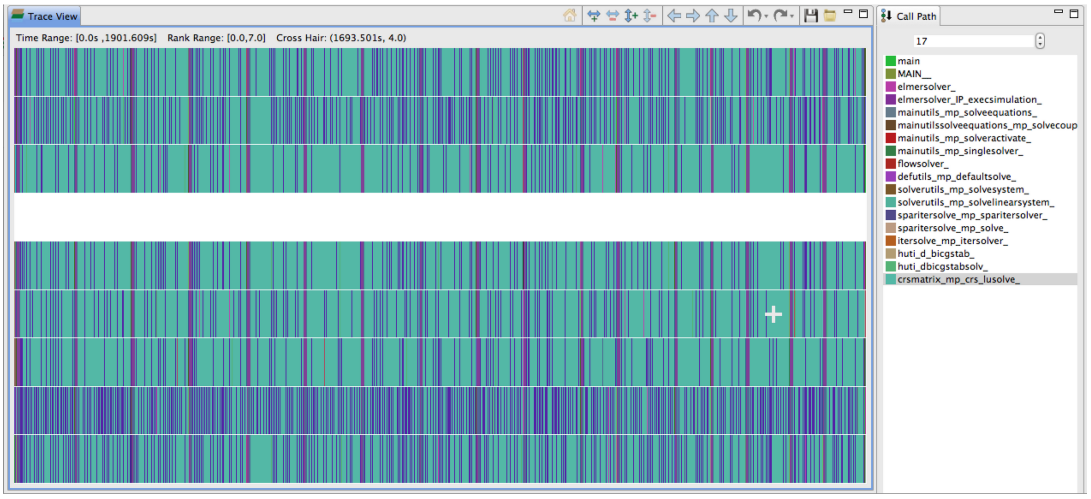

FIGURE B.10: **Profiling of the high resolution run using eight processors.** Note that this simulation diverged and most of the time was spent on calculating the ILU decomposition.

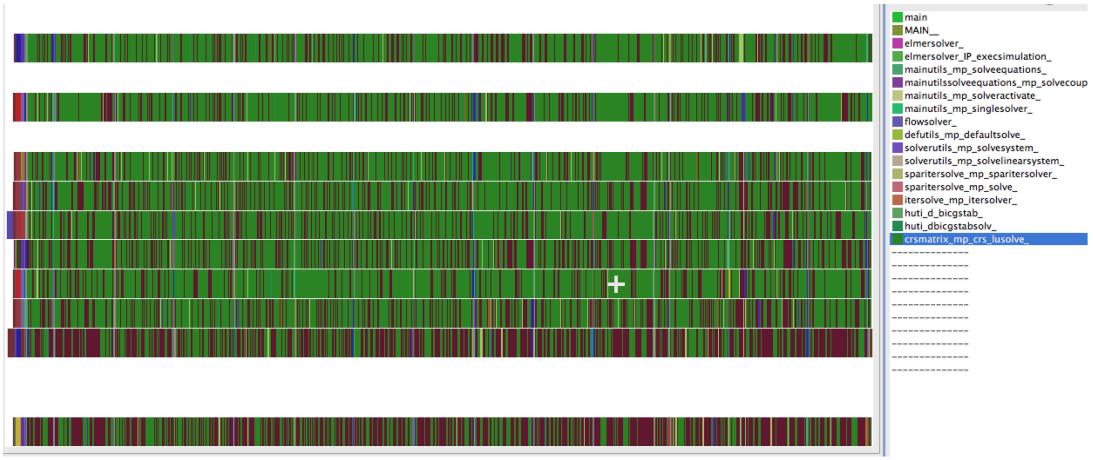

FIGURE B.11: **Profiling of the medium resolution run using 16 processors.** This simulation also diverged and spent most of its time doing the ILU decomposition.

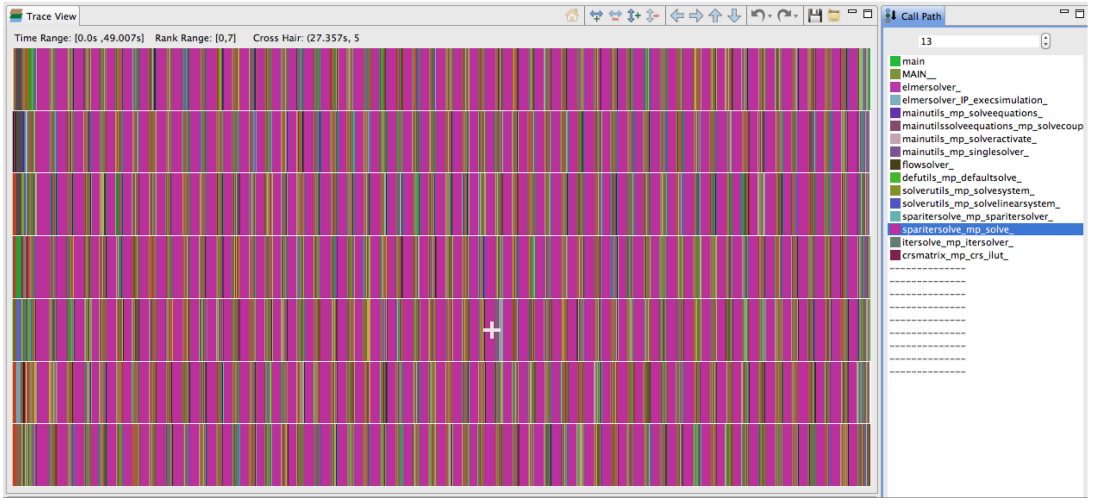

FIGURE B.12: **Profiling of the high resolution run on 8 processors with the "Diagonal" preconditioner.** This run displayed proper behavior with no convergence issues. As was expected, most time is spent in the flow solver and not in the preconditioner phase.

in the software and the results were shown to be consistent with previous serial runs across grid sizes. From a scientific viewpoint, the time per solution greatly improved even if efficiency wasn't ideal. From a learning standpoint, this project taught us an incredible amount about the real-world application of high performance scientific computing, the importance that computing can have on environmental problems, and the value of being a member of a highly motivated and collaborative open-source community. We also gained valuable experience in working with high performance computing tools and methods.

That being said, there is much more we would have liked to accomplish given more time and less

installation errors. Testing the other solvers, comparing different preconditioners, and diving more into the HPCtoolkit results to find other places for speedup are a few of the other goals that we would have liked to meet.

Appendix C

Lateral Friction Body Force and Measures of the Shape Factor

Throughout this entire thesis, we consider only gravity as an outside force, yet there are many other glacier models that include additional forces. An additional force would change our Stokes momentum balance equation to,

$$\nabla \cdot \boldsymbol{\sigma} + \rho \boldsymbol{g} + f = 0. \tag{C.1}$$

One common value for f considered a force arising from friction on the lateral sides of a glacier (Jay-Allemand et al., 2011; Nye, 1965). We define can define this body force as,

$$f = -\rho(\boldsymbol{g} \cdot \boldsymbol{t})(1 - f_s)\boldsymbol{t} \tag{C.2}$$

where $\boldsymbol{t}$ is the unit tangent vector perpendicular to the upper surface and f_s is a quantity called the "shape factor". The shape factor is a scalar quantity that depends on the transversal shape of the glacier. For $f_s = 1$ we would have an infinitely long glacier whereas a small f_s reflects a narrow glacier (Jay-Allemand et al., 2011). Obviously the shape factor can vary at different locations along the glacier, thus the lateral friction body force can have a stronger effect in some places. The shape factor depends on the fraction half the glacier width over the depth at the

Location	Width (m)	Depth at centerline (m)	Shape factor
Lobus Area	20209	360	0.9773
Khittrov-Grindle	10050	340	0.9570
Mid-Glacier	10004	800	0.8990
Upper-Glacier	7893	975	0.8458

TABLE C.1: **Width, depth at centerline and shape factor for various spots along Bering Glacier.** Width measurements are based upon UTM measurements from the contour outline and depth measurements at the centerline are given by radar measurements from the JPL WISE campaign (see section 3.3.1.2).

centerline (which is usually the deepest part of the glacier as it is with Bering see figure 4.6) (Nye, 1965). If we assume that the transversal shape of the glacier is approximately parabolic, then a simple calculation of the shape factor is given by,

$$f_s = \frac{2}{\pi} arctan(\frac{w}{2d}) \tag{C.3}$$

where w is the glacier width and d is the glacier depth at the centerline. A table showing the width, depth and shape factor based on the above equation is given in table C.1. The locations of measurement include the lobus area, mid-glacier, upper-glacier and a transverse line from the Khittrov Mountains to the Grindle Hills as is seen in figure C.1.

Because the shape factor is so high (close to one), the force given in equation C.2 will be very small throughout the glacier. This is due to the large size of Bering Glacier whose width is ultimately much larger than its depth. For this reason, the lateral friction body force was not included in the model of the BBGS.

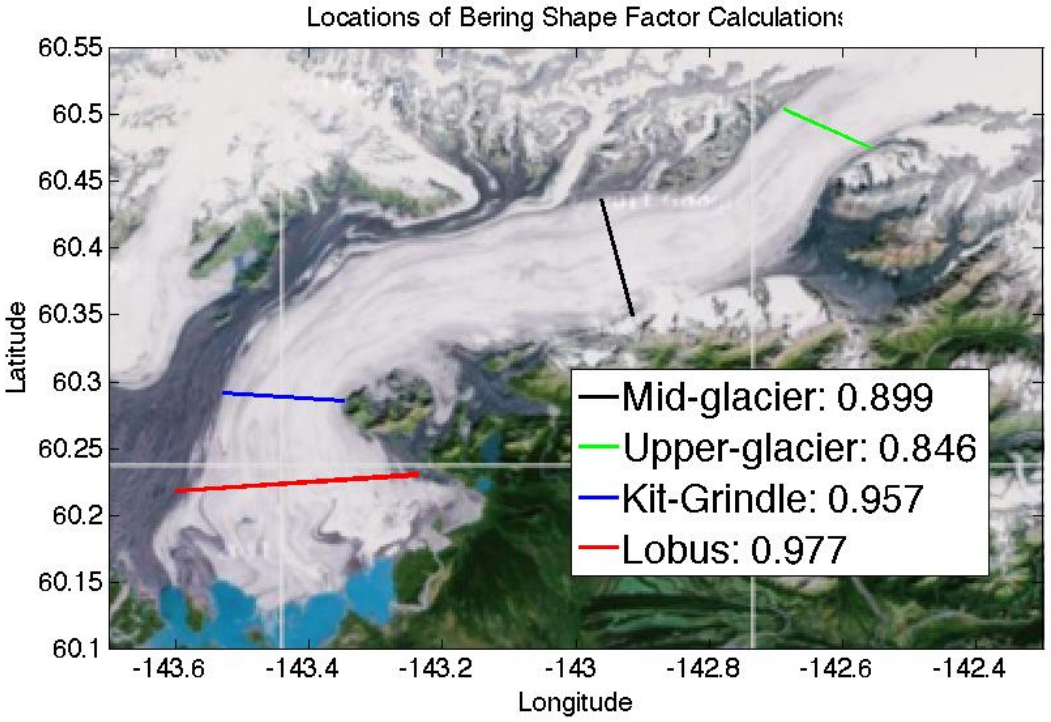

FIGURE C.1: **Shape factor locations and values throughout Bering Glacier.**